ABSTRACT

Title of Dissertation:	THE DIURNAL AND SEASONAL RADIATIVE EFFECTS OF CIRRUS CLOUDS UTILIZING LARGE AIRBORNE AND SPACE-BORNE LIDAR DATASETS
	Scott Christian Ozog, Doctor of Philosophy, 2019
Dissertation directed by:	Russell R. Dickerson Department of Atmospheric and Oceanic Science

Cirrus clouds are globally the most common cloud type, however, their radiative impact on the Earth remains a large source of uncertainty in global climate models. Cirrus are unique in that they are absorptive to terrestrial outgoing longwave radiation, while also relatively transmissive to incoming solar radiation. The interactions of this greenhouse and albedo effect determine the sign and magnitude of cirrus radiative effects. Cirrus are microphysically complex, and can exhibit a variety of different ice crystal shapes and sizes depending on the thermodynamic environment in which they form, and their dynamic formation mechanism. Our ability to reliably model cirrus radiative effects is dependent upon accurate observations and parameterizations incorporated into radiative transfer simulations. Laser lidar instruments provide valuable measurements of cirrus clouds unavailable by other radar systems, passive remote sensors, or in-situ instruments alone.

In this dissertation I developed and tested an improved calibration technique for the ACATS lidar instrument, and its impact on the direct retrieval of cirrus HSRL

optical properties. HSRL retrievals theoretically have reduced uncertainty over those from a standard backscatter lidar. ACATS flew on two field campaigns in 2012 and 2015 where it was unable to consistently calibrate its etalon. It has been operating from the lab in NASA GSFC collecting zenith pointing data of cirrus layers where the improved calibration has resulted in consistent and reliable separation of the particulate and Rayleigh signal components.

The diurnal trend of cirrus influence on the global scale has primarily been limited to data provided by satellites in sun-synchronous orbit, which provide only a snapshot of conditions at two times a day. Utilizing data from the CATS lidar aboard the ISS I investigated cirrus at four periods throughout the day in morning, afternoon, evening, and night across all seasons. Cirrus radiative effects were found to have a large latitudinal dependence, and have a greater potential to cool than many studies suggest with their primary warming contributions skewed towards the nighttime hours.

Constrained lidar retrievals reduce the assumptions made in retrieving cirrus optical properties. Utilizing the expansive airborne CPL dataset from six flight campaigns I model the radiative effects of over twenty thousand constrained cirrus observations. Mid-latitude cirrus were found to have a mean positive daytime forcing equivalent to that of the CO_2 greenhouse effect. However, synoptic cirrus were found to have a greater warming effect than convective cirrus, which were more likely to have a cooling effect.

THE DIURNAL AND SEASONAL RADIATIVE EFFECTS OF CIRRUS CLOUDS UTILIZING LARGE AIRBORNE AND SPACE-BORNE LIDAR DATASETS

by

Scott Christian Ozog

Dissertation submitted to the Faculty of the Graduate School of the
University of Maryland, College Park, in partial fulfillment
of the requirements for the degree of
Doctor of Philosophy
2019

Advisory Committee:
Professor Russell R. Dickerson, Chair
Professor Christopher C. Davis, Dean's Representative
Professor Juying Xie Warner
Professor Xin-Zhong Liang
Adjunct Professor, John E. Yorks
Adjunct Professor, Matthew J. McGill

Preface

This work is comprised of two research focuses analyzing cirrus clouds: lidar instrument science methodology in Chapter 2, and lidar data analysis & modeling in Chapters 3 and 4. In Chapter 2 I advance the efforts put forth by McGill *et al.* (1997a) and Yorks *et al.* (2014) to retrieve more reliable HSRL optical properties by improving calibration of the ACATS multi-channel lidar. This was completed with intentions of advancing towards modeling studies that I was unable continue to due to complications later discussed in Chapter 2, after which focus was shifted. In Chapter 3 I use the entire dataset of cirrus observations from the space-borne CATS lidar aboard the ISS to investigate the global mean diurnal and seasonal radiative effects of cirrus clouds on Earth's climate system. Then in Chapter 4 I further this work utilizing over 20,000 constrained airborne cirrus observations to model their radiative effects compared to the large scale gridded mean CATS observations modeled. Chapter 4 has been submitted to the *Journal of Geophysical Research – Atmospheres,* and is currently undergoing edits for resubmission. Chapter 3 is in preparation for submission to a peer-reviewed journal.

Dedication

I'd like to dedicate this dissertation to Dr. Ashton Peyrefitte, who passed away when I was finalizing this work. Dr. Peyrefitte, or Perry as many of his students knew him, taught my Introduction to Meteorology course my first semester at Central Michigan University in the Fall of 2008. Without Perry I'm not sure I'd be where I am today. After auditing his climatology course my second semester he recommended me for my first research project analyzing Michigan agricultural freeze/thaw cycles. He was the first professor I ever asked to write me a letter of recommendation. This helped me receive my NOAA Scholarship that paid for two years of tuition, and allowed me the opportunity to spend a summer in Alaska where I researched snowstorm events at the Anchorage NWS office. Perry's contributions to the department at CMU gave me, and many others, the ability to attend our first AMS Annual Meeting as bright-eyed undergrads. Perry was a passionate meteorologist, and an incredible educator, that greatly influenced the lives of countless students that now call themselves scientists. Thank you.

Acknowledgements

Under this dissertation is a foundation formed of the emotional support from friends & family, and the professional encouragement from colleagues & mentors along the way. Above all, I need to thank my family. My amazing Mom and Aunt Heidi, my brothers Nick, Alec & Dave, my sister Nicole, and of course my nieces Ellie, Haylie, & Amie. Thank you for always being there for me, and checking in to see how I was doing if I would fall radio silent when too engrossed in work. Mom, thank you for supporting my original decision to go to college for meteorology when I thought I wanted to be on TV. My undergrad advisors, Marty Baxter and Leigh Orf, for engaging me in research, and encouraging me to pursue graduate studies. This work would not have been possible without the team of "minions" at GSFC that I've worked close with, and have taught me so much over the past several years: Andrew Kupchock, Patrick Selmer, Stan Scott, Becca Pauly, and Dennis Hlavka. Russ for becoming my faculty advisor when I switched research projects. Especially John and Matt for their mentorship, and the incredible work experiences they enabled me to be a part of and learn from. Teaching me not just to be a data user, but all the hard work and complexity that goes into instrument science. Adam Greeley, whom I spent almost every lunch break with at Goddard going down proverbial rabbit holes of discussion. My awesome friends and volleyball team, "Pass and Hitties," thank you for keeping me sane with a social life outside of graduate school: Steph Kohls, Chelsea English, Jo & Eric Freeman, Shannon Hossinger, and Hillary Petersen. Finally, I need to thank Katie Lukens for introducing me to John, sending me down the path towards this work. Thank you all!

Table of Contents

List of Tables

List of Figures

List of Symbols

$\uparrow$	Outgoing
$\downarrow$	Incoming
A_n	etalon transmission parameter
A_T	telescope area
α	attenuated particulate backscatter
β_p	particulate backscatter coefficient
β_m	molecular backscatter coefficient
c	speed of light
C	calibration factor
d	etalon spacing
D_{eff}	effective particle diameter
dz	vertical resolution (analogous to Δr)
$\Delta\lambda$	Doppler shift in emitted wavelength
Δd_D	etalon defect parameter
$\Delta\lambda_{FSR}$	free spectral range in units of wavelength
$\Delta\lambda_L$	laser broadening (1/e width)
$\Delta\lambda_M$	molecular broadening (1/e width)
Δr	range bin width
δ	depolarization ratio
E_T	transmitted laser energy (Joules)
ε	relative error
γ	attenuated total backscatter
h	Planck's constant
η	Multiple Scattering Factor
j	channel number
ϕ	observation zenith angle
K	Kelvin
km	kilometers
L	etalon plate loss
λ	wavelength
λ_c	center wavelength of the etalon
λ_0	center position of the laser linewidth
m	meters
M	order of interference
N	number of photon counts
n_c	number of detector channels
N_{FSR}	free spectral range in units of channels
nm	nanometers
O_A	overlap correction function
θ	off-nadir angle of the laser beam
Θ	scattering angle
P_{11}	phase function
Q_E	detector quantum efficiency

r	range to scattering particles
R	etalon plate reflectivity
R_{eff}	particle effective radius
Sp	lidar ratio
σ	total extinction coefficient
σ_m	molecular extinction coefficient
σ_p	particulate extinction coefficient
T	Temperature
T_F	transmission of receiver filters
T_m^2	two-way molecular transmission
T_O	transmission of optics
T_p^2	two-way molecular transmission
τ	total optical depth
τ_p	particulate optical depth
μm	micrometers
ω	attenuated molecular backscatter
W	Watts

List of Abbreviations

ACATS	Airborne Cloud-Aerosol Transport System
ACEPOL	Aerosol Characterization from Polarimeter and Lidar
APB	Attenuated Particulate Backscatter
ARB	Attenuated Rayleigh Backscatter
ATB	Attenuated Total Backscatter
ATBD	Algorithm Theoretical Basis Document
BRDF	Bidirectional Reflectance Distribution Function
CATS	Cloud-Aerosol Transport System
CALIOP	Cloud-Aerosol Lidar with Orthogonal Polarization
CALIPSO	Cloud-Aerosol Lidar and Infrared Pathfinder Satellite Observation
CCAVE	CALIPSO-CATS Airborne Validation Experiment
CCSM3	Community Climate System Model v3.0
COD	Cloud Optical Depth
CPI	Cloud Particle Imager
CPL	Cloud Physics Lidar
CRF	Cloud Radiative Forcing
DISORT	Discrete Ordinate Radiative Transfer Solver
DJF	December January February
DWL	Doppler Wind Lidar
ESA	European Space Agency
FOV	Field-Of-View
FSR	Free Spectral Range
GCM	General Circulation Model
GISS	Goddard Institute for Space Studies
GMAO	Global Modeling and Assimilation Office
GOES	Geostationary Operational Environmental Satellite
GSFC	Goddard Space Flight Center
HDF	Hierarchical Data Format
HOE	Holographic Optic Element
HSRL	High Spectral Resolution Lidar
IGBP	International Geosphere Biosphere Programme
IN	Ice Nuclei
IPCC	Intergovernmental Panel on Climate Change
IR	Infrared
IRAD	Internal Research and Development
ISS	International Space Station
ITCZ	Inter-tropical Convergence Zone
IWC	Ice Water Content
IWP	Ice Water Path
JJA	June July August
LOS	Line-of-Sight
LW	Longwave
MAM	March April May
MC	Multi-Channel

MERRA-2	Modern-Era Retrospective Analysis for Research and Application version 2
MODIS	Moderate Resolution Imaging Spectroradiometer
NASA	National Aeronautics and Space Administration
Nd:YAG	Neodymium Yttrium Aluminum Garnet
NH	Northern Hemisphere
OD	Optical Depth
PBL	Planetary Boundary Layer
PDF	Probability Density Function
PODEX	Polarimeter Definition Experiment
PSI	Pounds per Square Inch
RT	Radiative Transfer
RF	Radiative Forcing
SEAC4RS	Studies of Emissions and Atmospheric Composition, Clouds and Climate Coupling by Regional Surveys
SH	Southern Hemisphere
SNR	Signal-to-Noise Ratio
SON	September October November
SW	Shortwave
SZA	Solar Zenith Angle
TOA	Top-of-the-Atmosphere
TTL	Tropical Tropopause Layer
UTC	Coordinated Universal Time
WAVE	Wallops Airborne Vegetation Experiment
VDR	Volume Depolarization Ratio

Chapter 1: Introduction

1.1 Motivation and Importance to Study Cirrus

Cirrus clouds, composed of ice particles are found in the upper troposphere, and sometimes lower stratosphere (Sassen, 1991; Murphy *et al*., 1990; Wang *et al*., 1996), play a crucial role in modulating Earth's radiative energy budget. Low and mid-level tropospheric clouds, composed of spherical liquid water droplets, are optically thicker than high cirrus clouds, and block more incoming shortwave (SW) solar radiation cooling the underlying atmosphere. Cirrus clouds, however, are relatively transmissive to incident SW radiation while absorptive to longwave infrared (IR) terrestrial radiation (Stephens 2005). This weak albedo effect combined with a relatively stronger greenhouse effect leads to a generalization that cirrus cause a net positive cloud radiative forcing (CRF; Liou, 1986) at the top of the atmosphere (TOA). This has led to a general paradigm that cirrus are a net warming component of the climate system (Boucher *et al.* 2013).

Globally, cirrus are the most common cloud type, having occurrence frequencies of 40-50% (Mace *et al.* 2009; Wylie and Menzel 1999). In the mid-latitudes frequencies are approximately 30-40%, and in the tropics they can be as high as 90% due to the prevalence of the inter-tropical convergence zone (ITCZ; Martins *et al.* 2011; Nazaryan *et al.* 2008; Wang and Sassen 2002). Cirrus clouds also impose possible positive climate feedbacks where their effective warming induces further warming. Cirrus radiative forcing is inversely related to the cloud top temperatures. In a warmer atmosphere cirrus heights are expected to increase leading to a greater decreased cloud top temperatures, and therefore a greater IR forcing component by reducing outgoing IR radiation at the cloud

top (Liou, 1986; Boucher *et al.* 2013). Although cirrus net RF can be an order of magnitude less than lower liquid water clouds (Campbell *et al.* 2016), their occurrence frequencies and long lifetimes make them an important part of the Earth's climate system (McFarquhar *et al.* 2000). Despite their importance, large uncertainties remain with respect to cirrus subtypes and associated radiative properties due to their complexity. This has resulted in cirrus parameterization being a key source of uncertainty in numerical simulations and global circulation models (GCM; Boucher *et al.* 2013; Del Genio, 2002).

Cirrus microphysical properties including particle size, particle shape, number density, and ice water content (IWC) exhibit large variability dependent on the conditions under which they form (Sassen, 2001). Shown in Figure 1.1 is how this cascades into affecting all cirrus properties. Optical properties include particulate extinction, lidar ratio, and optical depth. While scattering properties include single scattering albedo, phase function, and particulate backscatter. These then affect the magnitude of cirrus cloud radiative forcing and heating rate. The temperature, humidity, and dynamic formation mechanism in which cirrus develop has a strong influence on their microphysical properties, which then greatly influence cirrus optical and radiative properties (Pruppacher and Klett, 1997; Yorks, 2014). Cirrus can be separated into four sub-types dependent on where, when, and how they form; synoptic, injection, mountain-wave, and cold trap (Sassen 2001). Synoptic cirrus encompass those formed under the influence of large-scale synoptic flow that can elevate moist air, and promote ice crystal nucleation; such as jet stream dynamics, extratropical frontal systems, and Rossby Wave interactions. Injection cirrus are the mesoscale counterpart to synoptic, which form in relation to strong convective updrafts and anvil outflow, or blow off. Globally, injection cirrus are the most

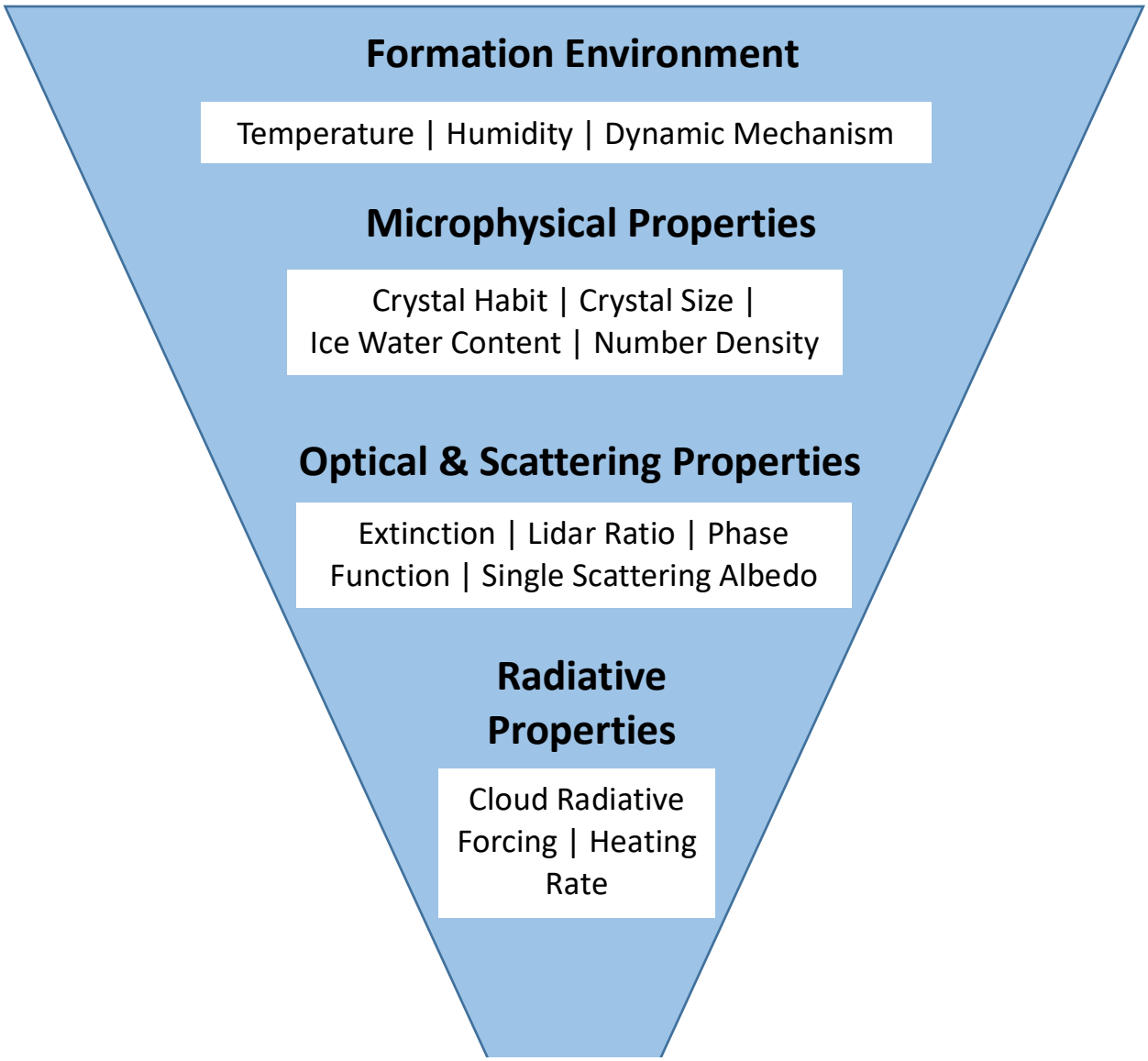

Figure 1.1 Flow chart showing how cirrus properties propagate and depend on their formation environment

common due to the high occurrence frequency of cirrus in the tropics associated with the ITCZ (Nazaryan *et al.* 2008). Here on injection cirrus will be referred to as convective cirrus. Mountain wave cirrus form due to the uplift of air crossing perpendicular over orographic regions, and the resultant rising air in the leeward formed wave. Cold trap cirrus, also referred to as tropical tropopause layer (TTL) cirrus, form as thin tenuous layers

at high altitudes in excess of 15 km and extremely cold temperatures <-70° C (Yorks, 2014). Mountain wave and TTL cirrus are relatively less common, and are not explicitly discussed in this work. It should be noted that there is also a fifth category of cirrus, anthropogenic, that form as contrails when high-altitude aircraft exhaust acts as ice nuclei where conditions are favorable for nucleation. Robust measurements of cirrus, and all associated properties, are key to improving cirrus parameterization in GCMs, and better understanding their impact on the climate.

1.2 Observations of Cirrus Properties

There are many instruments available for measuring cirrus optical and microphysical properties. Passive remote sensors such as radiometers are used to measure the emissivity of cloud layers at specific wavelengths. Liou *et al.* (1990) demonstrated a technique where the emissivity difference between two channels on the polar orbiting advanced very-high-resolution radiometer (AVHRR) were used to calculate cloud optical depth. Sassen and Comstock (2001) used a combination of ground based lidar and radiometer data, known as the LIRAD method (Platt and Dilley 1981), to develop a parameterization for cirrus optical depth based in layer thickness and mid-cloud temperature. These passive remote sensing systems are limited by their inability to provide information on the vertical structure of a layer. Additionally, passive sensors are also susceptible to contamination from additional emitting sources either in front of, or beyond, the intended target layer if not accurately filtered (Meyer and Platnick 2010).

In-situ probes flown on aircraft through cirrus clouds provide valuable measurements of microphysical properties, and have found significant differences between mid-latitude synoptic cirrus and tropical convective cirrus (Sassen and Benson 2001; Wang

and Sassen 2002; Lawson *et al.* 2001; Lawson *et al.* 2006; Yorks *et al.* 2011), implying varying radiative effects for these cirrus types. Lawson *et al.* (2006) reported in mid-latitude synoptic cirrus 99% of the total number concentration of particles were <50μm. Of those crystals >50μm 50% were made up of rosette like habits, 40% were irregularly shaped, and the remaining few percent exhibited column or spheroidal habits. This agrees with Lawson *et al.* (2001) who found a high percentage of rosette shaped crystals in mid-latitude cirrus based on observations using the Cloud Particle Imager (CPI). Examples of ice crystal habits imaged by CPI are shown in Fig 1.2, observed during the Radiative Effects of Thin Cirrus (REThinC) Campaign out of Houston, TX in August 2017. Conversely, column, plates, and aggregate habits have been more commonly observed in anvil cirrus, while rosettes less frequent (Lawson *et al.* 2006). Convective cirrus exhibit a higher concentration of larger particles on the order of 100-400μm, and IWC is also higher in convective cirrus compared to synoptic (Lawson *et al.* 2010; Noel *et al.* 2004). It has been found that ice crystal size distributions in cirrus layers are often bi-modal, including a small (<100μm) mode and a larger mode (Mitchell *et al.* 1996; and Koch 1996). Zhang *et al.* (1999) showed modeled net cirrus radiative forcing was lower when a bi-modal size distribution was assumed. In-situ probes are a key component in collecting direct measurements of cirrus microphysical properties, however these instruments also have difficulty providing vertical profiles of data and are also subject to potential shattering errors within measurements (Zhao *et al*. 2011).

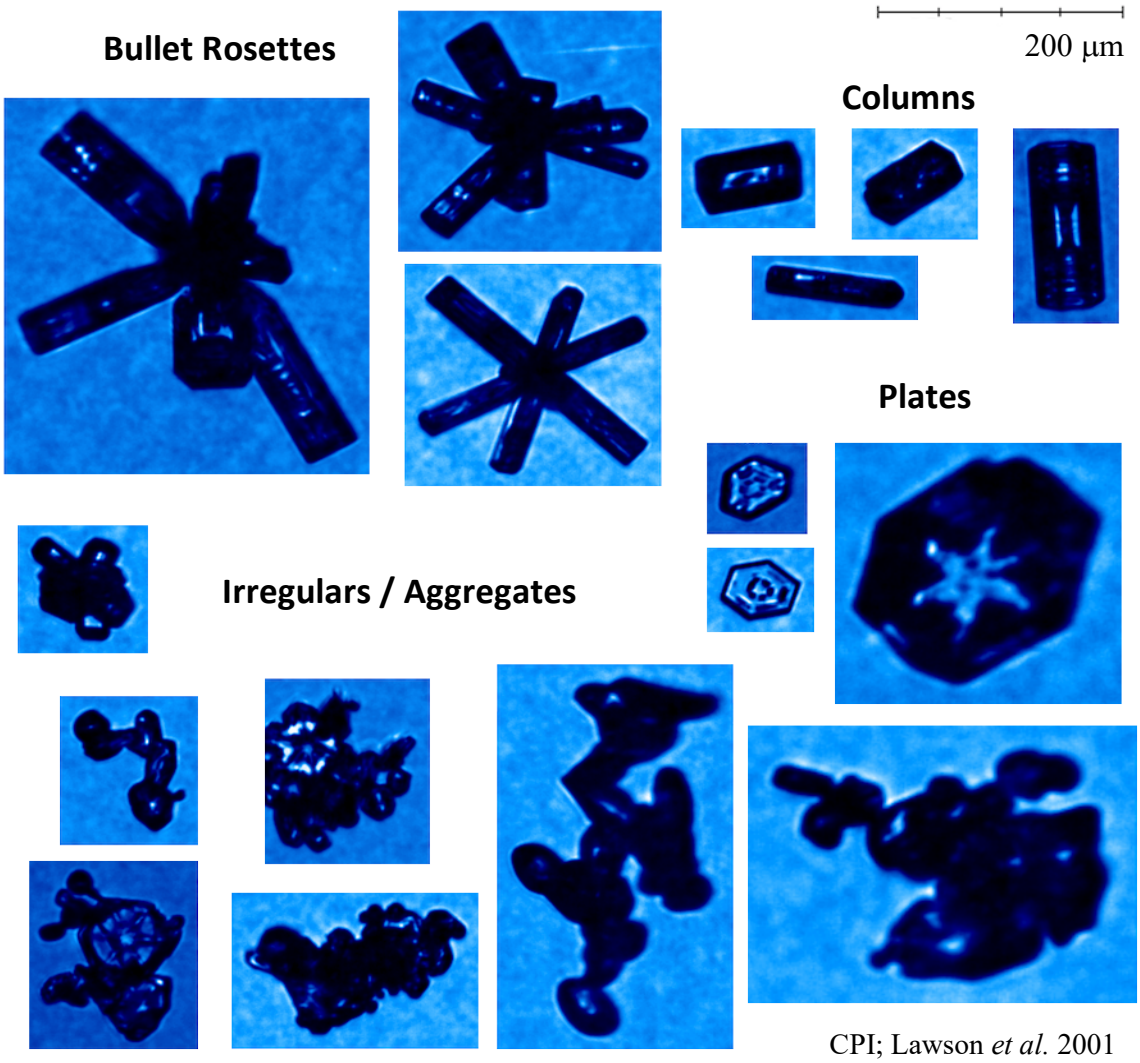

Figure 1.2 Images of varying cirrus crystal habits observed with the Cloud Particle Imager (CPI) during the ReThinC Campaign out of Houston, TX in August 2017

The microphysical properties influence cirrus optical and scattering properties, and their associated radiative properties. Radiative forcing principles are discussed further in Chapter 3, and involves modeling atmospheric SW and IR irradiances (Wm^{-2}) through the use of radiative transfer (RT) simulations. The influence on surface temperature through sustained TOA RF is defined as $\Delta T = \lambda * RF$, where λ represents a climate sensitivity parameter (Myhre *et al.* 2013). The sensitivity parameter can vary substantially based on

the atmospheric phenomena causing the forcing, the horizontal distribution of forcing, and also with latitude (Forster *et al.* 2007; Shindell and Faluvegi, 2009).

One of most influential optical properties is the estimated extinction, integrated to calculate cloud optical depth (COD), which expresses how much signal is removed from an incident beam due to absorption and scattering. Cirrus TOA total radiative forcing is generally positive and increases with COD to a critical value where the magnitude starts to decrease until eventually becoming negative. Due to cirrus non-linear interactions between their environment and physical properties along with model, parameterization, and dataset differences there is no consensus on these critical COD values (Hong & Liu 2015; Campbell *et al.* 2016; Ozog *et al.* 2019).

Cirrus RT simulations represent cloud layers using optical and microphysical properties often observed from remote sensing platforms, and then parameterize the associated scattering effects. Current cirrus scattering parameterizations in radiative transfer models are limited to a single crystal shape assumed randomly oriented throughout the cloud layer unless otherwise developed to have an explicitly defined habit mixture (Baum *et al.* 2005; Key *et al.* 2002; Yang *et al.* 2005; Yang *et al.* 2013). McFarquhar *et al*. (2000) found tropical thin cirrus have a RF as high as 5 Wm^{-2} with an average of 1.58 Wm^{-2} using lidar derived extinction values, and assumed column crystal habits. Hong *et al.* (2016) calculated the zonally averaged cirrus RF over all latitude belts for a range of varying optical depths, and found forcing to be up to 15 Wm^{-2} in the tropics. The mid-latitudes exhibited a seasonal dependence with values as low as -30 Wm^{-2} in the summer, and 10 Wm^{-2} in the winter. This study used optical depths retrieved from the *CloudSat* (Stephens *et al.* 2002) satellite radar, and the Cloud-Aerosol Lidar and Infrared Pathfinder

Satellite Observations (CALIPSO; Winker *et al.* 2009) satellite lidar with the globally assumed crystal habit limited to an aggregate crystal (Yang *et al.* 2000, Yang *et al*. 2005). Campbell *et al.* (2016) looked at a year of daytime mid-latitude zenith pointing lidar data, and found an estimated RF of 0.07-0.67 Wm^{-2}. This study also identified very thin cirrus as having a net negative RF. Zhang *et al*. (1999) performed a modeling studying on the sensitivity of cirrus RF to varying microphysical properties. This study determined that cirrus with a bi-model distribution of crystal sizes, common in cirrus clouds, had a greater potential to exhibit a net negative RF. The same study also found a net negative RF in cirrus with a large number density ($>10^7$ m^{-3}) of small crystals (<30 μm).

The IPCC AR5 (Boucher *et al.* 2013) reports cirrus microphysical mechanisms may be missing from GCMs leading to uncertainty if cirrus induce positive, negative, or neutral feedbacks. Reducing assumptions and uncertainties in cirrus layer properties incorporated into model studies is crucial to improving our understanding of cirrus, and is an imperative area of climate change research (McFarquhar *et al.* 2000; Lee *et al.* 2009; Yorks 2014). This will become even more important as cirrus spatial and temporal patterns change in a future warmer climate. Current GCMs estimate a decrease in cloud coverage along the ITCZ and mid-latitude storm-track regions (Chou and Neelin 2004; Held and Soden 2006; Boucher *et al.* 2013). Displacing cloud coverage to higher latitudes, which currently have relatively low cirrus frequencies (Sassen *et al.* 2008), though these regions are the most sensitive to global warming.

Currently, lidar instruments are an invaluable tool for studying cirrus clouds, and their effects on the climate. Passive remote sensors such as MODIS & VIIRS are limited by their inability to obtain the vertical structure of cirrus clouds. In-situ probes flown

through cirrus layers provide much needed direct measurements of ice water content, extinction, crystal size, and crystal shape, however, these instruments are limited by their inability to provide full vertical profiles (Zhao *et al.* 2011). Active remote sensing radar systems like *CloudSat*, which similarly transmit and detect backscattered radiation, often cannot detect thinner cirrus at the longer wavelengths in which they operate (Comstock *et al.* 2002). Additionally, the importance of these optically thinner cirrus layers is amplified by their prevalence. Cirrus clouds with optical depths less than 0.3, categorized as thin by Sassen and Cho (1992), have been found to be the most common among cirrus clouds (Mace *et al.* 2009; Stubenrauch *et al.* 2013).

1.3 Cirrus Profile Retrievals and Lidar Techniques

There are several different types of lidar designed for measuring varying atmospheric phenomena. The two most commonly used for retrieving cloud and aerosol profiles are standard backscatter lidars and high spectral resolution lidars (HSRL). Both of these lidar systems measure the elastic backscatter of emitted laser light from atmospheric molecules and particles. Lidars are valuable because their retrievals provide full atmospheric profiles of cloud and aerosol spatial and optical. This data is provided at both temporal and spatial resolutions that cannot be met by in-situ instruments, passive remote sensors, or similar radar remote sensors alone. Note that lidars are limited to the optical depths they can penetrate, and the signal becomes fully attenuated in thick water clouds or convective systems.

Standard backscatter lidars are currently the most common lidar used for retrieving profiles of clouds and aerosols, and have been deployed in space, airborne, and ground based platforms. These types of lidar are the least complex to implement, relatively

inexpensive, and have been providing reliable ground and air-based measurements for decades (McGill *et al.* 2015; Winker *et al.* 2010; McGill *et al.* 2003, Welton *et al*. 2001). The NASA Cloud Physics Lidar (CPL), further discussed in Chapter 4, is a standard backscatter lidar that flies on the NASA ER-2 high altitude aircraft, and has flown on over two dozen field campaigns since its first deployment in 2000. CPL operates at 355nm, 532nm, and 1064nm wavelengths, and produces optical properties in its visible and near infrared (NIR) channels (McGill *et al.* 2002). Standard backscatter and HSRL lidars primarily retrieve atmospheric profiles of attenuated total backscatter (ATB; Eq. 1.1) from

$$\gamma(r,\pi) = \frac{N(r)\, r^2}{C} = \beta(r,\pi)T^2(r,\sigma) \qquad \text{Eq. 1.1}$$

$$\beta(r,\pi) = \beta_P(r,\pi) + \beta_M(r,\pi) \qquad \text{Eq. 1.2}$$

$$T^2(r,\sigma) = exp\left\{-2\int[\sigma_P(r) + \sigma_M(r)]\, dr\right\} = T_m^2 T_P^2 \qquad \text{Eq. 1.3}$$

their raw signal. The ATB (γ) is referred to as the total because it is composed of both the molecular (Rayleigh) and a particulate (Mie) signal components, and is calculated at each lidar range bin (r). The ATB, however, yields no additional information of these signal components. ATB can be written as a function of the backscatter (β) and extinction (α) coefficient optical properties, which also both contain a molecular (β_m, α_m; Eq. 1.2) and particulate component (β_p, α_p; Eq. 1.3), respectively.

The lidars discussed in this work are photon counting where N*(r)* is the number of photons per range bin that have been backscattered by the atmosphere into the lidar detectors. $T^2(r,\alpha)$ is the two-way transmission, a unitless measurement normalized to 1.0 that indicates the amount of signal loss due to attenuation. The value C in Eq. 1.1 is a

generalized variable indicating the calibration factor, which accounts for instrument parameters calculated by fitting the signal to a Rayleigh profile retrieved from temperature, pressure, and humidity observations. The molecular components of both the backscatter and extinction coefficients can be computed from this Rayleigh profile, which is calculated from either model data or a World Meteorological Organization (WMO) upper air

$$S_P = \frac{\alpha_P}{\beta_P} \qquad \text{Eq. 1.4}$$

radiosonde balloon launch. Once this is done the two particulate components (β_P & α_P) are the only unknowns remaining, however, with only the single lidar equation. To calculate these particulate components a variable representing the extinction-to-backscatter ratio (Eq. 1.4) must be assumed constant through the layer observed. This is known as the lidar ratio, which is used to reduce the number of unknowns down to one allowing for a forward inversion of the lidar equation (Fernald *et al.* 1972; Klett 1981).

This is the primary challenge in calculating optical properties from standard backscatter lidar data. The lidar ratio used is assumed to be homogeneous throughout a given particulate layer profile, whether it is a cirrus cloud, water cloud, or an aerosol layer. Lidar ratios can vary from 10 to 100 steradians (sr) depending on the type of cloud or aerosol. The error in this assumed lidar ratio propagates through to the calculation of the optical properties. This further propagates into any parameterization or model that incorporates the derived quantities. Young *et al.* (2013) showed that an error of 40% in the assumed cirrus lidar ratio can cause up to 100% error in the retrieved cirrus extinction.

The benefit of an HSRL is that a lidar ratio does not have to be assumed when calculating optical properties. HSRL lidars contain an additional filter within their receiver sub-system for differentiating the signal between its molecular and particulate components.

This will be referred to as the HSRL technique, and their subsequent products as HSRL optical properties. It is made possible by taking advantage of the difference in spectral broadening that light undergoes when scattered by air molecules as compared to atmospheric particles. At visible wavelengths particles broaden the signal approximately 10^{-5} nm (Esselborn *et al.* 2008), and air molecules will broaden the signal two orders of magnitude greater around 10^{-3} nm (Young 1981). This greater broadening from the air molecules is caused by their high velocities due to random thermal molecular motion. Unlike standard backscatter lidars, which utilize only one channel at each wavelength they operate (unless they have depolarization capabilities), HSRLs will use more than one channel for a given wavelength, those sensitive to retrieving the molecular signal and those for the particulate signal. However, HSRL systems are less common than standard backscatter lidar due to their expensive cost, more complex design, and increased sensitivity to laser stability. Only a few HSRL systems have been operational from ground or airborne platforms.

There are two common receiver architectures deployed in HSRL systems to achieve the separation of Rayleigh and particulate signals. The first method uses an iodine vapor absorption cell. This cell acts to filter out the central wavelength of the emitting laser, and the weakly broadened particulate signal, and measures the Rayleigh backscatter which has been broadened by two orders of magnitude greater. These system have two channels, one for measuring the total signal (Rayleigh plus particulate) and another for measuring the filtered Rayleigh signal. The particulate signal can then be inferred by taking the difference of the two signals. A benefit of the iodine filter method is it has absorption lines at 532nm allowing for the use of Nd:YAG lasers, which are common among standard backscatter

lidars and readily available. However, I drawback to the iodine filter method is the particulate signal and associated optical properties are not directly calculated, but rather inferred from the difference in the total and Rayleigh signal.

Another HSRL method uses a Fabry-Perot interferometer, also known as an etalon, to discriminate the signal between its molecular and particulate components. An etalon consists of two parallel optically flat plates with reflective dielectric coatings on their respective sides facing one another. Light transmitted through an etalon appears as a fringe pattern on the imaging plane. Placing an array of detectors across this pattern yields information on the separate signal components. This method uses a linear array of multiple detectors rather than just a single channel for each component, and is therefore referred to as the multi-channel (MC) technique. A benefit of the etalon method is it allows for the direct retrieval of particle optical properties rather than inferring the particle signal. This method is discussed further in Chapter 2. The NASA Airborne Cloud Aerosol Transport System (ACATS) is a multi-channel HSRL designed for operation aboard the NASA ER-2 high altitude aircraft. ACATS was the first HSRL capable of retrieving nominal cirrus observations for an operational altitude of 20k feet aboard the ER-2 (Yorks *et al.* 2014). An iodine filter HSRL has operationally flown on science campaigns aboard the NASA King Air B-200 (Hair *et al.* 2008) and DC-8, however, these aircraft do not readily fly at altitudes high enough for cirrus observations. Yorks (2014) showed ACATS HSRL retrieved cirrus extinction had uncertainties 25-50% lower than coincident measurements from the Cloud Physics Lidar (CPL) standard backscatter system. Though HSRL systems are considered to yield atmospheric optical properties with reduced uncertainties, there is

still little known how this translates into modeling benefits that incorporate these observations.

1.4 Objectives

The ACATS lidar is inherently both an HSRL and a Doppler wind lidar capable of measuring wavelength shifts across its detector array to retrieve line-of-sight winds. ACATS has flown in two science campaigns aboard the ER-2; the Wallops Airborne Vegetation Experiment (WAVE) in 2012 out of Wallops Island, VA, and the CALIPSO CATS Airborne Validation Experiment (CCAVE) out of Palmdale, CA in 2015. HSRL retrievals were inconsistent during both of these campaigns due to poor calibration of the ACATS etalon, which accounts for imperfections in its mirror optics. Initial designs strategies were to utilize the near field Rayleigh signal in the clear air below the ER-2 for calibration, however, this proved to be too weak due to the high altitude nature of the aircraft. Chapter 2 discusses methods of a new ACATS etalon calibration technique I helped test and design. Once optimized, the improved etalon calibration values were tested to investigate how they impacted cirrus layer HSRL optical properties and vertical wind velocity retrievals.

Despite the important role cirrus play in Earth's radiation budget their diurnal impact has had few platforms to be adequately studied. Ground based lidars provide nearly 24 hour temporal coverage, however, are limited to a single point locations (Sassen *et al.* 2003; Campbel *et al.* 2016; Lolli *et al.* 2017). The CALIPSO satellite lidar has provided a robust understanding of cirrus properties on the global scale (Sassen *et al.* 2008; Nazaryan *et al.* 2008; Haladay & Stephens 2009; Hong *et al.* 2016), however, the sun-synchronous orbit of the CALIPSO satellite provides only a snapshot of the diurnal cycle with a single

day and night observation at 13:30 and 01:30 local solar time, respectively. In Chapter 3 utilize the entirety of the nearly 3-year Cloud Aerosol Transport System (CATS) dataset, which operated aboard the International Space Station (ISS) from January 2015 to October 2017. CATS had 3 operational science modes: Mode 7.1, 7.2, and 7.3. Due to laser failures mode 7.1 and 7.3 became inoperable early on in its deployment. Mode 7.2 operated for 31 months from April 2015 till October 2017 primarily collecting data in the near IR at 1064nm, and makes up the entirety of the CATS data discussed in this work. The unique ISS orbit allows for observations at all times of day with a inclination angle between 51° North and South latitude, which provides coverage of the tropics and majority of the mid-latitude regions. Using CATS I investigate the diurnal trend of cirrus optical properties across all seasons, and incorporate these observations into a radiative transfer model to better constrain the day and nighttime net annual global mean cirrus radiative forcing at the top of the atmosphere.

Though HSRL systems can directly retrieve lidar ratios, when conditions are favorable the lidar ratio in a standard backscatter system may be constrained and retrieved rather than using a climatological value. This occurs when a non-attenuating layer is bounded between two aerosol free clear air regions. An iterative process determines the best fit lidar ratio based on the reduction in the two-way molecular transmittance (T_m^2; Eq. 1.3) in the CPL molecular signal below the layer (Fernald *et al.* 1972; Spinhirne *et al.* 1980). These conditions often occur in cirrus observed by CPL from the stratospheric platform of the NASA ER-2. However, space-borne lidars have a lower signal-to-noise ratio (especially during daytime operations) resulting in infrequent constrained lidar ratio retrievals. In Chapter 4 I use a large CPL dataset comprised exclusively of constrained

cirrus observations from multiple campaigns to investigate radiative effects of convective and synoptic cirrus. By using only constrained optical properties, and accurately configuring the model to the environment conditions of the cirrus layers I develop robust statistics of their radiative forcing, and how this contrasts with the estimates discussed in Chapter 3 utilizing gridded regional mean profiles.

Chapter 2: Advancing ACATS Calibration Impacting Cirrus HSRL and Vertical Wind Retrievals

2.1 ACATS Overview

The NASA ACATS lidar is a photon counting multi-channel fringe imaging Doppler wind lidar (DWL) that operates in the visible spectrum at 532 nm (Yorks *et al.* 2014). ACATS employs a Fabry-Perot interferometer, also known as an etalon, as its high spectral resolution filter to detect the small frequency shifts in detected photons. The etalon was developed by Charles Fabry and Alfred Perot in 1897, and is a common tool in laser receiver architecture (Vaughan 1989). The MC wind lidar technique has been deployed and demonstrated on previous ground-based systems (Benedetti-Michelangeli *et al.* 1972; Abreu *et al.* 1992; McGill 1996). The ACATS system is similar to the ground-based MC DWL operated the University of Michigan (McGill *et al.* 1997a), adapted for operations aboard the NASA ER-2 as the first airborne MC DWL.

An etalon consists of two parallel optically flat plates with reflective dielectric coatings on their respective sides facing one another. The opposite sides not facing each other are transparent, allowing light to enter and exit the etalon. Light that enters the etalon is transmitted through the first plate into the cavity between the two plates where it undergoes multiple beam interference (McGill *et al.* 1997a). Multiple beam interference consists of light undergoing both constructive (magnitude increase) and destructive (magnitude decrease) interference within the etalon resulting in a ringed fringe pattern on the imaging plane. Most light is reflected back out of the etalon, which is discarded, and a small percentage is transmitted through forming the fringe pattern. Figure 2.1 depicts the fringe pattern from the CATS etalon where the green rings represent light that has

undergone constructive interference, and the black space where destructive interference has occurred. At any point on a ring of the fringe pattern each radius corresponds to a unique wavelength of light. With the respective wavelengths increasing with radius. The difference between the peak transmission of each fringe ring is referred to as the free spectral range ($\Delta\lambda_{FSR}$; Eq. 2.1). The FSR is a function of the incident wavelength entering the etalon (λ), plate spacing (d), and the index of refraction between the plates (μ). ACATS uses an air gap etalon where the index of refraction is assumed to be 1.0 between the two plates spaced 10 cm apart. This corresponds to an FSR of 1.4 picometers. The multi-channel fringe imaging technique utilizes an array of detectors across the interferometer fringe pattern with each detector in the array corresponding to small difference in wavelength to the adjacent detectors. The free spectral range can also be represented as the

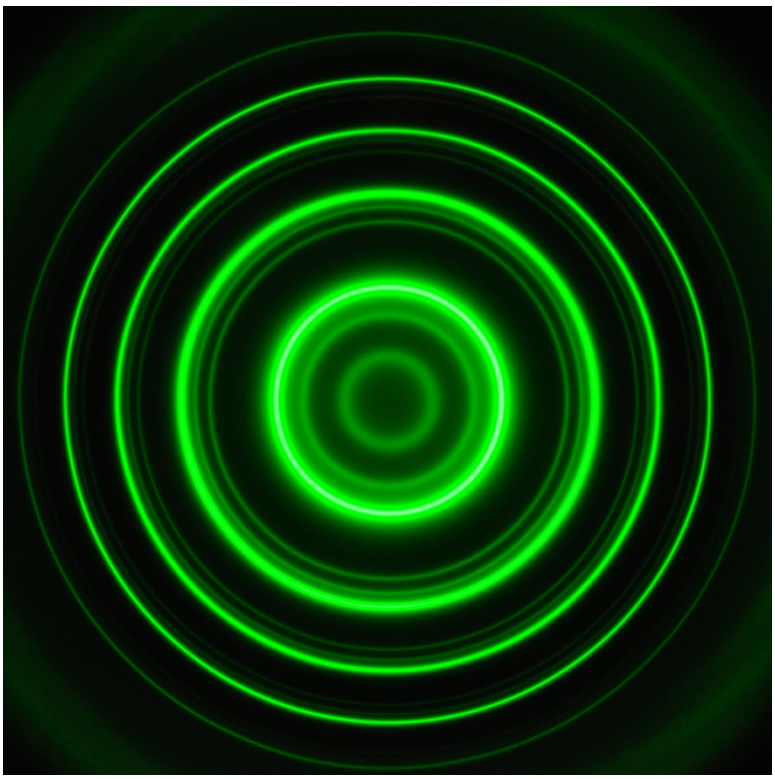

Figure 2.1. Fringe pattern through the etalon of the CATS instrument. (Credit: Stan Scott; GSFC)

$$\Delta FSR_\lambda = \frac{\lambda_o^2}{2\mu d} \qquad \text{Eq. 2.1}$$

number of detector channels across which an entire $\Delta\lambda_{FSR}$ is measured, N_{FSR}. The ACATS N_{FSR} is 20 channels, and since it has an array of 24 detector channels approximately 1.2 free spectral ranges (or orders) of the etalon fringe pattern are sampled. Figure 2.2 shows a schematic for the ACATS receiver from Yorks *et al.* (2014). In order to better sample the circular fringe pattern produced by the etalon, ACATS uses a holographic circle-to-point converter (McGill *et al.* 1997b) to focus the circular pattern onto the detector array. As shown in Fig. 2.2, after the incoming laser light is transmitted through the etalon it is focused by a lens onto the holographic optical element (HOE) where the circular fringe signal is focused down to a point on each of the 24 detectors. The circle-to-point converter

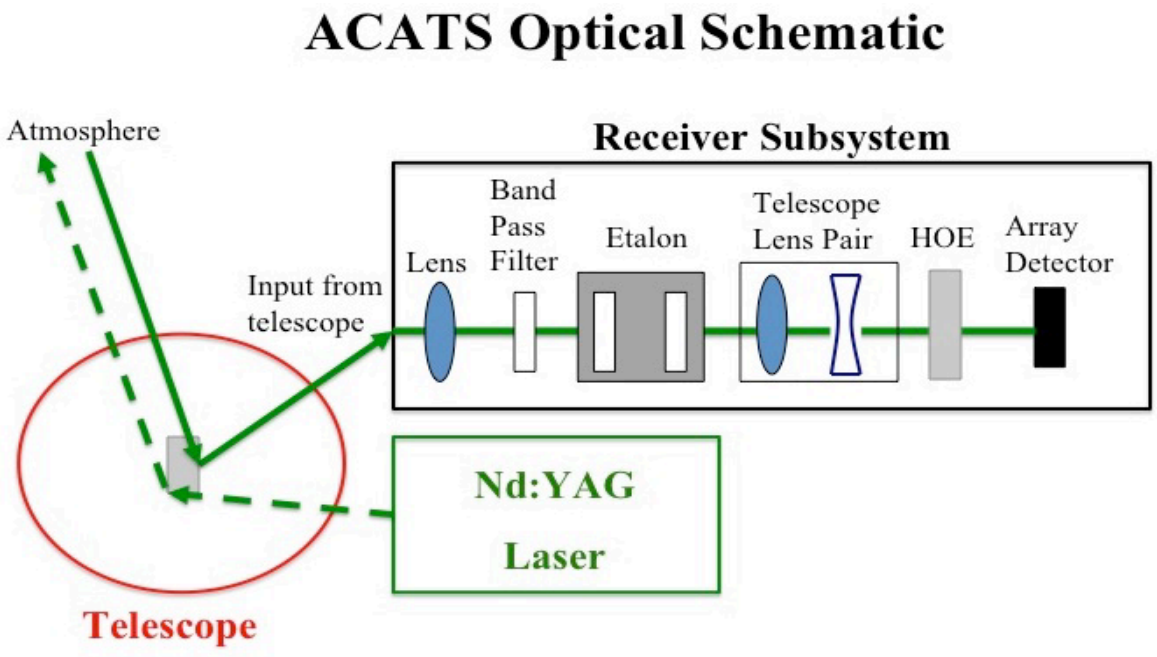

Figure 2.2 Schematic for the ACATS system where original emitted laser photons is depicted by the dashed green line, and scattered incoming photons into the receiver are depicted by the solid green line

HOE improves measurement efficiency and allows for the use of photon counting detectors (Yorks *et al*. 2014).

2.2 Multi-Channel System

As ACATS operates only at 532nm it is optimized for retrievals in atmospheric particulate layers of clouds and aerosols, but not in clear air regions consisting of only a molecular signal. As mentioned in Chapter 1 the MC method in these aerosol regions is made possible by the difference in spectral broadening light undergoes when scattered by air molecules compared to atmospheric particles. Figure 2.3a shows an idealized transmission spectrum of a signal that has been broaden by both air molecules and particulate matter. The blue curve represents the wide broadening caused by the air molecules, while the red curve represents the narrow broadening caused by the particulates. The shaded area on Fig. 2.3a represents the spectral range which ACATS is sensitive. Figure 2.3b shows an idealized signal ACATS would observe across its detector array in a given range bin containing aerosol or cloud particles. The blue curve in Fig. 2.3a represents

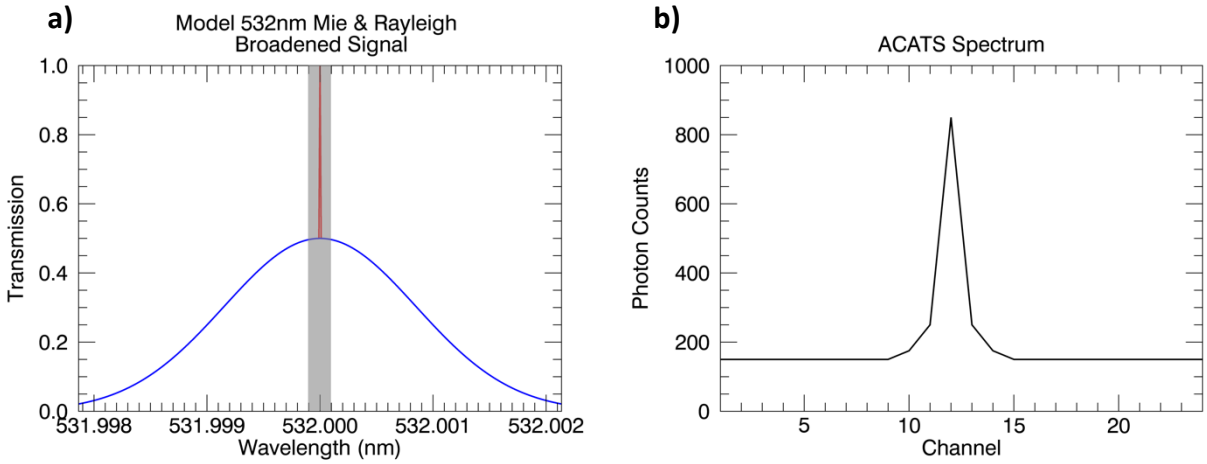

Figure 2.3 (a) Signal broadening at 532nm for mie (red curve) and Rayleigh (blue curve) signal. **(b)** Idealized ACATS signal across 24 channel detector array of shaded area in (a).

the Rayleigh broadened signal, and the strong peak observed in each plot is due to particulate backscatter. In the narrow spectral range of the ACATS system the Rayleigh signal appears as a flat line in Fig. 2.3b at around 150 photons per channel. Note Fig 2.3b ideally represents the shape of backscattered signal, but not necessarily realistic photon count values. The observed peak corresponds to the center of a fringe ring the detector array samples. The difference between the peak location in the outgoing laser pulse and return signal is the Doppler shifted wind signal.

The channel which the peak ACATS signal is observed is dependent on several factors: the Doppler shift of the received signal, laser stability, and etalon stability (gap spacing). The ACATS etalon has a dynamic wind velocity range of approximately 400 ms^{-1} corresponding to a LOS wind velocity resolution of 20 ms^{-1} per channel, or a 0.060 picometer Doppler shift. This means the laser center frequency and etalon gap must be controlled at a sub-picometer accuracy to prevent drift in the signal. The ACATS laser is a frequency-doubled Nd:YAG injection seeded laser with a liquid heating & cooling loop to provided thermally stable operations. As the ACATS lidar warms after start-up fluctuations in laser energy can cause the peak signal to drift across the detector array before stabilizing. Additionally, thermal variations can cause changes in the etalon gap spacing, which also contributes to peak drift. The three posts connecting the parallel etalon mirrors are piezoelectric actuators, which modulate the etalon gap with applied voltages. ACATS software checks on regular 10 second intervals that the peak signal is located in Channel 4, and is able to apply small adjustments to the gap using the etalon actuators reducing drift of the outgoing reference signal. Figure 2.4 shows drift tests I conducted on the ACATS laser across its detectors when automated etalon control is engaged (Fig. 2.4a) and disabled

(Fig. 2.4b). The peak wavelength of the ACATS laser in Fig. 2.4b is observed to decrease soon after start-up, dropping down into Channel 2 before slowly rising to a stable state between Channel 11 and 12 after approximately four hours. Fig. 2.4a shows the efficiency of the etalon control software at keeping the laser peak between Channel 4 and 5 for the duration of operation. This stability observed between the etalon gap and the laser central wavelength is a key component needed in ACATS processing to retrieve HSRL and wind products.

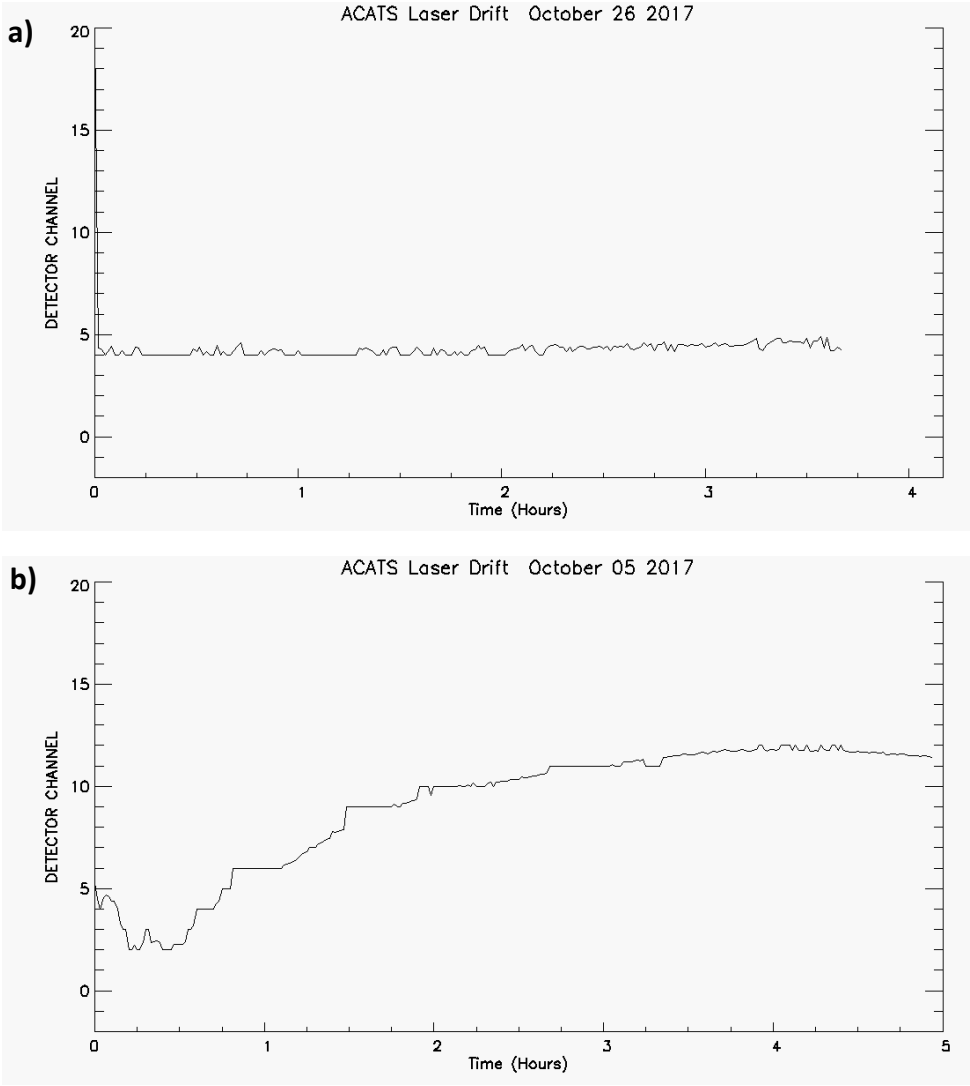

Figure 2.4 (a) ACATS laser drift across channels with etalon peak control algorithm enabled. (b) ACATS laser drift across detector channels with no control.

2.3 ACATS Processing

ACATS raw data are limited to its 24 channels which correspond to a wind measurement precision of approximately 20 ms^{-1}. However, post processing algorithms use an iterative least squares fitting technique of the ACATS lidar equation (Eq. 2.4) to the raw signal, which results in sub-channel precision on the order of 1 ms^{-1}. Taking into account ACATS multi-channel etalon design, a function for photon counts per channel can be derived similar to that for the standard backscatter lidar equation (Eq. 1.1). McGill *et al.* (1997a) showed that by convolving the etalon transmission function (Eq. 2.2) with the standard backscatter lidar equation you derive the multi-channel lidar equation (Eq. 2.4) for photon counts per channel. Like the standard backscatter lidar equation, the MC lidar equation can be broken into its instrument components and atmospheric signal components. The first term in Eq. 2.4 represents the instrument components with the primary difference to the standard backscatter lidar equation being the additional channel variables $\eta(j)$ and n_C. The second term in Eq. 2.4 is comprised of the molecular and particulate signal components, similar to the standard equation, with the addition of etalon transmission terms. The attenuated particulate backscatter is represented by α (expanded in Eq. 2.5), and the attenuated molecular backscatter is represented by ω (expanded in Eq. 2.6). The sum of the attenuated molecular backscatter and the attenuated particulate backscatter is equivalent to the total attenuated backscatter (γ) retrieved by standard backscatter lidars discussed in Chapter 1. Lastly, the third term characterizes the Doppler shift imparted to the signal with U_{LOS} representing the line-of-sight wind velocity in ms^{-1}. There are three unknown variables in Eq. 2.4 being α, ω, and U_{LOS}, and with the 24 detector channels this is an over determined equation. These three parameters are solved for by

$$T(\Delta\lambda, j) = \sum_{n=0}^{\infty} A_n cos\left[2\pi n\left(\frac{\Delta\lambda}{\Delta\lambda_{FSR}} + \frac{j}{N_{FSR}}\right)\right] sinc\left(\frac{n}{N_{FSR}}\right) \qquad \text{Eq. 2.2}$$

$$A_n = 2\left(1 - \frac{1}{1-R}\right)^2 \left(\frac{1-R}{1+R}\right) R^n e^{-4\pi n^2 \Delta d_D^2 \lambda_o^2} \qquad \text{Eq. 2.3}$$

Table 2.1 Etalon Transmission Function Variables

Variable	Description
A_n	etalon transmission parameter
j	ACATS channel number
n	number of iterations
R	Etalon plate reflectivity
N_{FSR}	Number of channels per FSR
$\Delta\lambda_{FSR}$	Etalon free spectral range
$\Delta\lambda$	Wavelength offset of initial wavelength and scan wavelength
λ_o	ACATS native wavelength
Δd_D	Etalon defect parameter

$$N(r, j) = \frac{E_T \lambda}{hc} O_A(r) \frac{A_T}{4\pi r^2} \Delta r Q_E T_O T_F(\lambda) \frac{\eta(j)}{n_C}$$

$$\times \sum_{n=0}^{\infty} A_n sinc\left(\frac{n}{N_{FSR}}\right) exp\left(\frac{-\pi^2 n^2 \Delta\lambda_L^2}{\Delta\lambda_{FSR}^2}\right)\left[\alpha(r) + \omega(r)\, exp\left(\frac{-\pi^2 n^2 \Delta\lambda_M^2}{\Delta\lambda_{FSR}^2}\right)\right]$$

$$\times\ cos\left[2\pi n\left(\frac{\lambda_O - \lambda_C}{\Delta\lambda_{FSR}} - \frac{2U_{LOS}(r)\lambda_O \sin\varphi}{c\,\Delta\lambda_{FSR}} - \frac{j}{N_{FSR}}\right)\right] \qquad \text{Eq. 2.4}$$

$$\alpha(\pi, r) = \beta_P(\pi, r) \exp\left(-2\int_0^r \sigma(r)\, dr\right) \qquad \text{Eq. 2.5}$$

$$\omega(\pi, r) = \beta_M(\pi, r) \exp\left(-2\int_0^r \sigma(r)\, dr\right) \qquad \text{Eq. 2.6}$$

expanding and linearizing Eq. 2.4 in a Taylor series, and then using an iterative weighted least squares fitting technique developed by McGill (1996) where it was first proven, and

later adapted for ACATS processing (Yorks *et al.* 2014). Here on referred to as the three-parameter fit.

2.4 Improved ACATS Etalon Calibration

Before performing the three-parameter retrieval the ACATS etalon must first be calibrated. A perfect theoretical etalon would be completely parallel and would have 100% transmission at the peak of each fringe ring with no signal broadening. However, a signal through a real etalon exhibits broadening effects from several sources such as plate imperfections and aberrations due to inexact parallelism (Vaughn 1989; McGill 1996). A general instrument parameter called the defect parameter (Δd_D) in Eq. 2.3 is used to account for etalon defects. Each detector channel has its own unique defect parameter with units of nanometers. Figure 2.5 shows the etalon transmission function for an etalon with the same specifications as ACATS; a reflectivity (R) of 0.86, estimated plate loss (L) of 0.05, and an air gap of 10 cm. These values are provided by the etalon manufacturer, Michigan Aerospace. The red curve represents the transmission assuming no defect of 0 nm across all channels. The blue dashed curve depicts the resultant broadening of the signal through the etalon due to a defect parameter of 30 nm across all channels. Note that Fig. 2.5 is plotted with a higher spectral resolution than 24 channels to better display the etalon transmission and defect variability. Defect values are often non-uniform across all channels, and would cause the curves in Fig 2.5 to be asymmetric. Each peak in Fig. 2.5 is analogous to the center of a ring on the fringe pattern (Fig. 2.1) produced by an etalon, with the difference in wavelength between each peak equal to the 1.4 picometer free spectral range ($\Delta\lambda_{FSR}$).

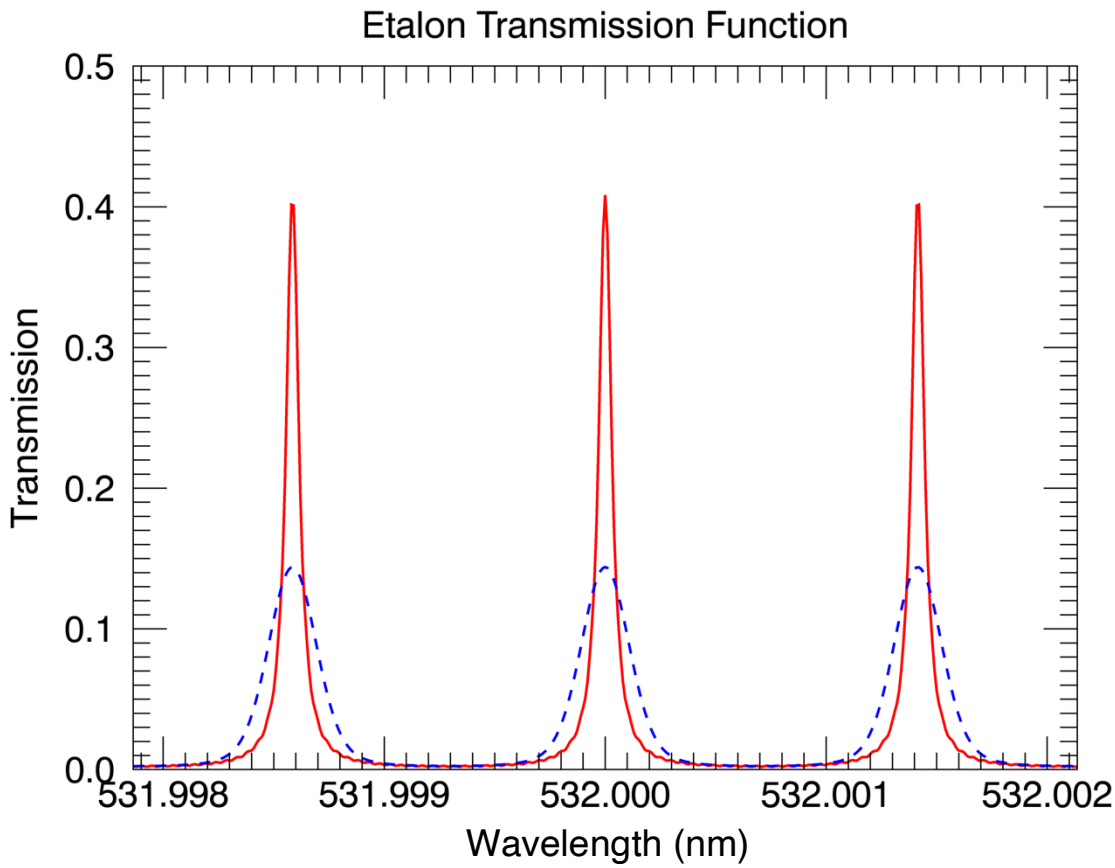

Figure 2.5 Etalon transmission function from Eq. 2.2 with R = 0.86 and L = 0.05. Red curve represents transmission assuming zero defect across all channels ($\Delta d_D = 0$ nm) and the blue dashed curve assuming a defect of 30 nm across all channels ($\Delta d_D = 30$ nm)

The three posts connecting the etalon reflective plates are piezoelectric actuators. These posts keep one of the plates stationary while small voltages applied to the posts move the opposite plate allowing for high precision control of the etalon gap and parallelism. In order to determine the defect parameters for the ACATS etalon the instrument response for each channel must be measured. This is done by having the ACATS software conduct what is called an etalon scan. During an etalon scan the gap is adjusted at predefined intervals for a given number of steps, which changes the alignment of the outgoing laser with the central wavelength of the etalon. This causes the peak signal to move across the ACATS 24 channel detector array. By performing a sufficient number of steps you obtain a

measured etalon response function for each of the 24 channels (Yorks 2014; McGill *et al.* 1997a). The defect value is then determined using an iterative least squares fitting procedure of the etalon transmission function (Eq. 2.2) to the ACATS measured response in each channel. This iterative process starts with a defect value of 0.0 increasing by intervals of 1.0, and the defect value which yields the best reduced chi squared value is determined to be the defect parameter for that channel.

Since 2012 the ACATS instrument has flown in three field campaigns aboard the NASA ER-2 where etalon calibration was inconsistently reliable. Additionally, defect values calculated from etalon scans performed with zenith pointing lab tests cannot be transferred to airborne datasets due to operational environment differences. The temperature and pressure of the ACATS instrument inside the ER-2 wing super-pod at an altitude of 20 km are greatly different versus lab conditions at NASA Goddard. Lab operating conditions are climate controlled at approximately sea level surface pressure, while flight conditions can range from 203 – 223 K at approximately 200 mb. The ER-2 super-pod uses a pressure release valve on an air canister inside the pod to retain an ambient pressure of approximately 3 PSI. Though this is less stable than ambient synoptic air pressure fluctuation. Thus, etalon scans must be performed during in-flight operations under the same conditions that the etalon has been operating during nominal data collection. In addition to similar environmental conditions, etalon defect values are nominally retrieved when the signal incident on the etalon during a scan is uniform. During previous field campaigns defect values retrieved from in-flight etalon calibration scans were inconsistently reliable due to the non-uniformity of the signal. This is due to the varying cloud and aerosol scene observed at the ER-2 average speed of 200 ms^{-1}.

Originally, near field return was the intended target for signal integration during etalon scans, however, the weak molecular signal at the high operational altitudes made this an unviable option.

Figures 2.6a and b shows example calibration fits from etalon scans performed during ACATS most recent field campaign in August of 2015. The measured channel response is shown by the red curve, and the fitted transmission function is shown by the blue curve. Fig. 2.6a depicts the response in Channel 1 from an etalon scan performed during a flight on August 19th, 2015. The response in Fig. 2.6a exhibits the expected periodic structure, however, the signal was noisy and calibration yielded a high biased defect value. Fig 2.6b shows the response in Channel 13 from a flight the following day on August 20th, 2015, and is an example of a poor channel response from an in-flight etalon scan. Generally, channel response during etalon scans becomes noisier at higher channels. The circle-to-point converter and etalon were manufactured independent of one another resulting in imperfect alignment, which decreases at higher channels, or larger fringe pattern radii (Yorks *et al*. 2014). This is addressed by normalizing the peak response of each channel to the channel that exhibit the greatest peak transmission. However, this does not completely remedy the noisier response observed at higher channels.

Since ACATS last deployment significant improvements have been made to both its hardware and software under the NASA GSFC Internal Research and Development (IRAD) program. As mentioned in the previous section, an etalon scan is ideally performed when the incident signal on the detectors is uniform. Since the intended Rayleigh signal at high altitudes proved unviable it was theorized that placing a scattering medium inside the

ACATS telescope housing in the path of the outgoing laser beam could be used for etalon calibration. This resolves both the weak signal and scene variability issue.

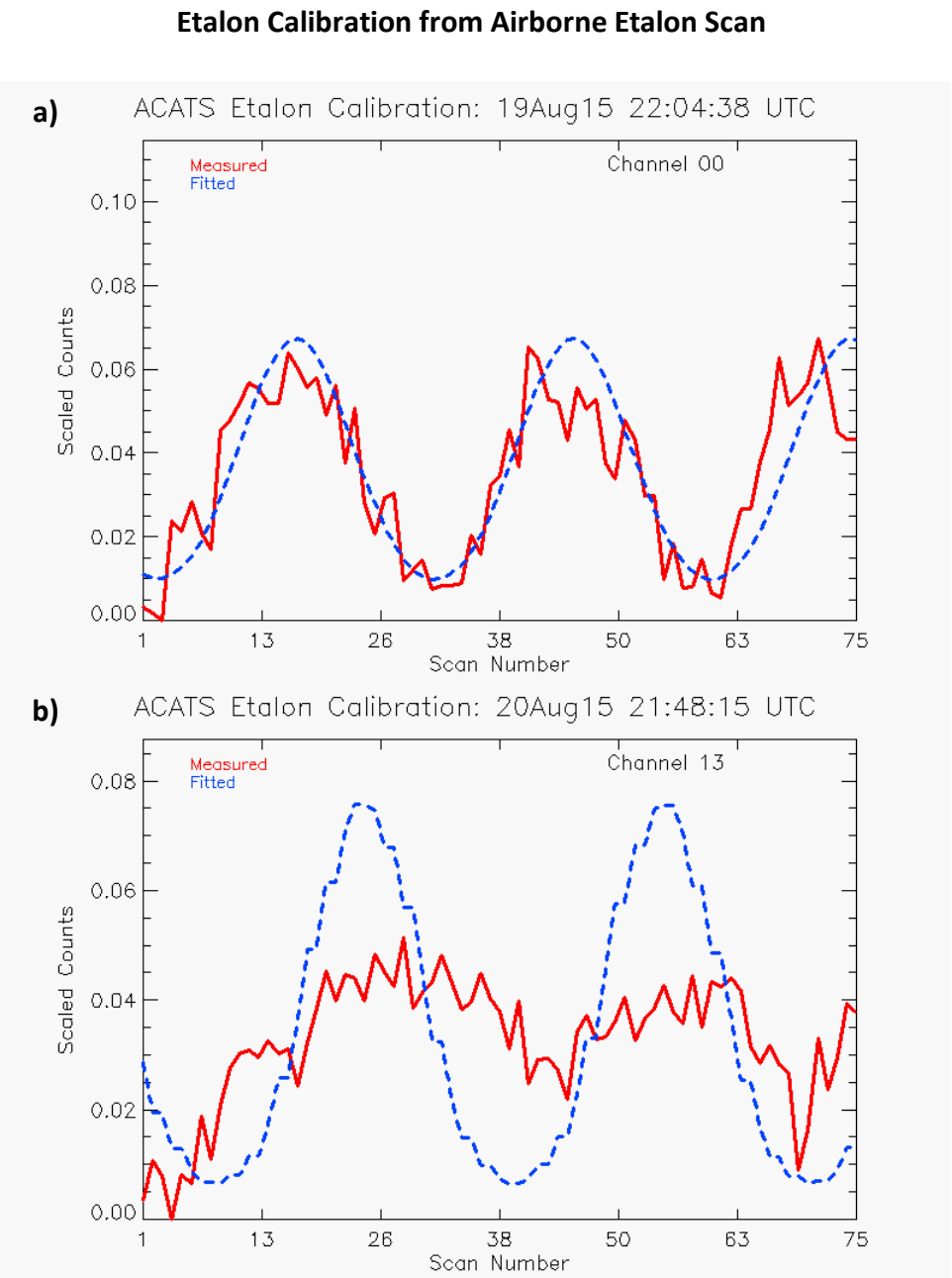

Figure 2.6 (a) The calibration fit for ACATS channel 1 from an airborne etalon scan performed on August 19th, 2015 with red curve representing the spectral response, and blue curve the fitted transmission function. (**b)** The calibration fit for channel 13 from a scan performed during a flight the next day on August 20th.

Applying this theory I tested and developed a new calibration configuration, which was integrated into the ACATS receiver subsystem. After testing various materials I determined that placing Delrin plastic in the path of the outgoing laser pulse within the ACATS telescope yielded the desired spectral response for an etalon scan. White Delrin plastic is highly reflective, and is thermally stable able to withstand the ACATS 0.25-Watt high power laser on the order of hours. Etalon scans take on the order of 10 minutes complete, however, the Delrin was tested with constant incident laser light for a maximum of eight hours with no signal or material degradation. Since the Delrin plastic scatters a high percentage of ACATS emitted photons into the first range bin it was realized that a filter was needed over the receiver fiberoptic to prevent detector saturation. High volume photon returns incident on the ACATS detectors puts the array into a non-linear counting region, which causes a high photon count saturating the detectors effectively smoothing out the desired peak spectral signal. In addition to the Delrin scattering medium neutral density Schott glass filters equivalent to an optical depth of 2.3 were placed over the receiver fiber in the telescope housing. Once the optimal configuration specifications were determined the Delrin and filter were integrated on electric piston motors used to put all components in etalon calibration configuration by the ACATS software when desired. Figure 2.7 shows the inside of the ACATS telescope with the newly integrated Delrin and filter in their etalon scan configuration. Green light can be seen incident on the Delrin, which is placed in front of a mirror that would otherwise direct the beam out of the telescope for atmospheric retrievals. Photons scattered by the Delrin inside the telescope

housing become incident on a focusing mirror toward the top of the housing (not pictured), and are directed into the fiberoptic cable covered by the filter.

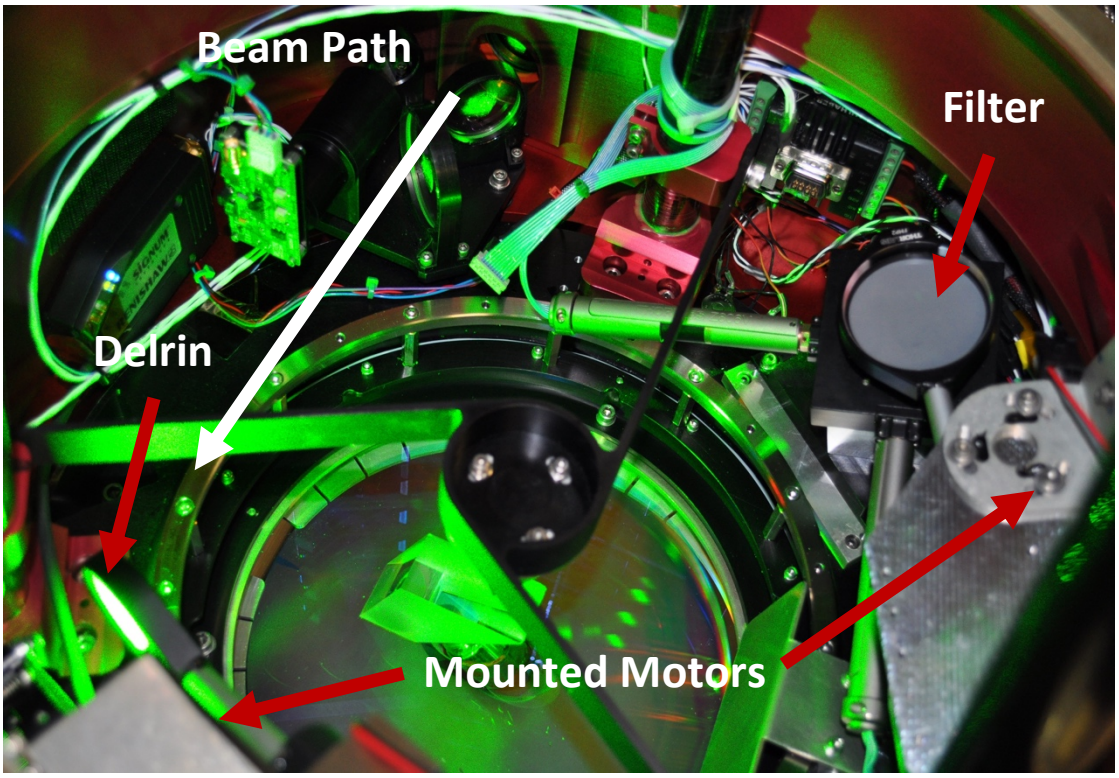

Figure 2.7 Looking down inside the ACATS telescope housing. Transmitted laser light enters the telescope from the top left of the image, and then scattered within by Delrin moved in front of the mirror by a piston motor. Filters are also moved over the fiber head by a piston motor to prevent detector saturation during calibration.

Using this new etalon calibration configuration and technique etalon scans were improved to yield consistent and reliable responses in each channel yielding accurate fits of the etalon transmission function. Figure 2.8 shows an example of the desired etalon calibration fit from an etalon scan. Fig. 2.8a depicts the response in ACATS first channel (red curve) from an etalon scan performed while taking zenith pointing data from NASA GSFC on March 22, 2018. The blue dashed curve shows the best fit etalon transmission function yielding a defect parameter of 13 nm. Fig. 2.8b shows the measured response in Channel 15 from the same etalon scan, which yielded a defect parameter of 51 nm.

Compared to Fig. 2.6 the etalon scan using the new configuration exhibited channel response with a higher SNR at both the lower and higher ACATS detector channels.

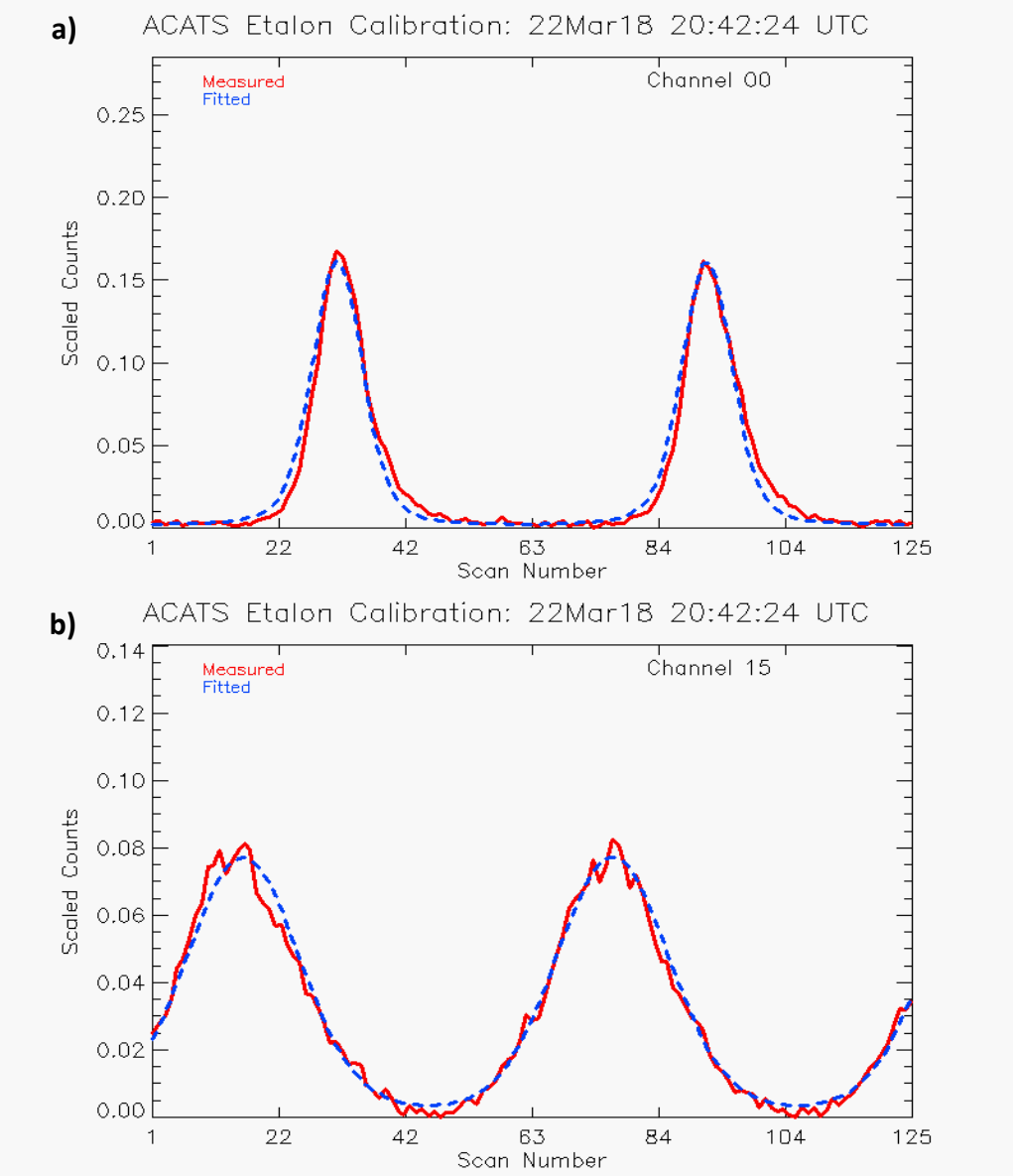

Figure 2.8 Etalon scan performed using new technique and hardware with new scan parameters of 125 steps at 4 nm intervals. **(a)** Shows the response in channel 1 response yielding a defect value of 13 nm, and **(b)** shows the response in channel 15 with a defect value of 51 nm.

Etalon scans can either be fully autonomous by configuring a startup file in the instrument software, or manually using the NASA ER-2 INMARSAT communications to

control ACATS from a laptop on the ground during flight. Three factors must be determined before performing an etalon scan: number of etalon actuator steps per scan, size of the steps (nm), and signal integration time per step. For fully autonomous operations during flight the periodicity of etalon scans must also by determined. These four factors are all hard coded into a startup configuration file that ACATS initiates when turning on, however, can be manually controlled mid-flight from the ground if needed. The number and size of steps determines how many orders of the free spectral range (number of peaks) are sampled by each channel. The integration time is how long photon counts are accumulated at each step. More integration time yields a greater signal for the calibration characterization, this however results in a longer etalon scan yielding less time collecting science data during flights. Additionally, moving the etalon actuators before integrating photon counts at each step also increases the time per scan. As NASA airborne science flight hours have a high cost point it is important to optimize etalon scans not only for accurate defect values, but also temporally. Previous ACATS field campaigns conducted etalon scans with 75 steps at 10 nm intervals, with an integration time of 5 seconds. These scans took approximately 8 minutes to complete, and sampled nearly 3 orders of the FSR. This is observed by the three peaks in the blue fit curve of Fig. 2.6a. Originally, etalon scans with the new configuration were tested incorporating these previous etalon scan specs from airborne science flights. Figure 2.9 shows this response in Channel 1 and Channel 15 from a scan on February 1, 2016. Though the signal in the channel response appears to be nominal with an accurate fit, having an etalon scan step of 10 nm yields a broader fit in the lower channels compared to the response in Fig. 2.8. The Channel 1 defect parameter in Fig. 2.9a was over a factor of two greater at 28 nm compared to the defect

parameter in Fig. 2.8a of 13 nm. This difference in channel response has a greater effect at lower channels compared to higher channels. The defect parameter for Channel 15 in Fig. 2.9b was 52 nm. Very similar to the 51 nm retrieved for Channel 15 in Fig. 2.8b. To retrieve more accurate defect values in the ACATS lower channels etalon scans were tested

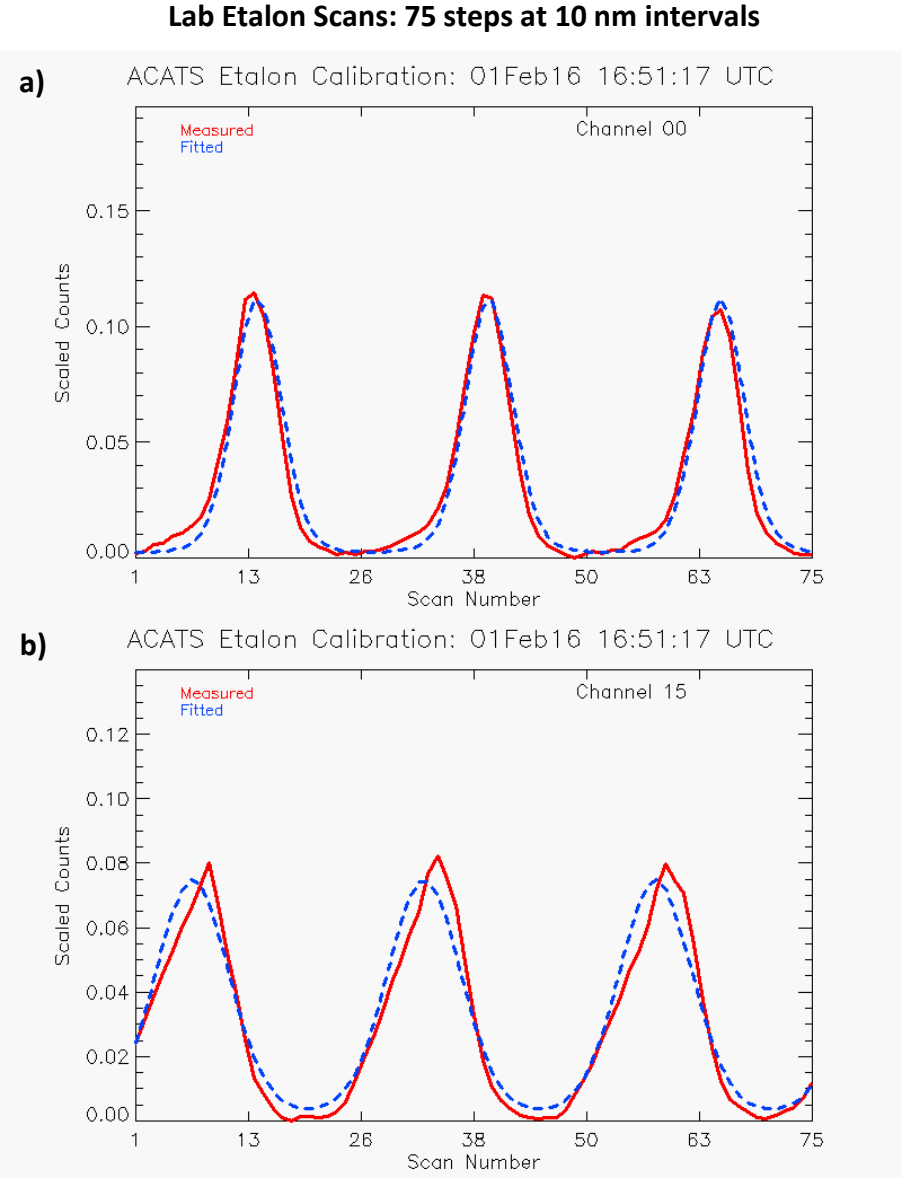

Figure 2.9 Etalon scan performed using new technique and hardware with original flight scan parameters of 75 steps at 10 nm intervals. **(a)** Shows the response in channel 1 response yielding a defect value of 28 nm, and **(b)** shows the response in channel 15 with a defect value of 52 nm.

and optimized to be conducted with 125 steps at 4 nm intervals, and an integration time of 5 seconds. Though the orders of the FSR sampled were effectively reduced from approximately three to two this still proved adequate to yield a reliable fit and defect retrieval. However, increasing the step count from 75 to 125 increased the etalon scan time by approximately 50%.

The new etalon calibration was proven in the lab to have much higher precision and lower uncertainty compared to etalon scans performed during flight operations. Figure 2.10 shows the defect statistics for the most recent ACATS science flights (Fig. 2.10a), and for a series of lab tests (Fig. 2.10b). The black curves indicate the calculated channel defect values for each etalon scan, the red curve is the mean bounded by the standard deviation in light blue, and the blue curve is the relative uncertainty given by the ratio of the mean to the standard deviation. The defect values recovered from science flights include seven of the most recent etalon scans from ACATS two previous deployments. These include a July 2014 campaign out of Fairbanks, AK and an August 2015 campaign out of Palmdale, CA. The defect values recovered from the sciences flights are inconsistent and exhibit high variability with a mean relative uncertainty of 26.6% and a mean standard deviation of 30.5 nm. To contrast with the airborne retrievals seven etalon scans were performed in the lab using the new configuration over seven separate days. This was done to mimic the complete cool down period ACATS would have over approximately 24 hours between consecutive flight days. The set of etalon scans using the new configuration exhibited low variability

across all ACATS channels with a mean relative uncertainty of 11.2%, and a mean standard deviation of 3.70 nm.

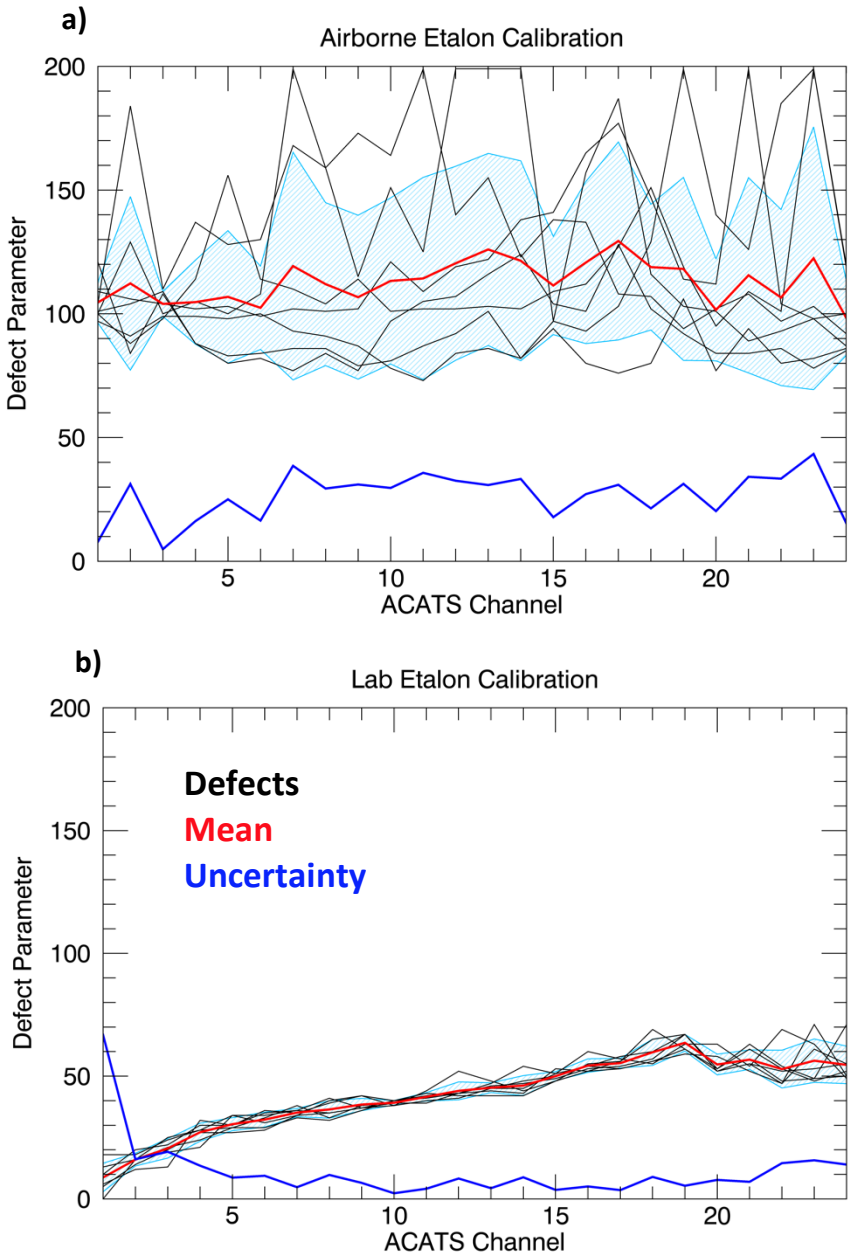

Figure 2.10 (a) Defect values from seven most recent ACATS science flights and associated statistics. Blue curves are for each individual etalon scan. The read curve is the mean defect for each channel bound by the standard deviation in the hatched light blue. The blue curve is the uncertainty in the defect for that channel. **(b)** Depicts the same statistics for seven lab etalon calibrations performed on separate days.

2.5 Cirrus HSRL Retrievals

As mentioned in section 2.3 accurate defect values are a key component in retrieving ACATS attenuated Rayleigh backscatter (ARB; ω), attenuated particulate backscatter (APB; α), and line-of-site wind velocity (U_{LOS}). Improved etalon calibration results in improved retrieval of ACATS HSRL products, with the successful separation of the molecular and particulate signals. Ideally, accurate retrievals of ARB and APB yield direct calculations of lidar ratio in each range bin. This is beneficial compared to the transmission-loss method, discussed in Chapter 1, which provides a constrained lidar ratio assumed constant through a layer that can only be calculated when conditions are favorable. Additionally, ACATS HSRL products can be retrieved at each range bin through all particulate layers in the lidar signal profile independent of layer boundary conditions.

Figure 2.11 shows curtain images from an ACATS science flight on August 19th, 2015 and zenith pointing lab data taken on April 13th, 2018. Figs. 2.11a – b depict the retrieved APB and ARB for the airborne data, respectively, and Figs. 2.11c – d show the retrieved APB and ARB for the lab data, respectively. Utilizing the defect values retrieved from the etalon scan performed mid-flight on August 19th, the ACATS three-parameter inversion was unable to successfully separate the signal into its Rayleigh and particulate components. The August 19th flight path was over the ocean for approximately the first half, and then over the Sierra Neva Mountains the second half. There is a thin cirrus layer at approximately 10 km and an aerosol layer 2 km above the ground in the second half of

the Fig. 2.11 a – b over the Sierras. The ground return is indicated by the white shaded area at the base of both 2.11 a – b. Though the Rayleigh signal was partly removed from the

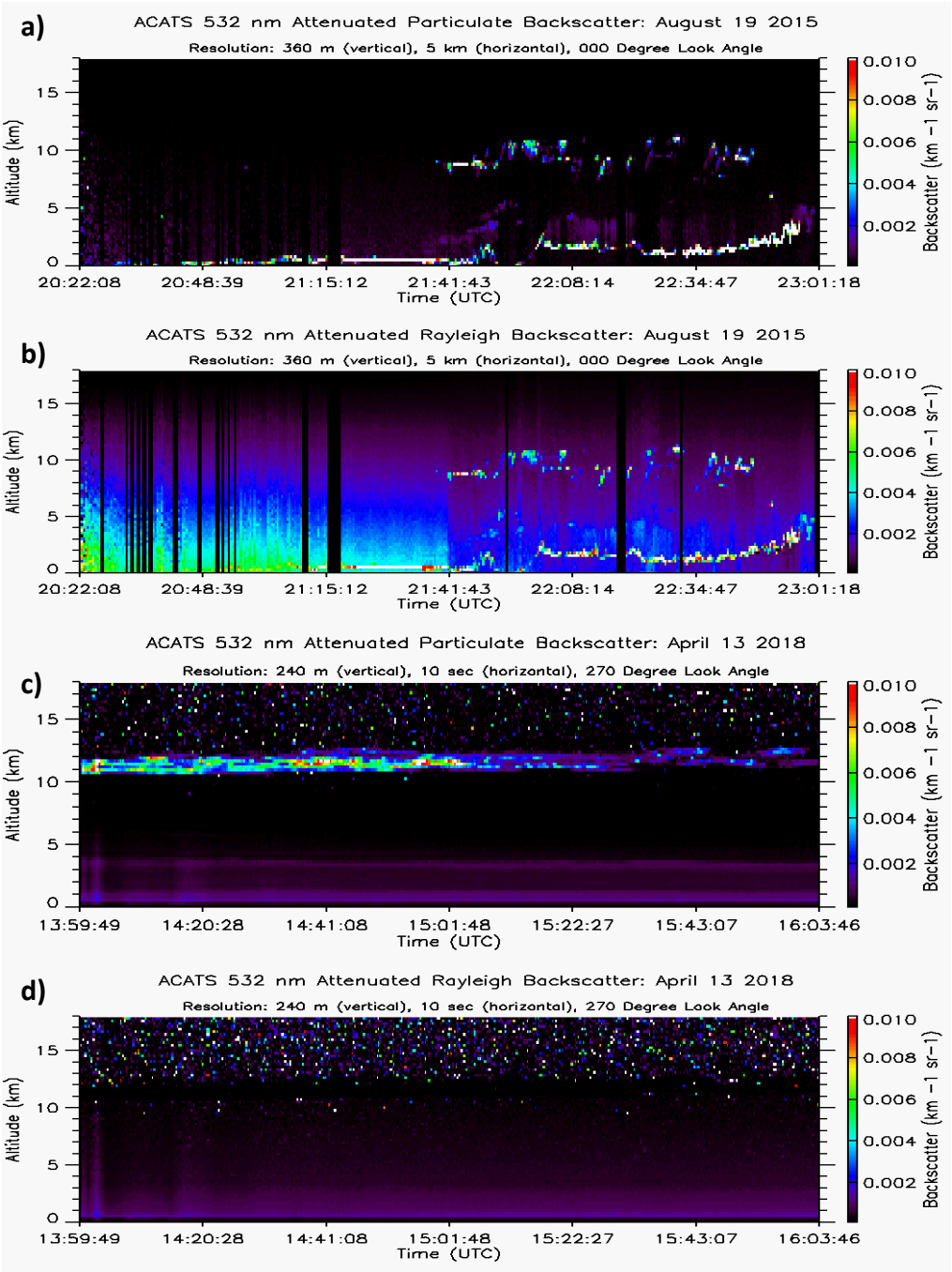

Figure 2.11 Separation of attenuated Rayleigh backscatter **(a)** and attenuated particulate backscatter **(b)** signals from science flight on August 19th, 2015. Improved separation of signal components in zenith pointing data take from NASA GSFC on April 13th, 2018. Attenuated Rayleigh backscatter **(c)** and attenuated particulate backscatter **(d)**.

particulate signal, indicated by the absence of the purple and blue values above the ground in 2.11a, the cirrus and aerosol layers are entirely present in both images. The April 13th case of zenith pointing lab data has a cirrus layer at approximately 11 km, and a thin aerosol layer at 3.5 km both spanning the whole timeframe in Fig. 2.11c. Compared to the airborne case, the etalon scan performed in the lab yielded defect values that qualitatively separated the ARB and APB into individual data sets. The Rayleigh signal is stronger in Fig. 2.11d compared to 2.11c indicated by the uniform purple gradient above the ground, which has a thin black line through it representing the removal of the aerosol layer present in 2.11c. Additionally, the ARB signal retrieved in Fig. 2.11d matches the modeled Rayleigh signal. This is shown in the profile (Fig. 2.12) of the April 13th scene from 15:10 UTC with the green and dashed curves representing the ARB and modeled Rayleigh signal, respectively. The modeled Rayleigh signal is calculated from radiosonde data retrieved from the Sterling, VA weather service office 00 UTC balloon launch. Note that this agreement is limited to approximately the region between 4 – 11 km. At 11 km the ARB signal enters the cloud base, and becomes greatly attenuated. The 4 km mark indicates the top of the aerosol layer observed in Fig. 2.11c. Below 4 km the signal is affected by errors in the overlap function, which is not optimized from ground operations. It can also be seen that the cirrus layer present in the APB image (2.11c) was successfully removed from the ARB image (2.11d). In all zenith pointing data retrieved from NASA GSFC the Rayleigh and particulate signals were successfully separated using defect values calculated from the new etalon calibration procedure.

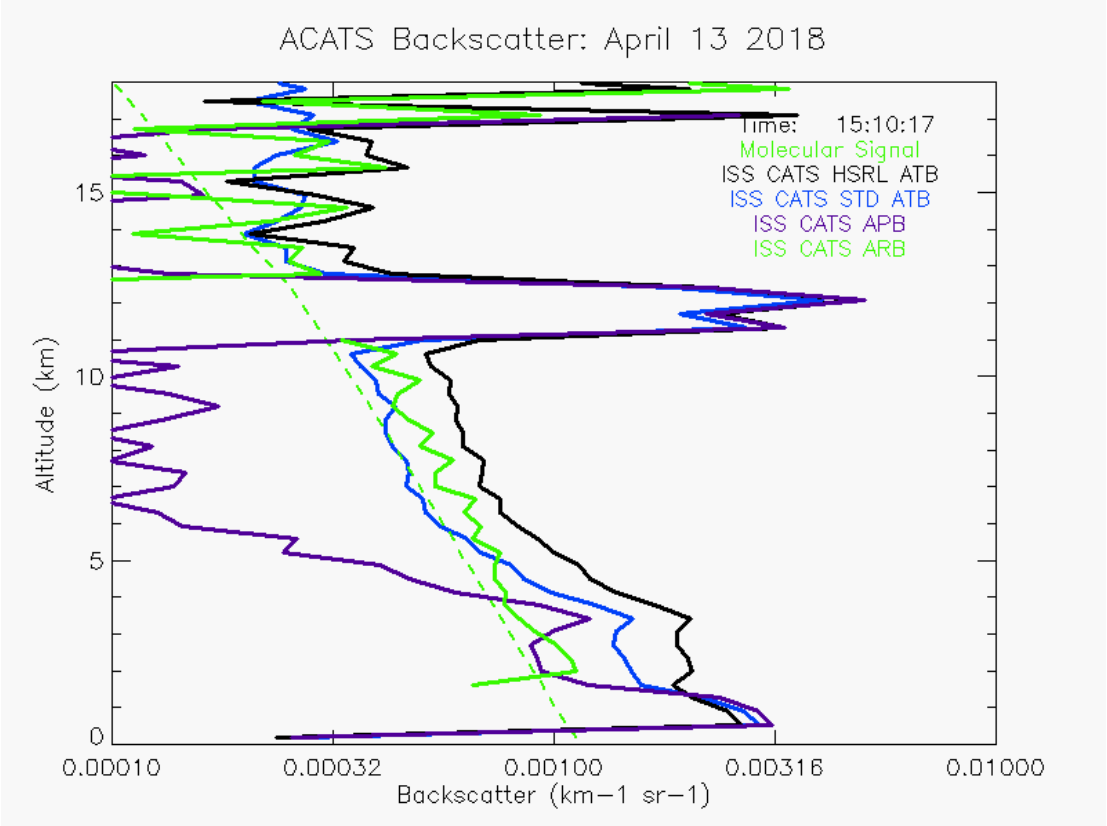

Figure 2.12 Profile from the April 13th cirrus scene at 15:10 UTC. The HSRL ATB, Standard ATB, ARB, APB, and modeled Rayleigh signal are represented by the black, blue, green, violet, and dashed curves, respectively.

Upon processing the data further for higher level optical properties, quantitatively the retrieved signals proved to have inadequate SNR. To compute HSRL optical properties from the separated ACATS signal, ARB and APB are first used to calculate the two-way particulate transmission (Eq. 2.7), and then particulate backscatter coefficient (Eq. 2.8). Once these quantites are calculated the optical depth (Eq. 2.9), particule extinction coefficient (Eq. 2.10), and particle lidar ratio (Eq. 1.4) can then be retrieved. Figure 2.13 shows the particulate extinction coefficient (Fig. 2.13a) and particle lidar ratios (Fig. 2.13b) retrieved from the April 13th case. Examining the cirrus layer extinction retrievals they are unrealistically high, and inconsistant with the cloud structure observed in Fig. 2.11c. The lidar ratios exhibit a boundary issue with annonamously high values at the cirrus layer top

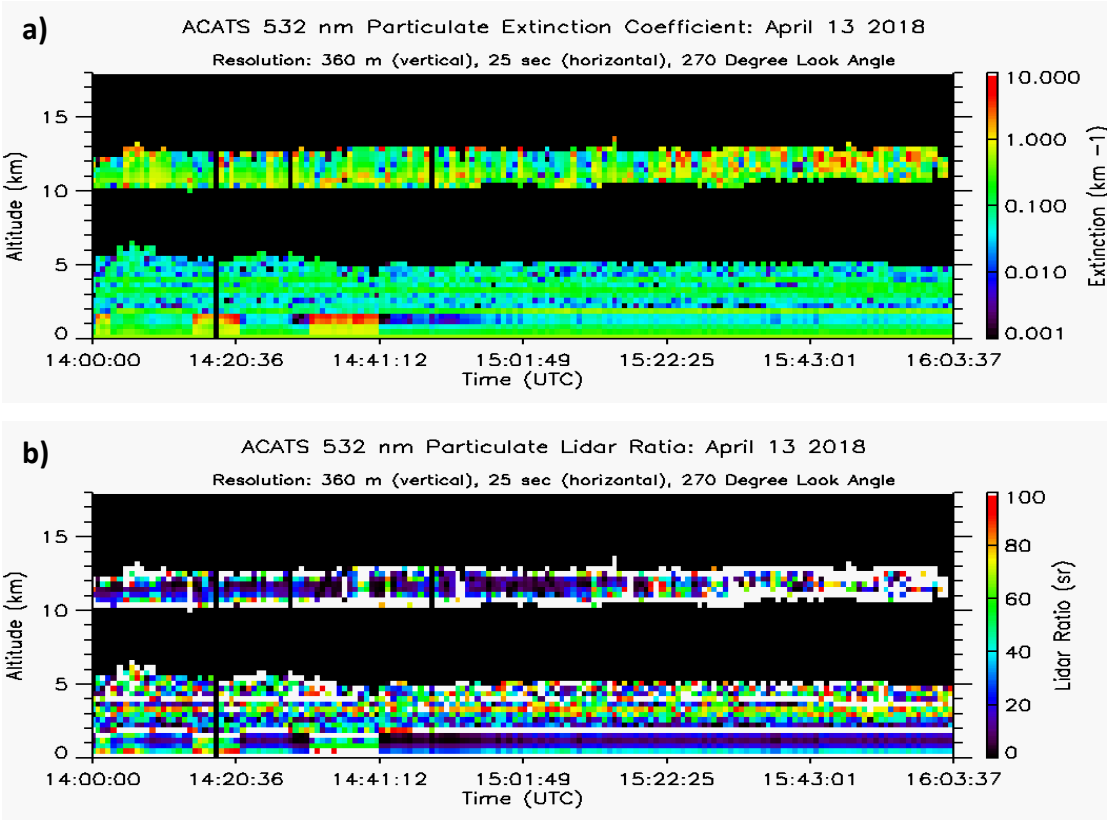

Figure 2.13 (a) ACATS retrieved optical properties for April 13th case. **(a)** Particle extinction coefficient and **(b)** particle lidar ratio

and base, and too low of values within the cloud layer. Figure 2.14 show the histogram of the retrieved lidar ratios within the cirrus layer from Fig. 2.13b. It can be seen that the peak favors the lowest retrieved lidar ratios less than 10 sr due to the low values within the layer, and then has a tail skewed towards higher values due to the boundary error. This is explained by looking at the sample profiles in Fig. 2.12. Examining the green and violet curves at the cloud boundaries, approximately 11 and 13 km, it can be seen that the ARB (green curve) is larger than the APB (violet curve) in these boundary bins. Applying this to the above equations, large ω with low α values results in large $T_p^2(r)$ (Eq. 2.7), and consequently a low β_P (Eq. 2.8). Additionally, since the ARB decreases durastically within the layer from the boundary bin this results in a relatively high $\partial\tau_P(r)$ from Eq. 2.9, and

therefore, a large $\sigma_P(r)$ (Eq. 2.10). Applying this to the lidar ratio of extinction-to-backscatter (Eq. 1.4) a large extinction with low backscatter will result in an annonymously high lidar ratio, as observed at the cirrus layer boundaries in Fig. 2.13b. Similarly, within the cirrus layer the low ω values, indicated by the absence of the green curve in Fig. 2.12, results in annonamously low lidar ratio values. Nominally, the histgram in Fig. 2.14 would have a peak in the range between 20 – 30 sr (Yorks *et al.* 2011).

$$T_p^2(r) = \frac{\omega(\pi, r)}{\beta_M(\pi, r)T_M^2(r)} \qquad \text{Eq. 2.7}$$

$$\beta_P(\pi, r) = \frac{\alpha(\pi, r)}{T_M^2(r)T_p^2(r)} \qquad \text{Eq. 2.8}$$

$$\tau_P(r) = -\frac{1}{2}\ln\left[T_p^2(r)\right] \qquad \text{Eq. 2.9}$$

$$\sigma_P(r) = \frac{\partial \tau_P(r)}{\partial r} \qquad \text{Eq. 2.10}$$

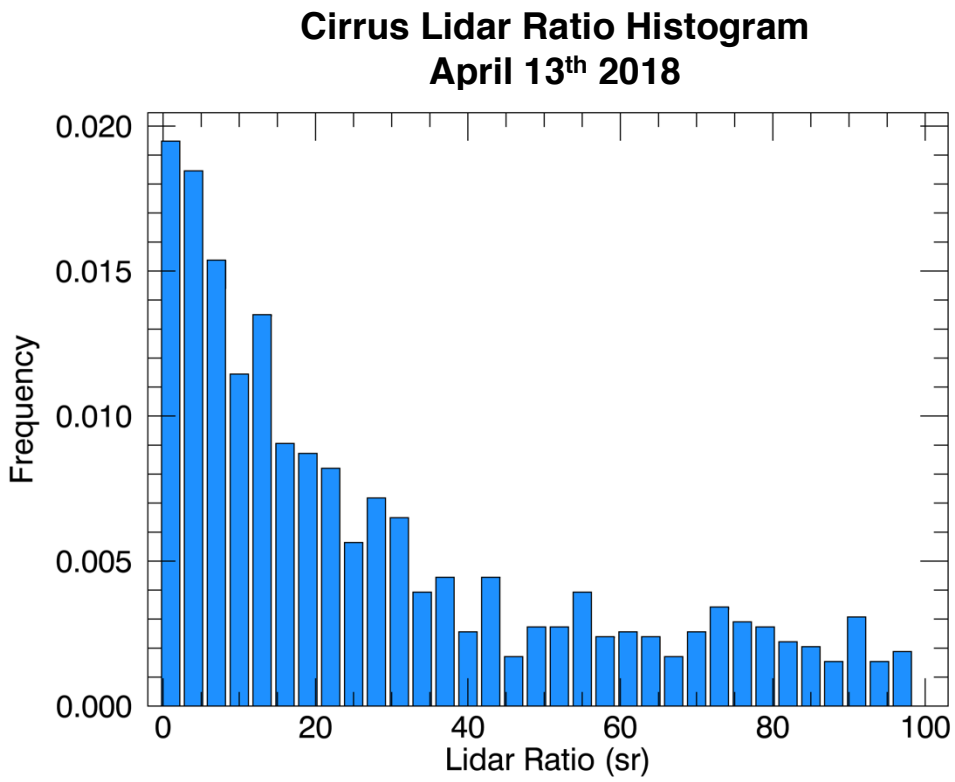

Figure 2.14 Histogram of retrieved cirrus lidar ratios from April 13th case with a bin size of 3 sr.

These patterns were often exhibited in cirrus HSRL optcal properties retrieved from ACATS zenith pointing data. Though calibration improvement was highly successful at improving the accuracy of the defect parameter, it was eventually concluded the ARB signal could not be estimated to the accuracy required to perform HSRL retrievals due to low Rayleigh signal. It is believed this is due to the 10 cm spacing of the ACATS etalon, which was designed for high resolution sampling of the Doppler shifted particulate signal. The etalon essentially filters out a large percentage of the Rayleigh signal, hindering reliable retrievals of ARB (ω) that are crucial to the first step (Eq. 2.7) of computing optical properties. A smaller etalon gap would have proved more reliable at sampling the Rayleigh broadend signal. This is shown in Figure 2.15 comparing the ACATS 10 cm gap etalon transmission function with that of a 3.0 cm etalon, like the one implemented in the CATS

instrument design, keeping all other variables constant. The broader blue curve indicates the greater transmission of the Rayleigh signal through the 3.0 cm etalon to the receiver.

For ground-based zenith pointing operations ACATS HSRL calculated optical properites are limited in the degree of accuracy to which they can be consistently retrieved. It was originally theorized that cirrus HSRL retrieved properties, when incorporated into a radiation model, would yield a greater constraint on modeled cirrus radiative effects compared to properties retrieved using the standard backscatter lidar technique. Yorks (2014) showed ACATS HSRL extinction retrievals exhibited uncertainties that were 25-50% lower than coincident CPL exctinction retrievals in the 2012 WAVE campaign out of

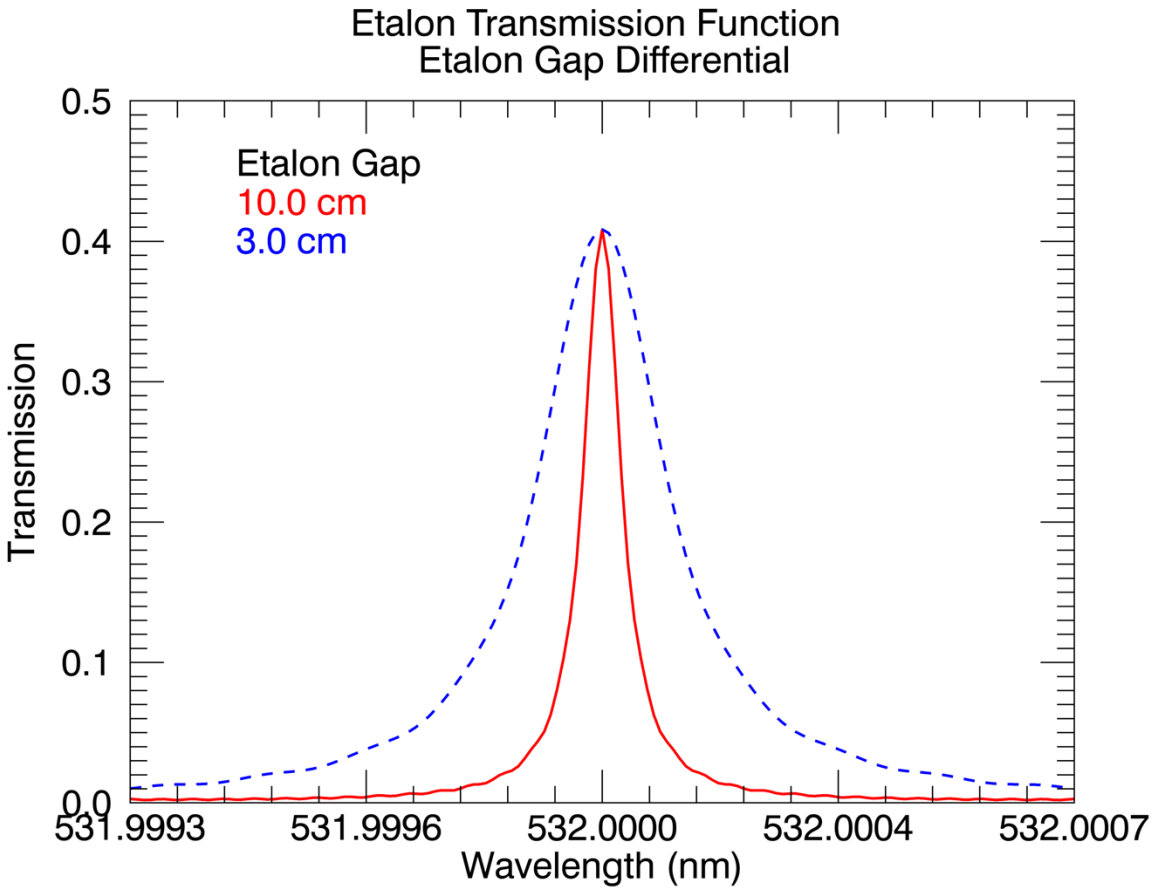

Figure 2.15 Etalon transmission function for an Etalon with a 10 cm gap (red curve) contrasted with an etalon having a 3.0 cm gap (blue curve)

Wallops Island, VA. After rigerous testing it was concluded ACATS lab retrievals would not be a viable option for this study due to the complications discussed prior. However, there is confidence the new etalon calibration technique will yield accurate defect values in potential future ACATS science campaigns from the ER-2 platfom. In contrast to ground-based data, future airborne ACATS operations will have the advantage of a reduced range-to-target and signal attenutation yieldling potentially more relaible ARB retrievals within cirrus layers.

2.6 Cirrus Vertical Wind Retrievals

After concluding ACATS Rayleigh signal was inconsistently reliable, focus was shifted from HSRL optical property retrievals to ACATS Doppler wind capabilities. As mentioned earlier in this chapter, a weak Rayleigh signal in the near field return below the high-altitude ER-2 hindered reliable etalon calibration and reference spectrum retrievals during flight operations. A crucial component of Doppler wind retrievals is defining the reference spectrum of the outgoing wavelength, which is subtracted from backscatter retrieved spectrum of each bin. The retrieved LOS wind is equivalent to the peak channel of the spectrum, and the corresponding dynamic wind speed per channel shift. As mentioned in section 2.2 the ACATS software attempts to keep the signal peaked in Channel 4, and ACATS etalon has a wind speed resolution of approximately 20 ms^{-1} per channel. For example, if the doppler shifted signal for a given retrieval was fit to Channel 4.1 this would correspond to a retrieved LOS wind of 82 ms^{-1}, and the reference spectrum peaked in Channel 4.0 would correspond to 80 ms^{-1} resulting in a calculated LOS wind of 2 ms^{-1}. Similar to etalon calibration, original ACATS operations were intended to retrieve the reference spectrum of each profile from the scattered Rayleigh signal in the range bins

immediately below the ER-2. However, weak scattering in the thin atmosphere at operational altitude of 20 km proved this to be an unviable option.

An additional benefit of the newly integrated hardware into the ACATS telescope is it allows for reference spectrum retrievals. The configuration required for the new etalon scan technique is identical to that for the retrieval of reference spectra. While etalon scans take on the order of tens of minutes, and reference spectrum can be retrieved within seconds. The ACATS software package was updated to include configurations defining the time interval for reference spectrum retrievals, and signal integration time. However, while etalon scans take much longer they are only required to be completed once or twice per flight. In contrast, reference spectra must be sampled more frequently to account for drift in the ACATS laser transmitted center wavelength. Fig. 2.4a shows the etalon control software operating nominally, however, small variation on the order of 1.0 channels are observed, which can cause retrieved wind errors up to 20 ms^{-1}.

Due to the zenith pointing view angle of ACATS lab testing, LOS wind testing was limited to retrievals of the vertical wind component within cirrus layers. Outside of active convective cores the vertical velocity within cirrus clouds is on the order of centimeters per second (Gultepe *et al.* 1990), which is below ACATS precision. Therefore, validation of ACATS zenith LOS winds was obtaining retrievals on the order of +/- 1.0 ms^{-1}. Initial testing conducted reference spectrum retrievals at six minute intervals with a one minute signal integration time. Figure 2.16 shows an ATB curtain image from January 16th, 2018 of the cirrus layer observed for this initial testing. Vertical black lines indicate times where the Delrin configuration was placed in front of the outgoing beam to retrieve the laser reference spectra. The retrieved reference spectra where then processed using the three-parameter fit algorithm (McGill *et al.* 1997a) to calculate associated wind estimates. These reference winds were then subtracted from all retrievals in subsequent profiles till the following reference spectrum integration. Figure 2.17 shows two nominal wind profiles from the January 16th case indicated by the vertical red lines in Fig. 2.16. Both profiles in

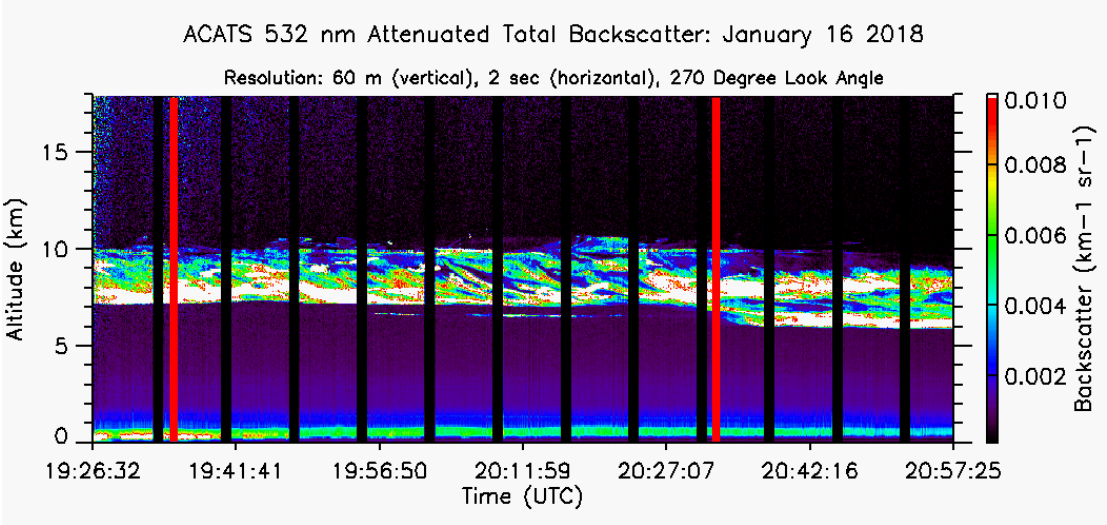

Figure 2.16 ATB curtain image of cirrus layer for first testing of ACATS wind retrievals calculating reference bins from new integrated hardware.

Fig. 2.17 exhibit the expected ACATS vertical wind profile in a cirrus layer, and correspond to times soon after a reference spectrum was retrieved. However, the ACATS laser drift during the six minutes between references caused increasing wind errors until after the following reference spectrum retrieval. Figure 2.18 shows a histogram of all retrieved LOS winds in the January 16th cirrus layer. This clearly shows wind estimates greater than the expected vertical velocities. The blue shaded bars represent winds retrieved using defect values from the etalon scan on that day, and the red bars are winds retrieved using those defects increased by 40% (the mean defect uncertainty shown in Fig. 2.10a using original calibration method). The effect is not clear in the histograms shown, however the accurate defect values yielded a mean wind of -4.82 ±15.25 ms^{-1}, and the increased defects a mean wind of -10.1 ±15.72 ms^{-1}.

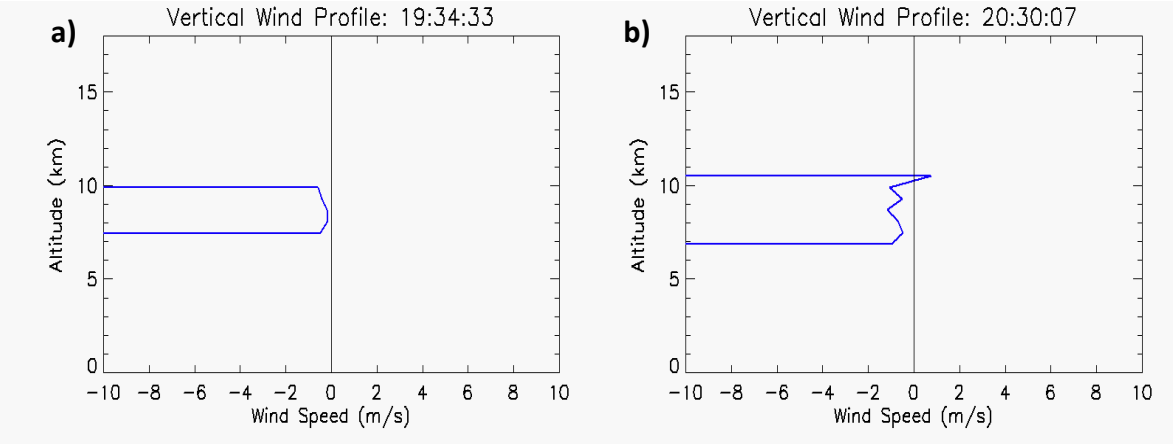

Figure 2.17 Vertical LOS wind profiles from January 16th cirrus layer indicated by red lines on Fig. 2.14. **(a)** Profile at 19:34:33 UTC and **(b)** profile at 20:30:07 UTC.

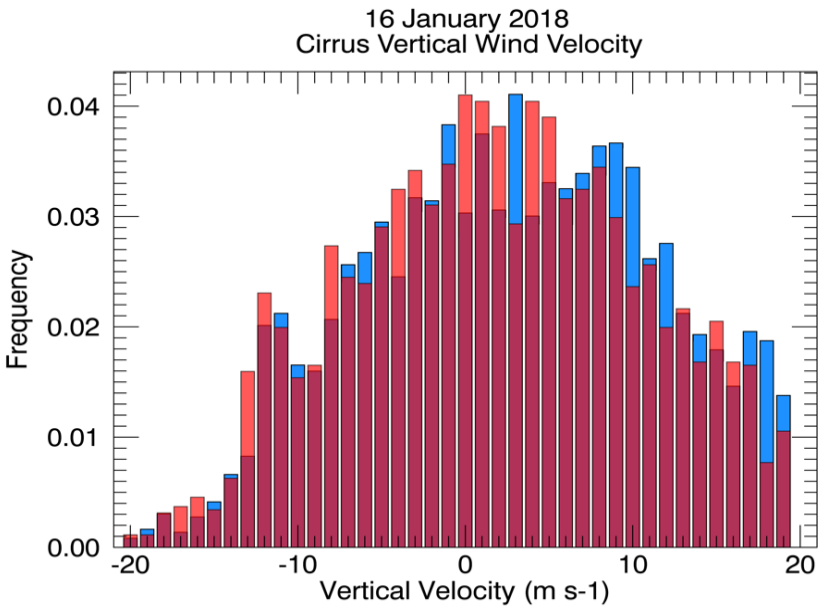

Figure 2.18 Histograms of ACATS retrieved vertical line-of-site wind velocities in a cirrus layer passing of GSFC on January 16th, 2018. Blue shaded bars are those retrieved using accurate defect values, and red shaded those retrieved using defect values in each channel increased by 40%

Though ACATS laser is injection seeded for laser stability testing proved that the high resolution etalon in the ACATS system was sensitive to small drifts in the laser spectrum, which indicated reference spectra had to be retrieved at more frequent intervals. Figure 2.19 shows the histogram for retrieved vertical winds in a thin cirrus layer that passed over GSFC on March 22nd, 2018. In this case reference spectrums were taken every 45 seconds with a signal integration time of ten seconds yielding over 150 reference spectra over a two hour data collection period. Additionally, the more frequent reference spectra retrieval allowed for interpolation of the reference wind array to match the same number of profiles as the whole dataset yielding a unique reference wind value to be subtracted from each profile. This is in contrast to the January 16th case, which assumed a constant reference spectrum, and associated reference wind value, between reference spectrum integration periods. The Fig. 2.19 histogram shows a clear improvement on vertical wind

retrievals compared to the January 16th case with a clear peak closer to the expected zero ms^{-1}. The effect of accurate defect values is also clearer in this case with the displacement of the histogram peak associated with the increased defect vales towards greater magnitude winds. The mean vertical wind in the March 22nd case was -2.26 ±6.14 ms^{-1}, and -4.15 ±12.4 ms^{-1} using the increased defect values. As both mean wind values are biased towards negative velocities it is possible ACATS is detecting falling crystals, however, speeds on the order of -2.0 ms^{-1} are greater than expected (Gultepe *et al.* 1990).

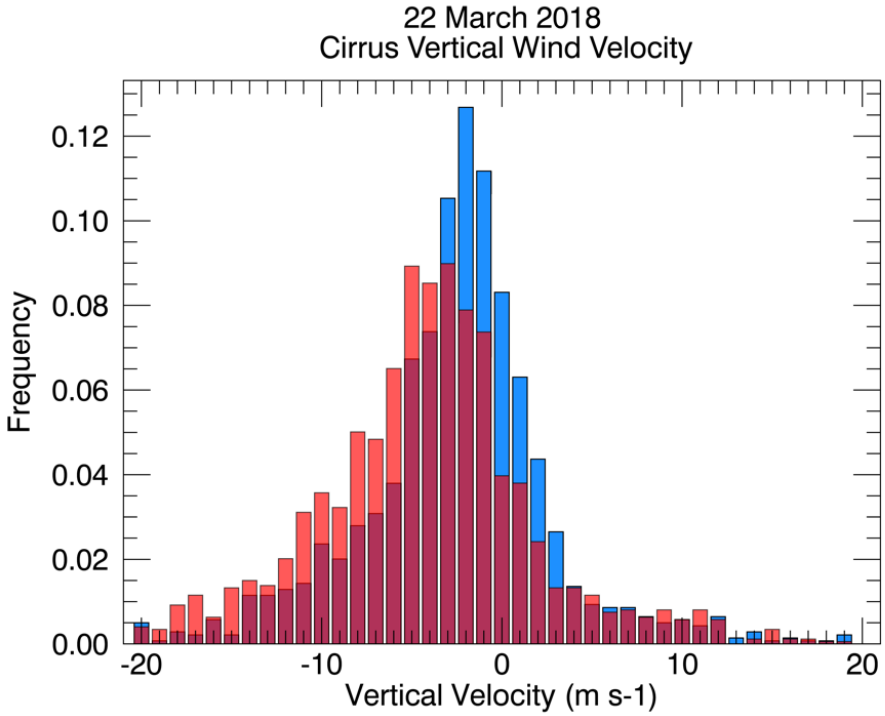

Figure 2.19 Histograms of ACATS retrieved vertical line-of-site wind velocities in a cirrus layer passing of GSFC on March 22nd, 2018. Blue shaded bars are those retrieved using accurate defect values, and red shaded those retrieved using defect values in each channel increased by 40%

The updated ACATS system with the new calibration configuration integrated into the receiver sub-system was successful at providing consistent and reliable etalon calibration. This is a crucial first step in retrieving ACATS HSRL and Doppler wind retrievals. The new calibration technique yielded etalon defect values leading to the

reliable separation of the Rayleigh and particulate signals. However, HSRL optical properties and LOS Doppler wind retrievals exhibited large uncertainties within cirrus layers during ground based zenith pointing operations. Though the Rayleigh signal was consistently distinguished from the particulate signal in cirrus clouds during testing, retrieval of the ARB was not to the accuracy required for reliable science quality retrievals of HSRL optical properties. Using the MC technique ACATS is also inherently a DWL. Using the improved etalon calibration configuration vertical wind retrievals within cirrus layers were also analyzed. However, it was shown that the ACATS laser stability was not to that required for consistent retrievals of reference spectra. Increasing the temporal resolution of reference spectra improved wind retrievals, however results still had a greater error than required for science quality data indicated by the NASA 2017 decadal survey.

Though HSRL retrieval algorithms may benefit from the absence of a near field aerosol layer, and a reduced range to target during future ER-2 airborne data, this work has elucidated the hardware challenges posed to the ACATS lidar. Without definitive HSRL or Doppler wind retrievals it is likely that prospective ACATS science flights are indefinitely delayed. Additionally, this research has shown the complex synergy between hardware and software components required for successful DWL retrievals, and the challenges posed to future DWL missions; such as the proposed ATHENA-OAWL (Tucker *et al.* 2018) or the recently launched Aeolus by the European Space Agency (ESA; Endemann 2006)

Chapter 3: Global Cirrus Physical and Radiative Properties and their Diurnal & Seasonal Variation (In prep)

Cirrus clouds remain a large source of uncertainty in global climate models due to their physically complex nature, and the array of varying scattering and absorbing properties they exhibit depending on their dynamic formation mechanism, thermodynamic environment, and geographic location. While many airborne based field campaigns have helped elucidate the link between types of cirrus to their associated physical and radiative properties (Yorks, 2014; Bucholtz *et al.* 2010; Ozog *et al.* 2019) global coverage of thin cirrus profile data has primarily been limited to two satellite lidars, CALIPSO and CATS. In this Chapter I investigate all 31 months (April 2015 – October 2017) of CATS mode 7.2 data to retrieve global mean cirrus properties. Utilizing the unique CATS orbit I analyze the diurnal and seasonal variability of cirrus radiative properties. While seasonal studies have been prominent using the robust CALIPSO dataset (Sassen *et al.* 2008; Berry & Mace 2014; Hong *et al.* 2016), diurnal studies are limited to the two local observing times. Here I further analyze the diurnal cycle of cirrus properties by separating the CATS data into four daily subsets (morning, afternoon, evening, and night) for each season, essentially increasing the diurnal representation by a factor of two to four observations.

3.1 CATS Data

The ISS orbits Earth approximately ever 90 minutes. CATS orbital data is separated into a day and a night time granules (HDF files) based on the local solar zenith angle. In total the whole CATS dataset contains 9461 day granules and 9316 night granules, containing millions of cirrus observations. For the entirety of this dataset CATS was operating in its mode 7.2 configuration operating at 532nm and 1064nm, which

additionally includes depolarization capabilities at 1064nm (McGill *et al.* 2015). However, an issue stabilizing the laser frequency with the transmission frequency of the etalon prevented the collection of science quality data in the 532nm. Note that CATS employed a 3 cm gap etalon as a test bed for satellite HSRL retrievals. Due to this all data represented in this study consists of CATS 1064nm retrievals.

CATS processing algorithms produce three distinct science data products including level 1B (L1B), level 2 layer (L2_lay), and level 2 profile (L2_prof). The L1B product consists of the calibrated CATS signal used for layer detection and further processing optical properties for observed atmospheric layers in the L2 products (Yorks *et al.* 2018; Pauly *et al.* 2019). CATS L2 data is produced at a horizontal resolution of 5 km, and a vertical resolution of 0.06 km with the data frame extending from 30 km to -2 km (Yorks *et al.* 2015). L2_lay consists of layer integrated products for all layers observed in each profile consisting of optical depth, ice water path (IWP), integrated depolarization ratio, integrated ATB, and lidar ratio. L2_prof likewise yields vertical profiles of range resolved optical properties within each layer consisting of particle extinction coefficient, particle backscatter coefficient, and ice water content. The above variables are not extensive to all provided in CATS data, just the L2 data used in this study. Additionally, all cirrus observations were quality controlled. I limited cirrus observation only to those that were determined to be ice phase by the CATS processing algorithms with a cloud phase score of 8 or greater (0 – 10), transparent layers (OD < 3.0), and were processed using either a constrained or climatological lidar ratio. Information on CATS processing is provided in the CATS Algorithm Theoretical Basis Document (ATBD; Yorks *et al.* 2015; 2018).

The observations in each day granule were separated into two components corresponding to either local morning or afternoon nadir to the ISS. Likewise each night granule was separated into evening and nighttime observations. Morning observations were defined as those before local solar noon, and afternoon defined as those after local solar noon. Evening observations were those before midnight, and nighttime after midnight. Appendix A contains information on the calculation of local time. Additionally, this diurnal signal was also analyzed in each of the four seasons (JJA, SON, DJF, and MAM) corresponding to boreal summer, autumn, winter, and spring, respectively. This resulted in 16 representative observations of all properties analyzed to better understand cirrus spatial and temporal influence. Due having an odd numbered 31 months of observations there was not an equal number of monthly datasets used to represent each season; stated in table 3.1.

Table 3.1 Cirrus Occurrence Frequency Statistics (±51°)

Season	Mean	Median	Std. Dev.	Min	Max	# Months
JJA	42.7 %	42.1 %	19.7 %	0.9 %	98.0 %	9
SON	43.7 %	42.6 %	19.2 %	0.9 %	99.0 %	8
DJF	43.1 %	44.0 %	20. 2 %	0.9 %	99.6 %	6
MAM	44.6 %	44.0 %	17..3 %	1.3 %	96.9 %	8

3.2 Global Cirrus Statistics

Table 3.1 lists seasonal global cirrus frequency statistics for each season and Fig. 3.1 depicts gridded occurrence frequency of cirrus observations for each time of day in each season on a 3° x 3° latitude/longitude grid between 51° North & South. This was simply calculated as the ratio of total number of cirrus observations in each lat/long grid cell to the overall total observations by CATS. As mentioned in the previous section, only layers which were not fully attenuating were considered for this dataset. Meaning

observations where CATS flew directly over thick convection or cumulonimbus ice are not included.

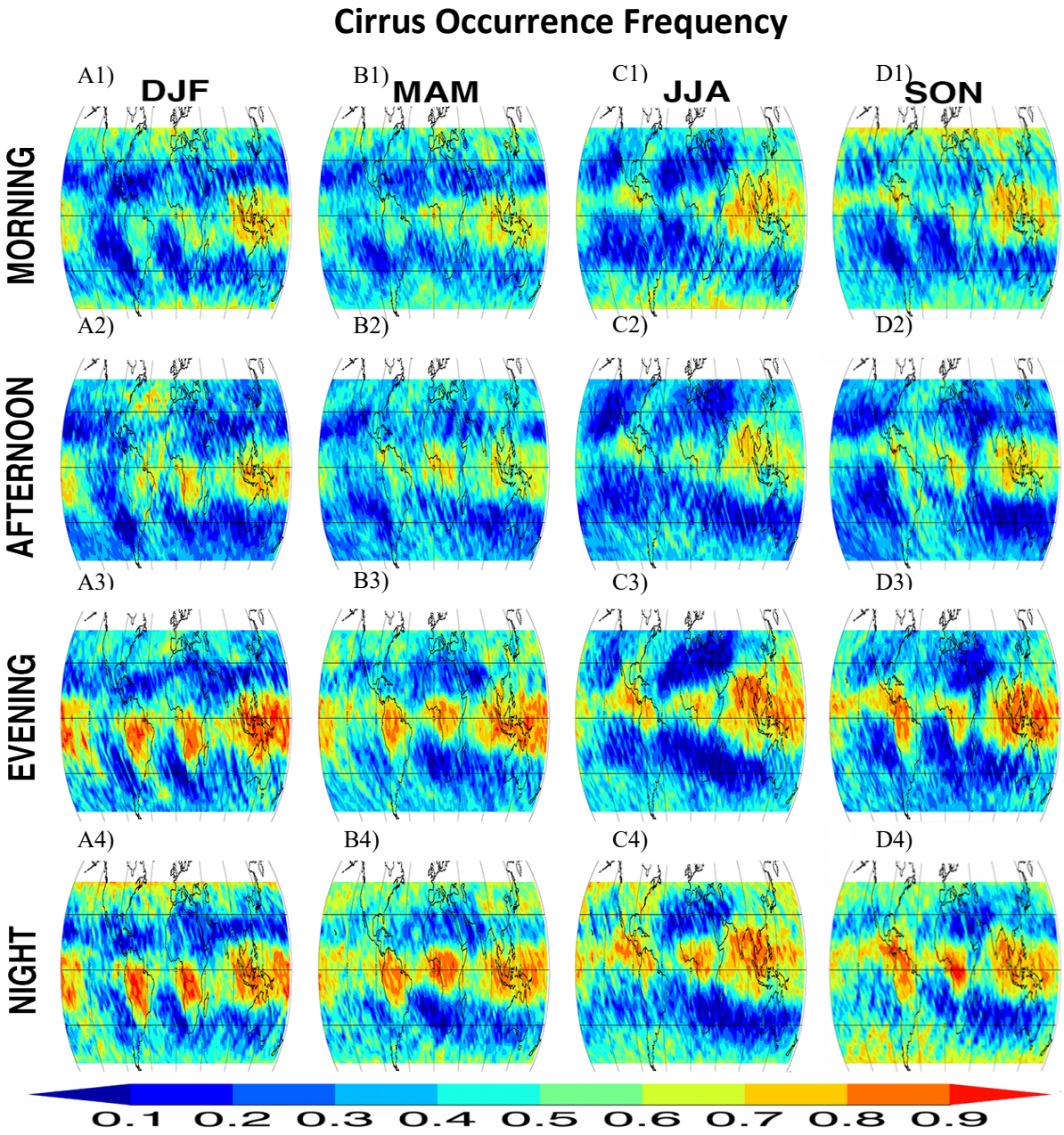

Figure 3.1. Cirrus occurrence frequency based on the ratio of total cirrus observations to the total observations in that lat/lon grid space. Row 1, 2, 3, and 4 corresponding to morning, afternoon, evening, and night, respectively. Column A, B, C, and D corresponding to DJF, MAM, JJA, and SON, respectively.

The values in table 3.1 agree well with previous studies estimating global cirrus occurrence frequencies on the order of 40-50% averaged across the mid-latitudes and tropics (Martins *et al*. 2011; Wylie *et al*. 1994, Sun *et al.* 2011). Table 3.1 also shows that when averaged across the whole dataset there is little seasonal change in cirrus frequency with a spread of approximately 42 – 44% for both the mean and median. Note the term global is being used to represent the entire CATS dataset which ranges from 51° N to 51° S. However, the distribution of cirrus changes significantly both diurnally and seasonally. Figure 3.1 depicts the gridded cirrus frequency with the seasons DJF, MAM, JJA, and SON in columns A, B, C, and D, respectively, and morning, afternoon, evening, and night in row 1, 2, 3, and 4, respectively. This figure shows that within the relatively constant global frequency there are appreciable spatial and temporal variations in cirrus frequency. The CATS data is consistent with previous studies using CALIPSO data that calculated mid-latitude cirrus frequencies on the order of 40%, and up to 90% in regions along the inter-tropical convergence zone (ITCZ; Mace *et al.* 2009; Nazaryan *et al*. 2008). The tropics observe a peak frequency in the evening to night hours, and then dissipate quickly into the morning. In contrast, the mid-latitudes observe a minimum in the afternoon before ramping up to a maximum in the night time that remains steady into the morning hours, which then rapidly decreases as the day progresses. Figure 3.2 shows the mean diurnal frequency cycle for these regions fit with a sinusoidal function. Black, green, red, and blue curves for DJF, MAM, JJA, and SON, respectively, with solid and dashed curves representing the mid-latitudes and tropics, respectively. For each season it is consistently observed that the mid-

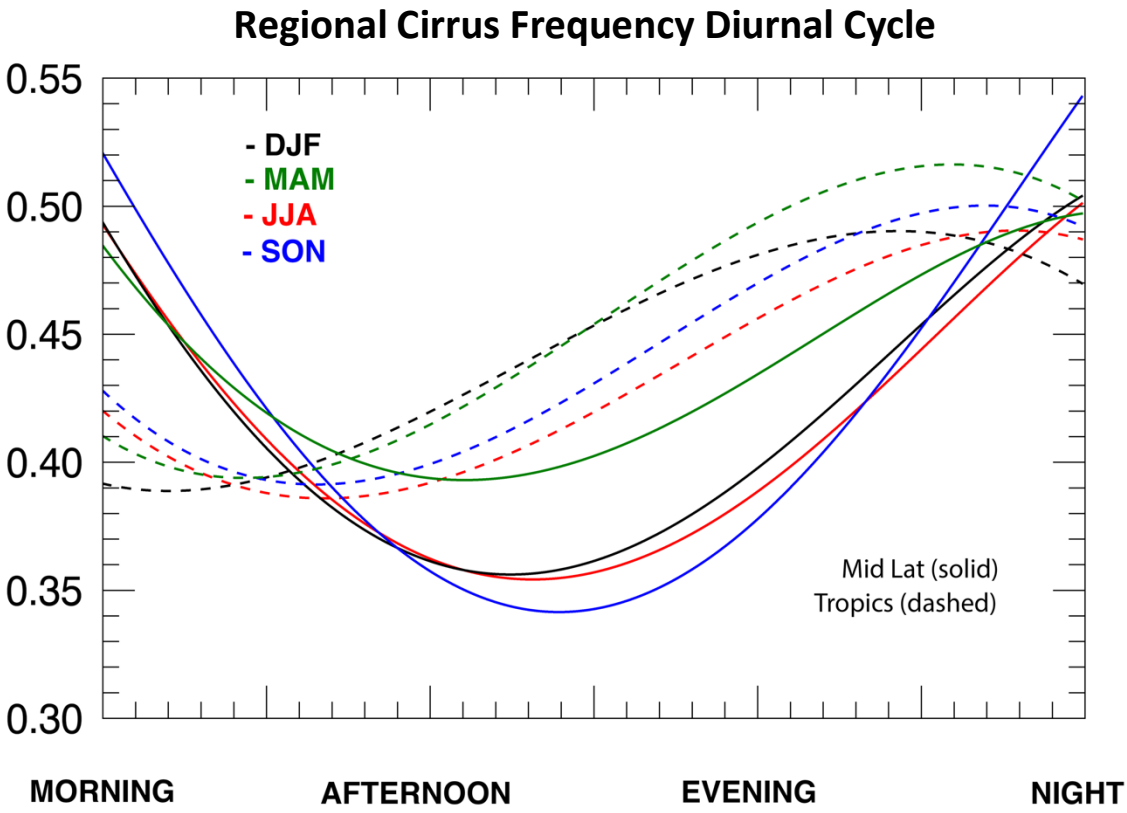

Figure 3.2. Diurnal cirrus frequency cycle for the mid-latitudes (solid), and the tropical (dashed) regions)

latitude diurnal cycle is shifted approximately a quarter of a day $\left(\text{or } \frac{\pi}{2}\right)$ later compared to the tropical diurnal cycle. In the tropics the daily cloud maximum occurs in the evening due to increased solar heating at the surface throughout the day leads to evening convection (Soden 2000; Tian *et al.* 2004). Noel *et al.* (2018) analyzed the diurnal frequencies of CATS cloud observations and observed similar trends with a cirrus minimum occurring mid-day in all regions. In the mid-latitudes the daytime reduction in frequency is influenced by solar heating effects after sunrise causing the sublimation of cirrus layers. Additionally, the amplitude of the minimum and maximum differences is greater for the mid-latitudes compared to the tropical cycle. This is because the tropical region observes both the highest frequency values along the ITCZ, but also the lowest frequency values in the latitudinal

doldrum regions where the Hadley cell causes sinking air, which averaged together yield a reduced fluctuation of frequencies in the tropics (Noel *et al.* 2018). The images in Figure 3.1 show well the daily cycle of cirrus production along the ITCZ in addition to depicting its latitudinal drift through the seasons. In DJF high cirrus frequencies along the ITCZ are almost completely south of the equator, and consist of three regional local maxima over the West Pacific, Congo Basin, and Amazon Basin. These regions are observed to shift north to their most northern extent in JJA where the Amazon and Congo maxima have been almost completely displaced to Central America and the Sahel, respectively. Also, the Western Pacific maxima extends farther Northwest into the Asian continent with the monsoonal flow, and has reduced extent in the Central Pacific.

3.2.1 Global Cirrus Optical and Physical Properties

As mentioned earlier in Chapter 1 cirrus optical and physical properties play a critical role in modulating layer radiative properties. Where and when cirrus form has implications for their dynamic formation mechanism (e.g. synoptic, convective, or orographic; Sassen 2001; Yorks 2014). This affects their ice crystal habit structure, which determines scattering properties. Tropical cirrus primarily consist of convective anvil layers or cirrus that has been sheared away from its host convective system (Lou & Rossow, 2004). Mid-latitude cirrus on the other hand is often generated through synoptic influences such as jet stream dynamics, temperature frontal systems, and Rossby Wave interactions (Sassen 2001), but can also be potentially convective in nature in warmer regions or times of the year.

When operating at only a single look angle it is impossible for a lidar system to decipher specific crystal habits. However, information on cirrus scattering properties can be inferred from certain lidar products. CATS 1064nm channel also has depolarization capabilities where it detects photons that have been linearly polarized perpendicular to their emission. One of the CATS L2_lay products is the layer integrated volume depolarization ratio (VDR; Eq. 3.1). VDR is defined as the ratio of the perpendicular integrated ATB ($\gamma'_{\perp}$) to the parallel integrated ATB ($\gamma'_{\parallel}$). Depolarization ratio yields information on particle sphericity using its correlation with aspect ratio (Sassen 1991; Noel *et al.* 2004). Particles with aspect ratios near unity, like spheroids, have lower depolarization ratios while particles with larger aspect ratios, like columns or irregular polycrystals, have higher depolarization ratios. While no conclusions on exact ice particle habits can be drawn from depolarization ratio alone, it can be infered that regions exhibiting variations in depolarization would also exhibit different scattering properties. In addition to potential differences in habit structure, varying depolarization values can also be the result of surface roughening. Particles that have greater surface roughness tend to depolarize scattered radiation more than smoother prestine ice crystals (Baum *et al.* 2010). Changes in surface roughness for a given habit shape can also impact their scattering and radiative properties (Yang *et al.* 2005; Yang *et al.* 2013; Yi *et al.* 2013).

$$\delta_{layer} = \frac{\sum_{top}^{base} \gamma'_{1064\perp}(z)}{\sum_{top}^{base} \gamma'_{1064\parallel}(z)} \qquad \text{Eq. 3.1}$$

Figure 3.3 is formatted similar to Figure 3.1 displaying the mean integrated depolarization ratio for each season and time of day. Integrated depolarization ratios in the

daytime appear to be higher compared to the nighttime hours due to solar noise. Absolute integrated VDR uncertainty is reported in the CATS data with the relative uncertainty

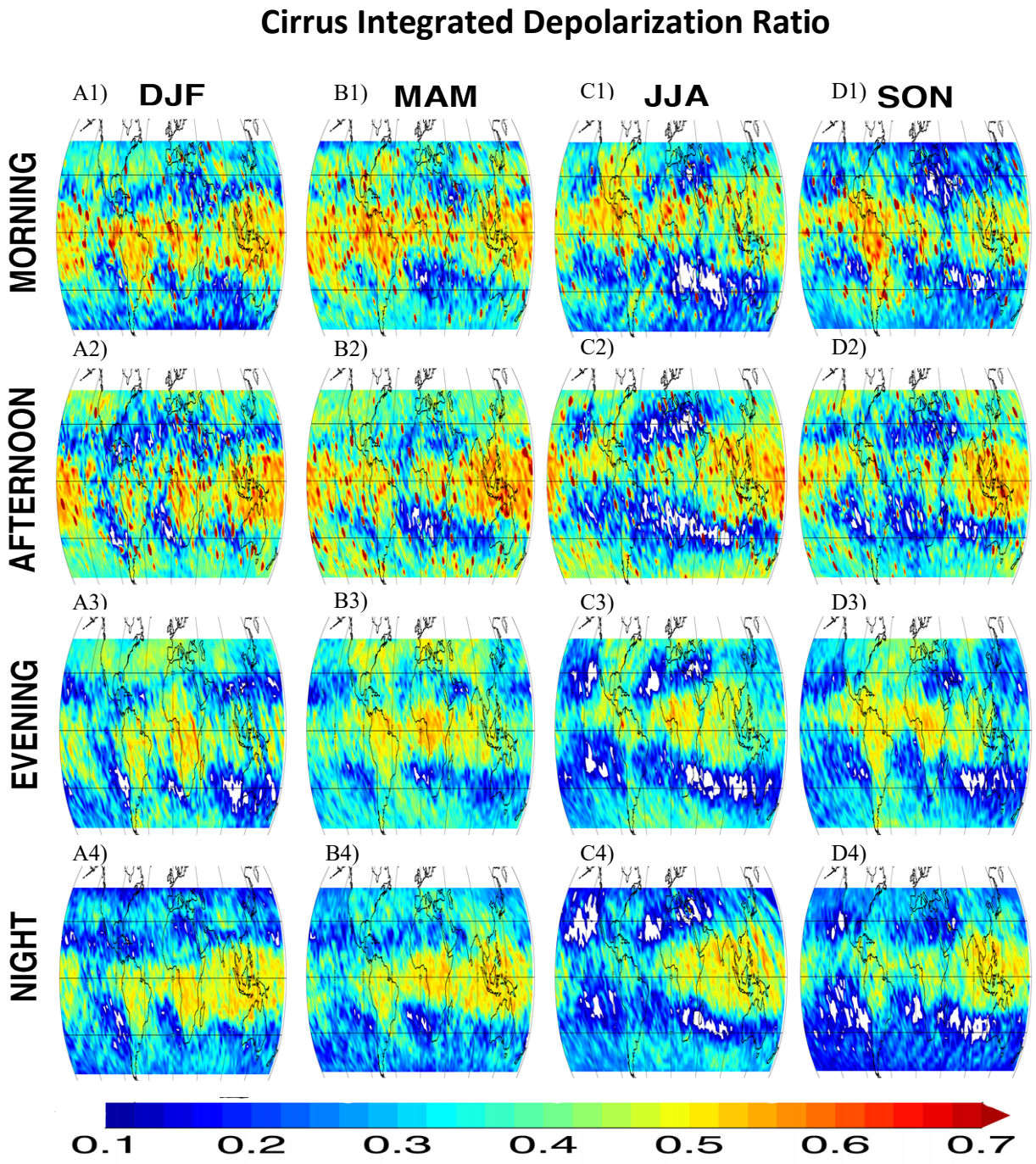

Figure 3.3. Cirrus integrated depolarization ratio from CATS L2 layer product. Row 1, 2, 3, and 4 corresponding to morning, afternoon, evening, and night, respectively. Column A, B, C, and D corresponding to DJF, MAM, JJA, and SON, respectively.

calculated by taking the ratio of absolute integrated VDR uncertainty to the measured integrated VDR. The mean nighttime integrated VDR uncertainty is only 2 – 5% compared to approximately 15% during the day, with the difference primarily due to solar noise. The cirrus in tropical regions exhibit a higher depolarization compared to the mid-latitudes as the cirrus here often form at higher colder altitudes due to the greater depth of the troposphere. Figure 3.4 depicts the diurnal cycle of the median depolarization ratio for each season in the mid-latitudes (solid curve) and the tropics (dashed curve). The median is displayed over the mean as anonymously high values due to solar noise created a daytime mean high bias. The values in Figure 3.4 match up well with standing theory that depolarization is highly anti-correlated with cloud temperature (Sassen *et al.* 2000; Platt *et*

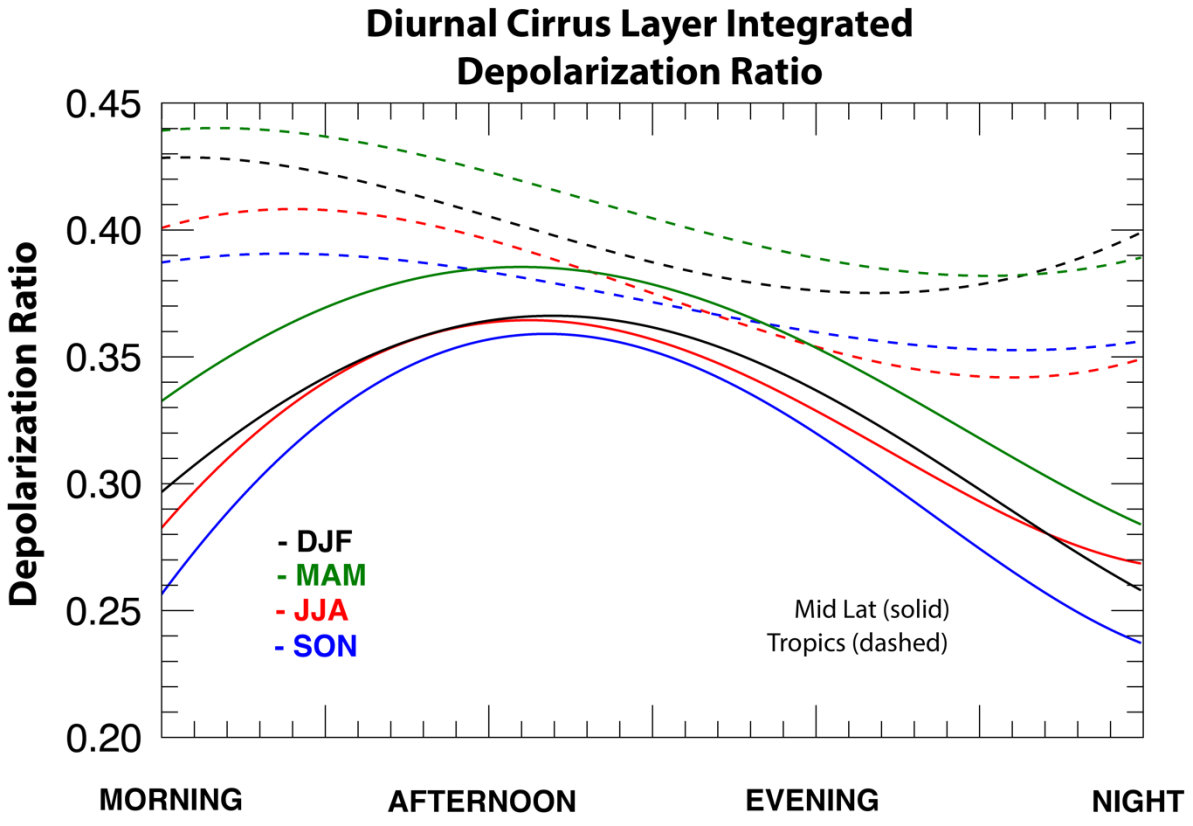

Figure 3.4. Diurnal cirrus integrated depolarization ratio cycle for the mid-latitudes (solid), and the tropical (dashed) regions)

al. 2002). Colder temperatures being correlated with higher depolarization ratios. In Fig. 3.4 both the mid-latitudes and the tropics exhibit their highest depolarization in MAM, which also had the coldest mean cloud top temperatures at 215.9 ±3.5 K in the mid-latitudes and 198.2 ±7.9 K in the tropics, as shown in Table 3.2. Temperature data is provided by NASA Global Modeling and Assimilation Office (GMAO) Modern-Era Retrospective for Research and Applications, version 2 (MERRA-2; Gelaro *et al.* 2017) data, and is reported in both CATS L2 products. Likewise SON and DJF have the lowest depolarization ratios and warmest cloud top temperatures. It was shown by Das *et al.* (2008) and Suneeth *et al.* (2017) that tropopause heights can diurnally fluctuate on the order of 1 km due to surface heating and convection interactions, which results in diurnal fluctuation of cirrus top temperatures. Both these studies were conducted in the tropics at only a few point locations on select days, and showed min/max tropopause heights occurring at varying times of day. However these studies showed the potential for diurnal tropopause height fluctuation, and when averaging across large temporal and spatial scales this is shown in Figure 3.5 by cirrus top temperatures. Fig. 3.5 shows the inverse relationship between cloud top temperature and integrated depolarization ratio in the mid-latitudes. This is indicated by the inverse trend in mid-latitudes curves of Fig. 3.5 and Fig. 3.4, respectively. The tropical cloud top temperatures in Fig. 3.5 shows less diurnal variation then in the Fig. 3.4 depolarization ratios likely due to the increased daytime uncertainty from solar effects.

There are several factors contributing to the depolarization dependence on temperature (Sassen & Benson, 2001). At colder temperatures ice crystal growth becomes more favorable along the z-axis rather than radially outward increasing aspect ratio. Crystals are more geometrically pristine rather than rounded from evaporation and

sublimation. Colder temperature also eliminate potential mixed phase low biases, and also the internal structure of ice crystals becomes more solid than hollow (Sassen & Benson, 2001).

In addition to the depolarization ratio, variations in particle shape can also be

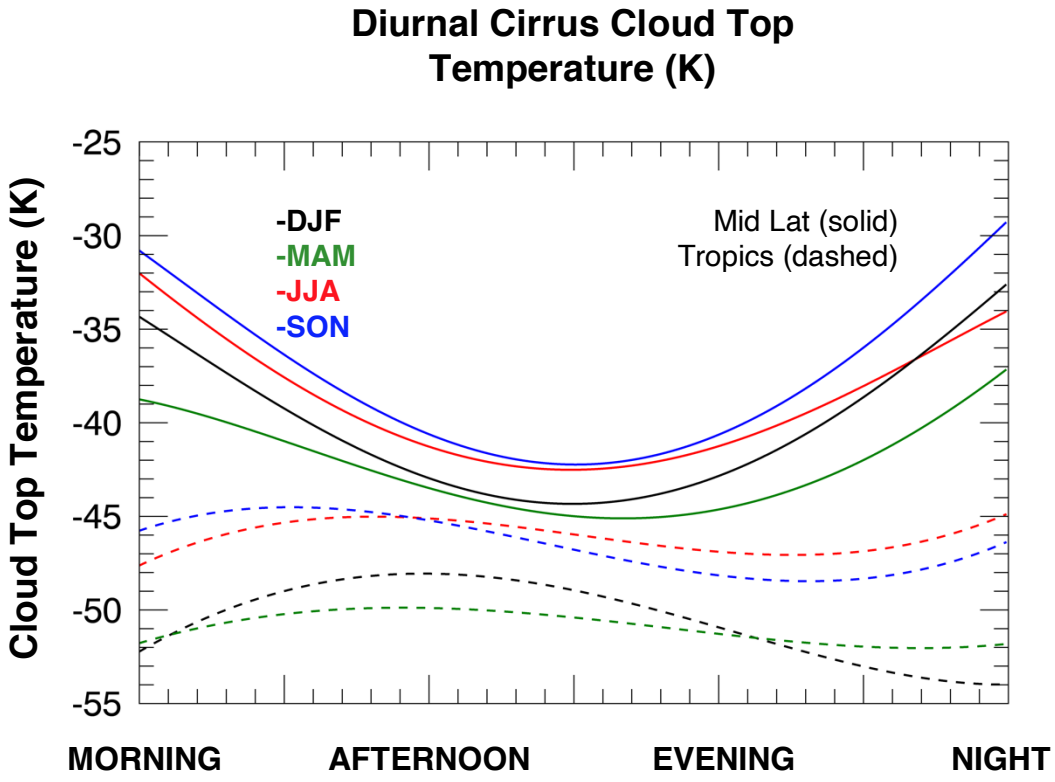

Figure 3.5. Diurnal cirrus layer top temperature for the mid-latitudes (solid), and the tropical (dashed) regions)

Table 3.2 Cirrus Cloud Top Temperatures (K)

Season	Mean		Median		Std. Dev.	
	Mid – Lat	Tropics	Mid – Lat	Tropics	Mid – Lat	Tropics
JJA	217.8	201.8	217.7	198.4	7.4	12.5
SON	217.3	200.3	217.6	196.9	4.9	11.6
DJF	217.0	199.4	216.9	195.3	6.0	11.2
MAM	215.9	198.2	216.1	195.2	3.5	7.9

inferred from the phase function. Operating at a single view angle, CATS only retrieves information from the 180° scatter angle of atmospheric particulates. Previous studies have

derived an approximation (Eq. 3.2) for the phase function in the backward direction (θ=180°) calculated using lidar data (Platt 1979; Platt & Dilley 1981; Baum *et al.* 2010) where γ' is the layer integrated ATB, τ is the layer optical depth, and η is the multiple scattering factor. The CATS multiple scattering factor has been calculated to be 0.51 for all ice cloud layers in the most recent processing (Yorks *et al.* 2018).

$$P_{11}(180°) = 2\pi \frac{2\eta\gamma'}{1 - \exp(-2\eta\tau)} \qquad \text{Eq. 3.2}$$

Figure 3.6 depicts $P_{11}(180°)$ for all seasons and times of day in the same order as previous figures. P_{11} (phase function) is a non-dimensional parameter that represents the amount of energy scattered in a given direction, and is unique to different ice particle shapes and sizes (Yang *et al.* 2005; Yang *et al.* 2013). Figure 3.6 shows the strong diurnal variations in the scattering properties of cirrus clouds.

While it cannot be concluded that the crystal habits present in cirrus change throughout the day, the observed diurnal variations should be resultant from crystal surfaces roughening as they age, larger heavier crystals falling out of the cirrus layer, or crystals becoming aggregated together. One of the clearest gradients present in Figure 3.6 is the land ocean contrast. This is observed over North America, Eurasia, South America and Africa. There is also clear demarcation at some intervals around the 30° latitude mark with higher P_{11} values observed in the mid-latitudes compared the tropics. This is most prevalent in the NE Pacific Ocean. Land ocean contrasts could be caused by variations in temperature, humidity, and also potential differences in ice nuclei. Latitudinal contrasts could be the result of varying formation mechanism within the tropics being more convective in nature compared to the mid-latitudes being more synoptic, which would

likely mean different habit shapes and scattering properties (Lawson *et al.* 2006; Lawson *et al.* 2010). In the tropical regions where a high frequency of cirrus was observed P_{11} values over South America and Africa are comparable to one another while in Eastern

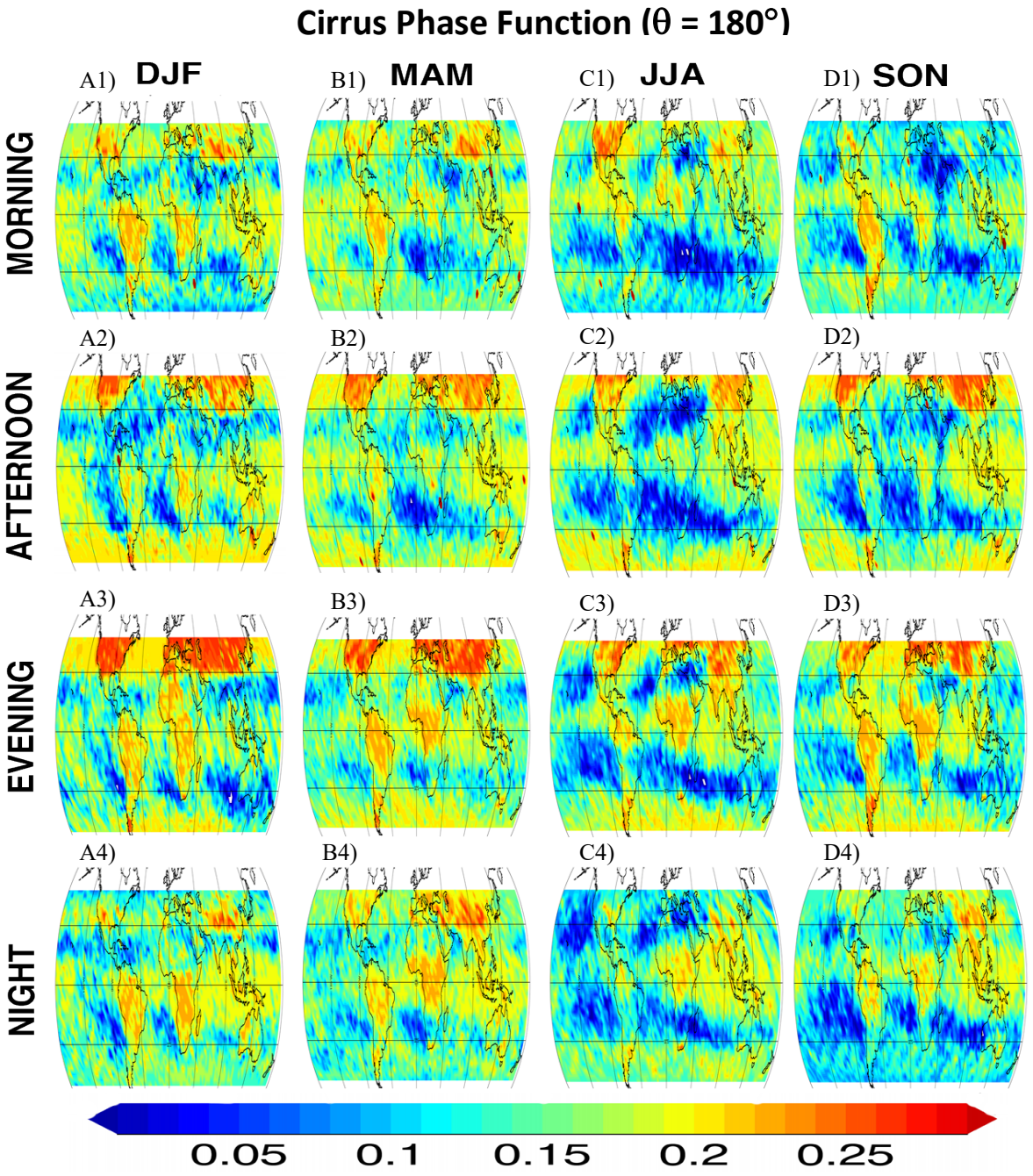

Figure 3..6 Cirrus layer integrated phase function at 180°. Row 1, 2, 3, and 4 corresponding to morning, afternoon, evening, and night, respectively. Column A, B, C, and D corresponding to DJF, MAM, JJA, and SON, respectively.

Indian and Western Pacific Ocean they are noticeably lower. While the formation mechanism is similar for these tropical cirrus the land ocean contrast is still observed. Baum *et al.* 2010 analyzed $P_{11}(180°)$ for an entire year of CALIPSO data, and found similar land ocean contrasts. Guignard *et al.* 2012 examined six years of Atmospheric Infrared Sounder (AIRS), CloudSat, and CALIPSO data which they fit to a scattering properties look up table (Baran *et al*., 2001; Baran and Francis, 2004) to estimate global ice crystal shape, and also found ocean land contrasts over North America, South America, Eurasia, and Africa.

CATS L2_prof data was used to investigate mean cirrus extinction and ice water content profiles, and then integrated to produce optical depth and ice water path, respectively. While the CATS L2_lay product contains layer optical depth and ice water path, full profiles of cirrus layer properties are required for incorporation into radiative transfer simulations, further discussed in section 3.2.2. Therefore integrated profile values are more representative of cirrus layers incorporated into RT model runs. On the same 3° x 3° lat/long grid previous CATS cirrus layers statistics were developed, mean profiles of cirrus extinction, ice water content, and particle effective diameter were calculated for each season and time of day. Ice water content and effective diameter being the properties used to represent cirrus profiles when modeling. This is similar to Hong & Liu (2015) which investigated cirrus using 4-year mean profiles of combined CloudSat and CALIPSO measurements.

Figure 3.7 shows the gridded cirrus optical depth for each season and time of day. Optical depth was calculated by integrating mean cirrus extinction profiles for each grid cell using Eq. 3.3 where σ(z) is the particle extinction coefficient (km^{-1}) at each range bin and *dz* is the CATS vertical resolution of 0.06 km. White shaded regions in Figure 3.7 are where little cirrus was observed with layer optical depths below 0.005. Similar to Figure 3.1 the ITCZ associated ice clouds is clearly visible along the equatorial region, with relatively higher optical depths observed over Indonesia, Congo Basin, and Amazon Basin in DJF, which then shift north into the Northeast Indian Ocean, Sahel, and Central America in JJA, respectively. The mid-latitude regions also exhibit greater optical depths in their respective winter months, DJF in the boreal winter and JJA for the austral winter. Here the cirrus are more associated optically thicker stratiform synoptic systems. This pattern is less contrasted in the Southern Hemisphere where much of the surface south of 30° S is ocean, which still exhibits extra-tropical cyclones, and less convection, during the austral summer compared to the boreal summer. This is shown in Figure 3.8 where the highest mean optical depths observed throughout the day are in the mid-latitudes in DJF, and the lowest in the tropics in MAM. Though cirrus occurrence in MAM (Fig. 3.1) in the eastern Indian Ocean and Indonesian are on par with the rest of the year the images in Figure 3.7 show these regions having considerably lower optical depths compares to the rest of the year. Adam

$$\tau = \sum_{top}^{base} \sigma(z)\, dz \qquad \text{Eq. 3.3}$$

et al. (2016) shows the ITCZ having the least amount of energy in MAM seasons transitioned from the austral to boreal summer. The is considered the dryer season before the monsoonal season begins in JJA. The tropics exhibit a greater diurnal variation than

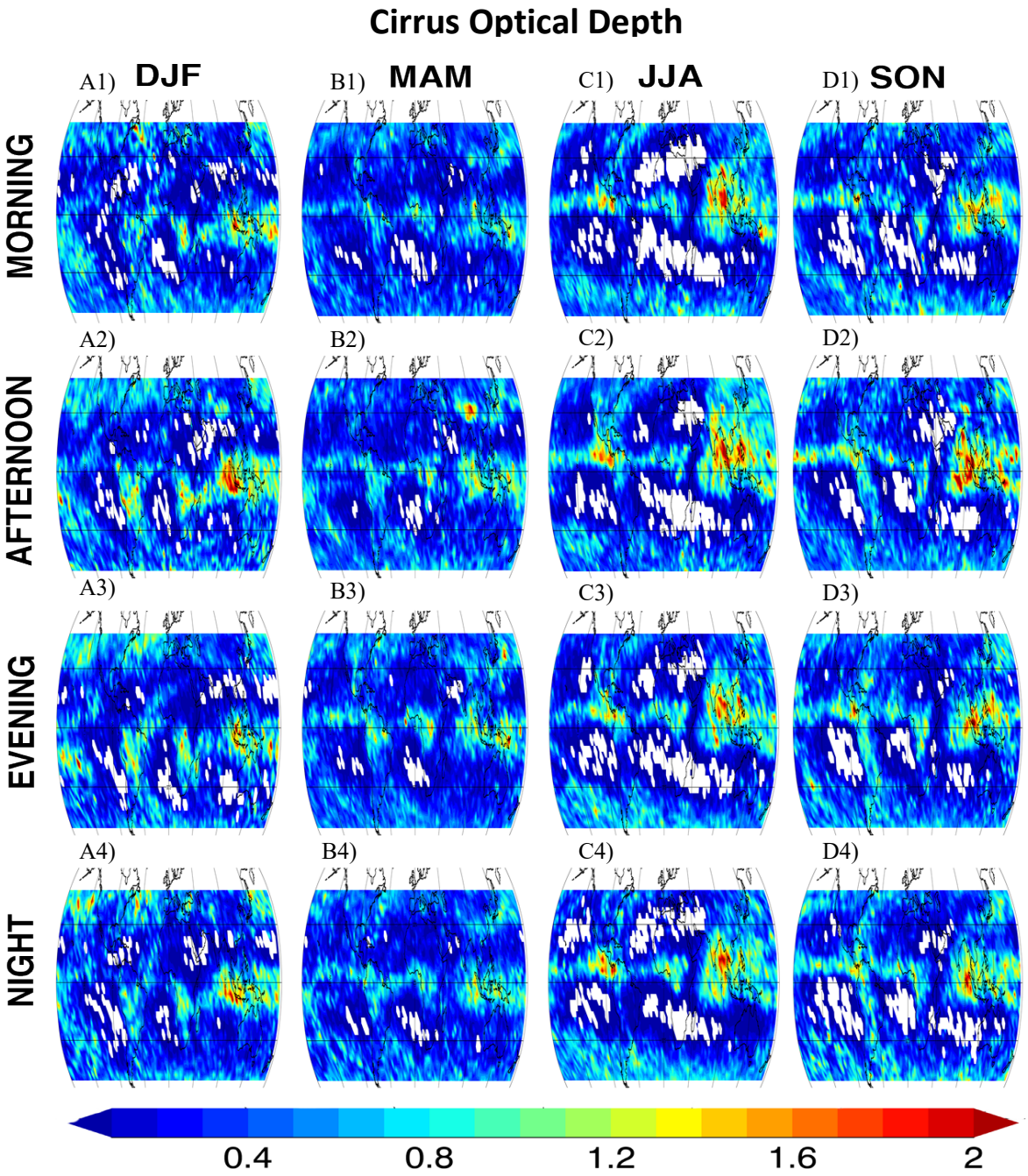

Figure 3.7. Global cirrus optical depth from integrated mean extinction profiles. Row 1, 2, 3, and 4 corresponding to morning, afternoon, evening, and night, respectively. Column A, B, C, and D corresponding to DJF, MAM, JJA, and SON, respectively.

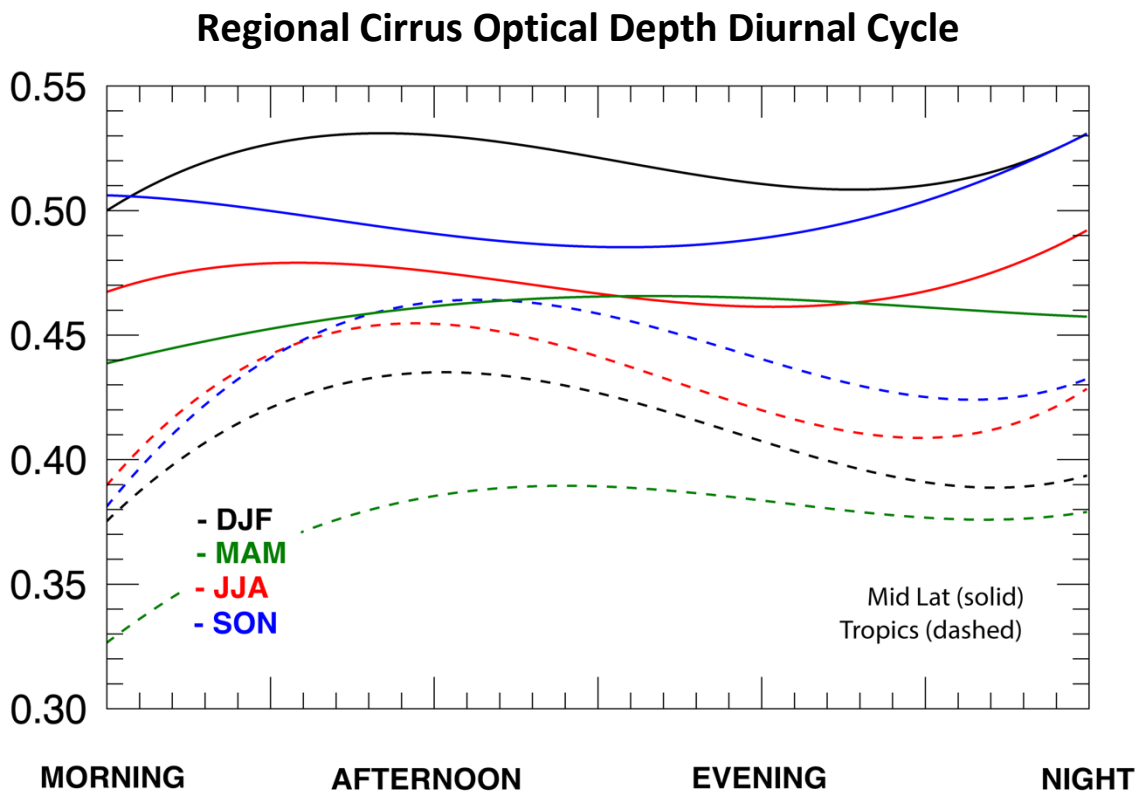

Figure 3.8. Diurnal cirrus mean optical depth cycle for the mid-latitudes (solid), and the tropical (dashed) regions)

the mid-latitudes, with a consistent trend of the maximum optical depth occurring in the afternoon. This could be due to the detection of developing anvil cirrus associated with convection starting in the afternoon, which disperses into the nighttime hours.

Gridded cirrus ice water path was calculated similarly to the optical depth by integrating mean profiles of IWC calculated from CATS L2_prof data. CATS ice water content is derived using a parameterization developed by Heymsfield *et al.* 2014. This is the same method the CALIPSO algorithms use to calculate IWC. The Heymsfield parameterization first calculates particle effective diameter (D_{eff}) using a temperature power-law relationship (Eq. 3.4), which is then incorporated into Eq. 3.5 using the lidar retrieved extinction coefficient to calculate IWC. Effective diameter is calculated using

only the temperature profile (T), where α and β are coefficients with three potential values depending on the temperature range. Note that effective diameter is independent of the lidar signal.

$$D_{eff}(z) = \alpha\, e^{\beta T(z)} \qquad \text{Eq. 3.4}$$

$$IWC(z) = \sigma(z)\frac{0.91}{3}D_{eff}(z) \qquad \text{Eq. 3.5}$$

As IWC is directly proportional to the extinction coefficient gridded figures of IWP are qualitatively similar to optical depth, and therefore are not shown. Figure 3.9 shows the mean IWP for the entire dataset. To verify this method of integrating mean profiles to derive cirrus layer integrated products it was found that this CATS IWP dataset agrees well with other datasets. Eliasson *et al.* 2011 analyzed six global satellite IWP datasets from July 2006 – April 2008 along with six modeled datasets. While CATS derived IWP in Figure 3.9 qualitatively agreed well with all datasets in Eliasson *et al.* 2011, its magnitude

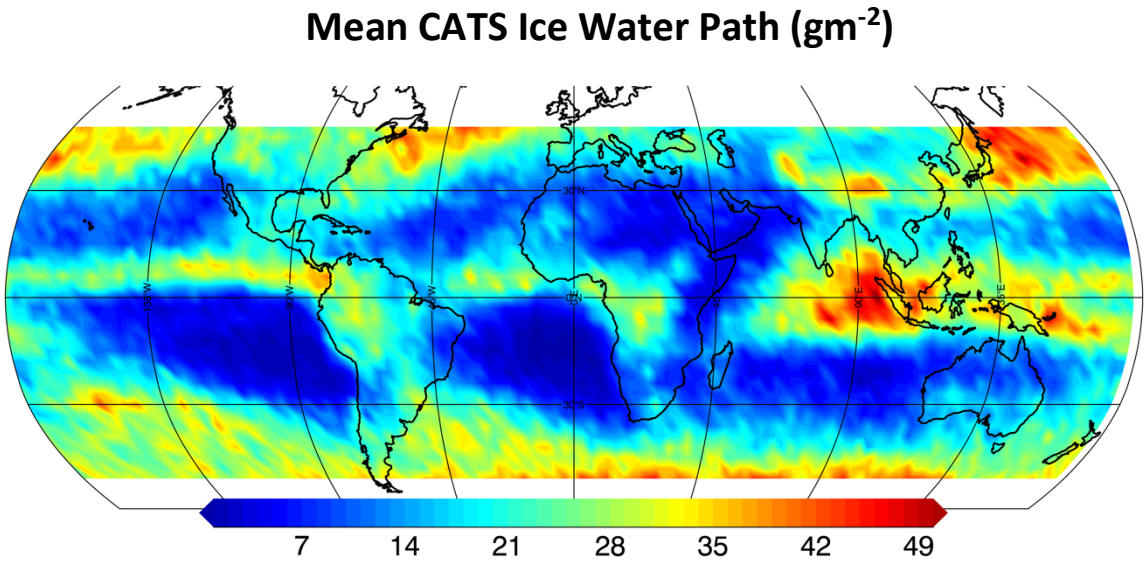

Figure 3.9. CATS mean IWP calculated from integrated mean profiles of IWC for the entire dataset

was quantitatively similar to the precipitation filtered CloudSat IWP and the IPCC AR4 Community Climate System Model v3.0 (CCSM3) IWP.

In addition to the cirrus cloud properties discussed, environmental conditions independent of cloud properties also influence their radiative effect. This includes factors such as the local SZA, surface temperature, and surface albedo. Other than surface albedo, which remains relatively constant on the diurnal scale, environmental conditions also vary both on the seasonal and diurnal scale. To most accurately simulate cirrus radiative effects these factors were also taken into account for all model runs discussed in the following section.

Past studies have inferred the diurnal influence of cirrus radiative forcing by holding mean cloud properties constant, and changing SZA to simulate diurnal progression. Here I have accumulated mean morning and afternoon observations from before local solar noon and after local solar noon, respectively. When incorporated into model simulations the SZA used for all morning runs is calculated to be that at local 9:00 AM, and all

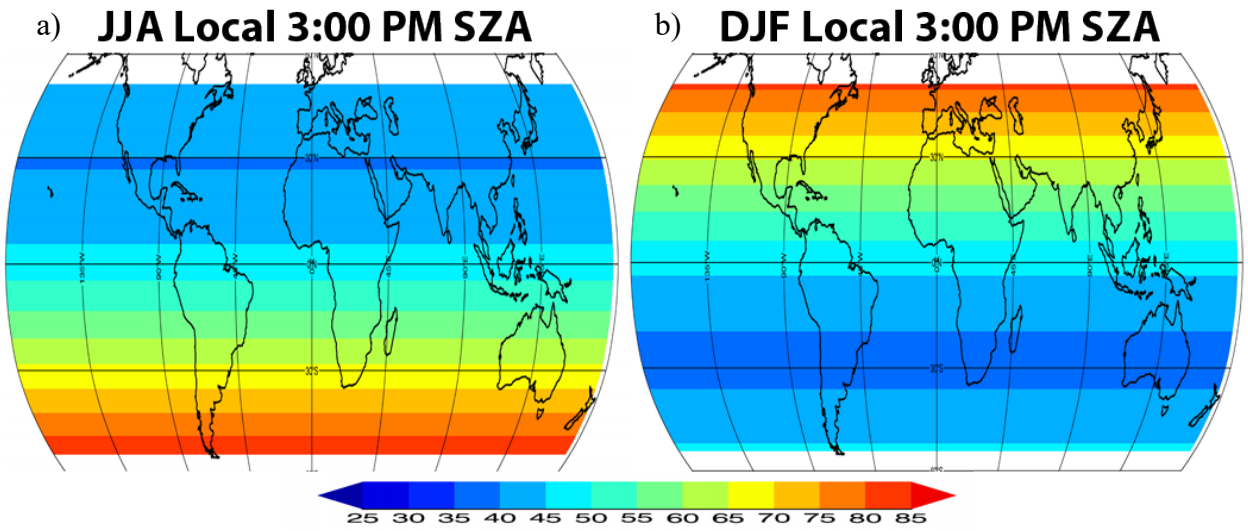

Figure 3.10. Calculated local solar zenith angle at 3:00 PM used in all afternoon radiative transfer model simulations

afternoon runs to be the SZA at local 3:00 PM. Figure 3.10 shows an example of the latitudinal belts of calculated local SZA. The dark blue region of lowest SZA values observed in the austral summer has a greater extent than that in the boreal summer due to the Earth's closer proximity to the sun in DJF.

The global surface albedo was calculated from the Moderate Resolution Imaging Spectroradiometer (MODIS) MCD43C3 Version 6 Bidirectional Reflectance Distribution Function and Albedo (BRDF/Albedo) dataset (Schaaf *et al.* 2015). This albedo dataset is comprised of a running 16-day mean at 0.05 degree resolution produced every day. The mean surface albedo for each season was calculated from the mean of five MCD43C3 datasets of the MODIS shortwave broadband (0.3 – 5.0 μm) albedo. The five chosen files were those corresponding to the 15th and 30th of the first two months, and the 15th of the last month in the season. For example, June 15th, June 30th, July 15th, July 30th, and August 15th for the JJA season. Figure 3.11 shows the mean surfaces albedo calculated for each season. Dark red shaded regions in North America and Asia in DJF and MAM represent snow cover, and contain values in excess of 0.8. The color bar was limited to 0.5 to better show the contrast in surface albedo in other regions. The ocean albedo is set to a constant 0.07, and with the dataset constrained between the 51° latitudes there is assumed to be no sea ice present in any season. Lastly, the mean surface temperature for all times was calculated directly from the temperature profiles provided in the CATS L2_prof product from MERRA-2.

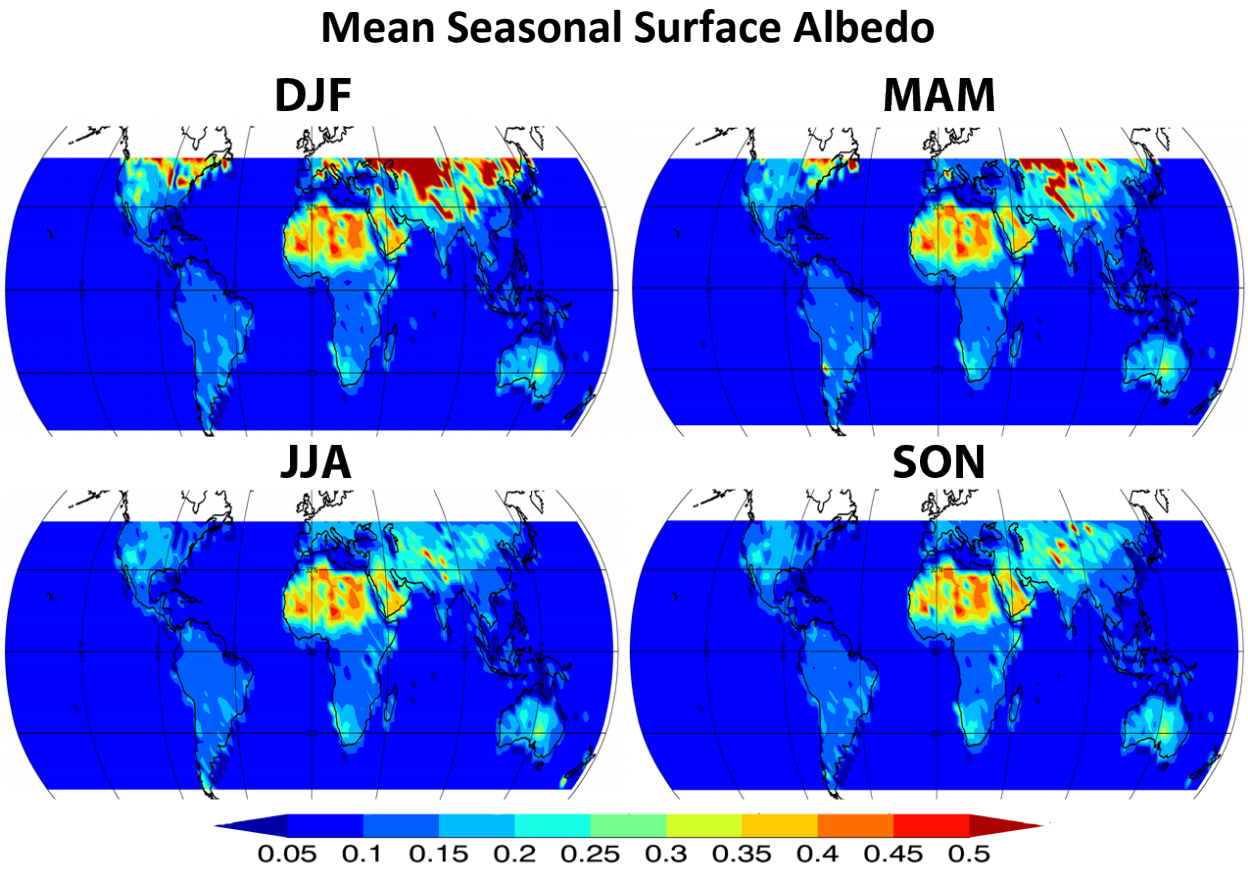

Figure 3.11. Mean surface broadband shortwave albedo for each season calculated from MODIS MCD43C3 version 6 product.

3.2.2 Global Radiative Properties

Cirrus profile and layer products retrieved from CATS were incorporated into a one-dimensional column radiative transfer model to calculate their radiative effects. The radiative transfer model libRadtran (library of radiative transfer; Mayer and Kylling 2005) was used for all RT simulations. LibRadtran is a robust model that offers a high degree of customization to tailor model simulations to the desired research goals. Model configurations are set in an initiation file used in each call to libRadtran. The designated initiation parameters used in this study are listed in table 3.3 including the radiative transfer

solver used, number of streams, molecular absorption parameterization, surface albedo, atmosphere geometry, layer optical depth, and trace gas components.

Table 3.3. Summary of libRadtran Model Components

Model Component	Selection	Source
Radiative Transfer Code	DISORT 2.0	Stamnes *et al.* (1988; 2000) Buras *et al.* (2011)
Number of Streams	6	DISORT Default
Meteorology	NASA GMAO MERRA-2	Gelaro *et al.* (2017)
Molecular Absorption	Correlated - k	Fu and Liou (1992)
Geometry	Pseudospherical	-
Surface Albedo	MODIS	Schaaf and Wang (2015)
Trace Gas Concentrations	CH_4 1.8 ppm N_20 0.32 ppm CO_2	Blasing (2016) LibRadtran Standard Atm.
Ice Scattering Parameterization	Solid Bullet Rosette	Yang *et al.* (2013)

The Discrete Ordinate Radiative Transfer Solver (DISORT) version 2 with 6 streams was chosen for the radiative transfer scheme. This solver was developed by Stamnes *et al.* (1988) then upgraded to version 2 in Stamnes *et al.* 2000, and translated to C from FORTRAN with an updated pseudospherical mode by Buras *et al.* (2011). The correlated-k distribution method from Fu and Liou (1992) was used molecular absorption. This configuration was chosen as it is a favorable setup for calculating integrated shortwave and longwave irradiances by the libRadtran user guide version 2.0.2. It is also similar to that used in previous studies of cirrus radiative effects using libRadtran (Hong *et al*. 2016).

In addition to the model parameters designated by the configuration file, atmospheric and cloud layer profiles are also required. LibRadtran atmospheric inputs

require profiles of height, pressure, temperature, ozone, oxygen, water vapor, and CO_2 gas concentrations. Mean temperature and pressure profiles were calculated directly from those provided in the CATS L2_prof product. MERRA-2 data was also used to retrieve a five day mean of altitude (surface elevation), ozone, and water vapor for each season. The five days chosen corresponded to the same dates used in calculating the surface albedo from MODIS. Two CO_2 profiles corresponding to a standard summer and winter atmosphere were provided within libRadtran data archive.

Cirrus layers in libRadtran are mass defined using IWC(z) and D_{eff}(z), discussed above. The model then solves for extinction (Eq. 3.6) using a formula similar to solving the Heymsfield IWC equation (Eq. 3.5) for extinction. The single scattering parameterization selected in the initiation file uses this to calculate the scattering properties for the associated cirrus layer. Several single scattering parameterizations are available in libRadtran for varying ice habit geometries. The parameterizations developed by Ping Yang *et al.* (2013) were chosen as they offer the most robust options to represent cirrus layers. Yang *et al.* (2013) provides scattering calculations in the spectral region 0.2 – 99 μm on particle effective diameters ranging from 10 – 180 μm for 13 different crystal habits.

$$\sigma(z) = 3\,\frac{IWC(z)}{D_{eff}(z)} \qquad \text{Eq. 3.6}$$

For the first set of radiative simulations of each season and diurnal interval a single ice crystal habit was assumed, which is often standard for cirrus radiation studies (Lolli *et al.* 2017; Campbell *et al.* 2016; Hong *et al.* 2016). This is unrealistic on a global scale, and a primary source of error for cirrus radiative forcing estimates. Section 3.3 will discuss

uncertainties from altering crystal habit as Zhang *et al.* (1999) showed how varying habit parameterizations can have large effects on modeled irradiance. Note that current cirrus scattering parameterizations in 1-D radiative transfer simulations are limited to a single crystal shape assumed randomly oriented throughout the cloud layer unless otherwise developed to have an assumed explicitly defined habit mixture (Baum *et al.* 2005; Key *et al.* 2002; Yang *et al.* 2005; Yang *et al.* 2013). A solid bullet rosette shape was chosen for the initial runs assuming a single globally constant habit due to the common nature of bullet rosette type shapes in cirrus clouds (Lawson *et al.* 2006; Bailey & Hallet 2009, Woods *et al.* 2018).

The total (shortwave plus infrared) cloud radiative forcing (CRF) is equal to the difference in net (incoming minus outgoing) flux between a cloudy and clear cloud-free atmosphere (Ramanathan *et al.* 1989), and is defined as such at any given altitude being investigated (Eq. 3.7). Downward and upward facing arrows indicate incoming and outgoing radiation, respectively. To compute total net CRF at each grid cell four model simulations had to be run for each grid cell. One for each component in Eq. 3.7 corresponding to a shortwave (SW) and an infrared (IR) model run incorporating the cirrus layer, and another SW and IR run with a pristine cloud free atmosphere. For the pristine run all configurations were held constant with the exception of representing of the cirrus layer.

$$CRF_{Total} = [(SW_{\downarrow} + IR_{\downarrow}) - (SW_{\uparrow} + IR_{\uparrow})]_{Cloudy} - [(SW_{\downarrow} + IR_{\downarrow}) - (SW_{\uparrow} + IR_{\uparrow})]_{Clear} \quad \text{(Eq. 3.7)}$$

Figure 3.12 shows the modeled results for total net CRF at the top of the atmosphere (TOA) for all 16 observational periods. The top of the atmosphere is the chosen level as it

is designated by the IPCC to best indicate for surface temperature response (Myhre *et al.* 2013). Additionally, the values depicted are weighted by the frequencies retrieved in Fig.

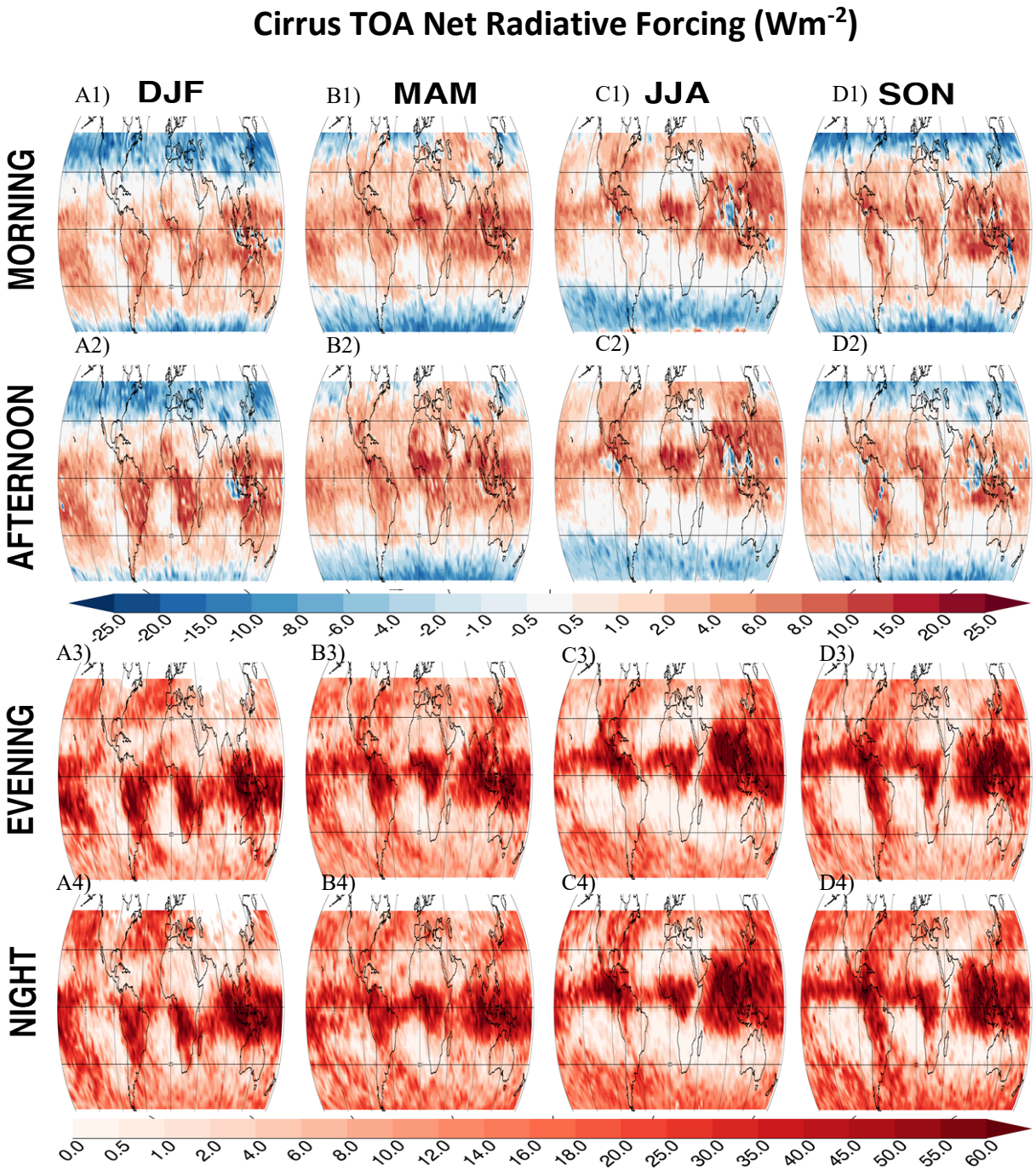

Figure 3.12. Global modeled TOA net radiative forcing. Row 1, 2, 3, and 4 corresponding to morning, afternoon, evening, and night, respectively. Column A, B, C, and D corresponding to DJF, MAM, JJA, and SON, respectively.

3.1. This provides a better estimate of cirrus effect on the climate rather than portraying abosulte modeled irradiance values (Berry and Mace 2014; Campbell *et al.* 2016). Row 1 and 2 show the daytime forcing for the morning and afternoon, respectively, with the blue shaded regions corresponding to negative CRF (cooling), and red shading to positive CRF (warming). Row 3 and 4 show the evening and nighttime total net CRF, respectively. Nighttime forcing is represented on a different scale due to cirrus clouds only warming after sunset in the absence of a shortwave albedo effect.

Cirrus do not always have a warming effect, and there is a clear latitudinal dependence to net total TOA CRF that shifts with the seasons. In the entire northern hemisphere mid-latitudes cirrus exhibit a net cooling effect in the boreal winter (DJF), while in the boreal summer (JJA) cirrus become a net climate warmer in this region. This same pattern is observed in the southern mid-latitudes during the respective austral summer and winter. In JJA the southern hemisphere cooling region in Fig. C1 & Fig. C2 extends to approximately 30° S, and retreats further south in JJA (Fig. A1 & A2).

This latitudinal correlation to the sign change between a heating and cooling effect has two primary drivers, SZA and surface temperature. Surface temperature isotherms (Fig. 3.13) orient themselves primarily in the East-West direction with variations due to surface elevation and land coverage type, while SZA for any given solar time is only dependent on latitude. Three small oceanic regions at the most northern latitudes in JJA (Fig. 3.12 C1) that exhibit cooling correspond to the three northern ocean regions in Fig. 3.13 that exhibit the coolest ocean surface temperatures approximately 12°C. In the winter hemisphere the latitude where cooling sign change occurs is generally observed where the SZA is greater than 65°, indicated by the yellow shading in Fig. 3.10a & b corresponding to the southern and northern hemisphere in Fig. 3.12 C2 & A2, respectively. This pattern was also observed by Campbell *et al.* 2016 that theorized as SZA increases with latitude there exists

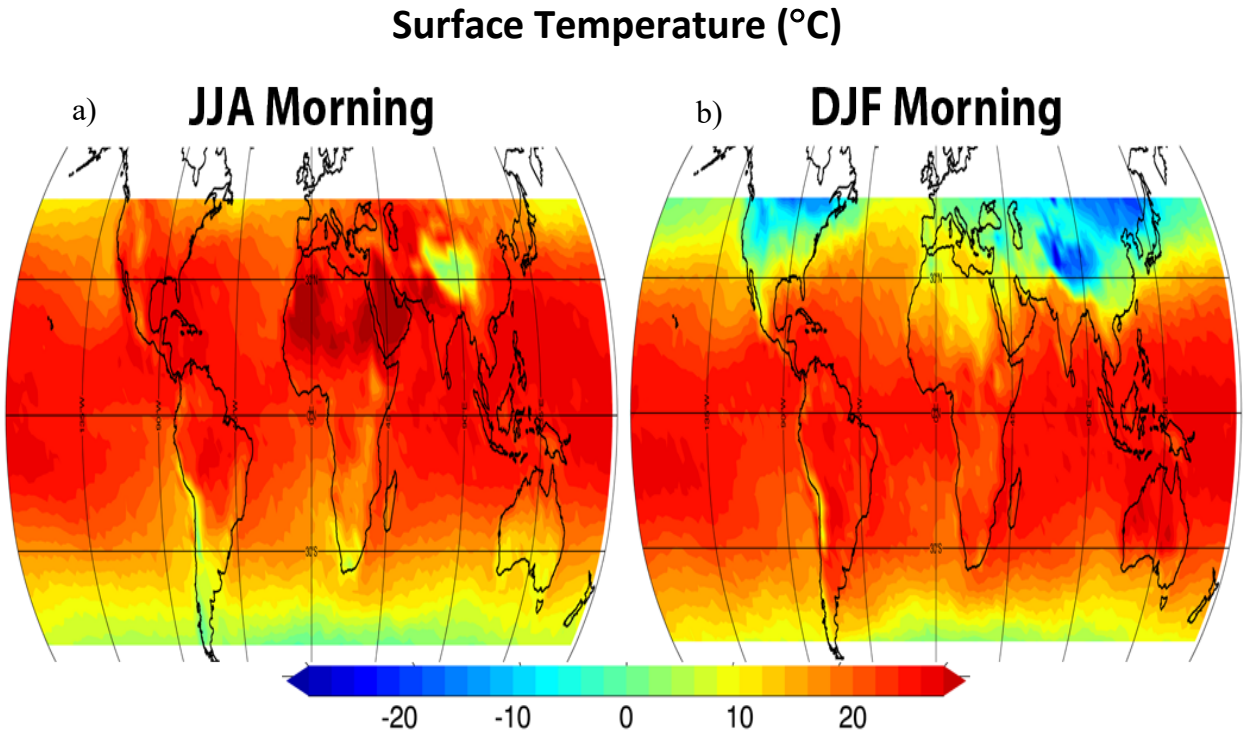

Figure 3.13. Mean surface temperature for JJA & DJF morning calculated from CATS temperature profiles using MERRA-2 surface elevation.

a crossover point in the mid-latitudes where cirrus change sign from warming to cooling. Min *et al.* 2010 also showed the cirrus shortwave albedo effect strengthens (more negative) with increasing SZA to its greatest magnitude at approximately 75°, after which the albedo effect diminishes becoming zero after sunset. This is possibly the reason a narrow region of warming is observed in the most southern regions of Fig. 3.12 C1 where SZA values were approaching 85°.

Just as in the case of the northern summer oceans, the southern hemisphere summer exhibits a sign change demarcation approximately where ocean surface temperatures drop below 12° C. This is observed in comparing Fig. 3.13a & b to Fig. 3.12 C1 & A1, respectively. While mid-latitude summer and winter regions exhibit a strong dependence on surface temperature and SZA, respectively, the spring and fall seasons show that it is the interaction between these variables including others, like optical depth, become more influential. This is observed in the tropics where cirrus almost exclusively warm except in a few regions in the Western Pacific and Eastern Indian Ocean where thicker COD values along the ITCZ are present.

Figure 3.14 depicts the mean and standard deviation of diurnal total net CRF for each season. Due to differences in warming and cooling observed in Fig. 3.12 between the Northern and Southern hemisphere the mid-latitudes here where additionally separated as such. The northern are represented mid-latitudes by the solid curves, and the southern mid-latitudes by the dash-dot-dash curves. The northern mid-latitudes had mean positive daytime CRF in the JJA and MAM, while exhibiting negative mean daytime CRF in DJF and SON. The southern mid-latitudes had a mean negative daytime CRF for all seasons except the austral summer (DJF), which observed mean positive slightly above zero Wm^{-2}. The tropics having the warmest surface temperatures and coldest cloud top temperatures always had a mean positive daytime

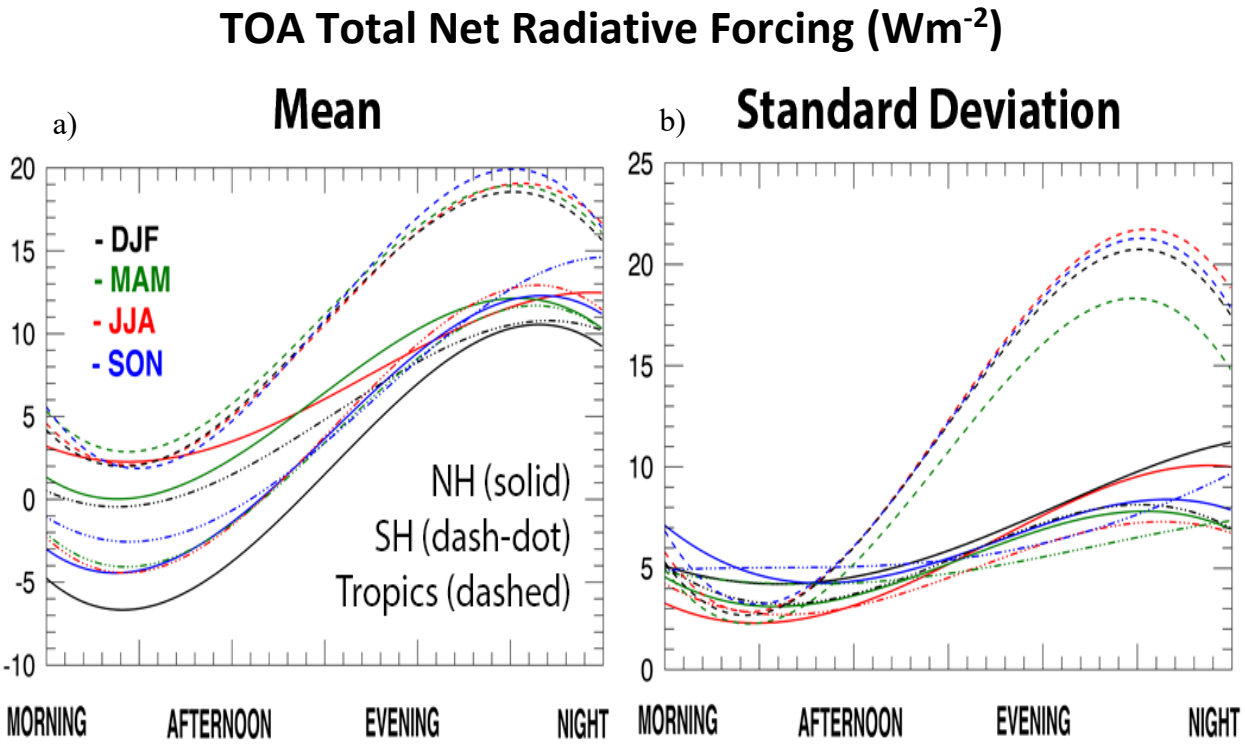

Figure 3.14. Diurnal mean and standard deviation of total net CRF at TOA. DJF, MAM, JJA, and SON by the black, green, red, and blue curves respectively. Northern hemisphere, southern hemisphere, and the tropics by the solid, dash dot, and dashed lines, respectively.

CRF with little variations observed between the seasons. As mentioned above, clouds have a positive CRF at night observed in Fig. 3.14a by all curves. The tropics consistently have a greater nighttime forcing then the mid-latitudes, which was similar in magnitude between the Norther and Southern hemispheres. Again, likely due to the colder cloud top temperatures. Fig. 3.14b shows that all regions and periods had similar standard deviations during the daytime around approximately 2 – 5 Wm^{-2}, and greater in the nighttime. Tropical nighttime standard deviations are approximately 20 Wm^{-2}, about twice as much as the mid-latitudes that ranged between 7 – 11 Wm^{-2}. Nighttime standard deviations are greater than the daytime as the absolute magnitude of CRF is greater at night compared to the day as the IR greenhouse effect is able to influence unencumbered by the modulating SW albedo effect.

3.3 Radiative Forcing Uncertainties

Evaluating radiative forcing uncertainties from 1-D RT simulations is a complex non-linear problem worthy of its own dissertation, and is not the sole focus of this study. CRF uncertainties are a product not only of measurement and instrument uncertainties, but also uncertainties in the model itself and the associated parameterizations (Cordero *et al.* 2007). This includes, but not limited to, errors inherent to the DISORT radiative transfer solver (Stamnes *et al.* 2000), effect due to number of streams used, and scattering parameterizations (Yang *et al.* 2013).

The influence of scattering parameterizations for varying ice crystal habits has been emphasized as a large source of cirrus RF uncertainty (Wendisch *et al.* 2005; Zhang *et al.* 1999). The above CRF discussion in sections 3.2.2 came from model results using a single habit assumption, which the use of a single scattering parameterization for all observations

has been common practice (Hong *et al.* 2016; Hong & Liu 2015, Campbell *et al.* 2016; Lolli *et al.* 2017). I theorize that parameterizing cirrus habits more dependent on their region and season will yield better constrained estimates of their radiative effect. Here I represent CRF uncertainty as the relative difference between global cirrus CRF using the solid bullet rosette parameterization, and global cirrus CRF using a custom habit parameterizations based on regions an season (Eq. 3.8). This is similar to other studies which represented cirrus CRF uncertainty as the differences between modeled results. Campbell *et al.* 2016 estimated CRF uncertainty as the differences in modeled CRF using optical properties calculated from two different lidar ratios. Hong *et al.* 2016 estimated cirrus CRF uncertainty as the difference in model runs resultant from initiating runs using coincident data between CALIPSO and CloudSat.

$$CRF_{uncert} = \frac{|CRF_{custom} - CRF_{Bullet}|}{|CRF_{Bullet}|} \qquad \text{Eq. 3.8}$$

As mentioned earlier the solid bullet rosette was chosen due its relative commonality. However, cirrus clouds rarely exhibit a single crystal habit and can often have columns, spheroids, plates, and aggregates/irregulars. It has also been observed for aggregate type crystals to be relatively common in cirrus, especially those associated with convection (Yorks 2014; Lawson *et al.* 2006; Lawson *et al.* 2010). To calculate the CRF uncertainty I ran libRadtran over the entire dataset again using a custom habit parameterization based on region and season. An aggregate of column-like crystals was used in all regions more associated with convection. This included the entirety of the tropics between 30° north and south, and also over land in the mid-latitudes during the respective summer seasons (i.e. JJA for the north and DJF for the south). All other regions

and seasons remained with the bullet rosette. However, due to the land ocean contrast in P_{11} observed in Fig. 3.6 the bullet rosette over all mid-latitude ocean observations was altered to have a roughened surface instead of a smooth surface. This was chosen because the roughened bullet rosette has a lower phase function at 180° compared to the smooth bullet rosette (Yang *et al.* 2013), which was the observed difference between ocean and land P_{11} in Fig. 3.6.

Figure 3.15 shows the global TOA net CRF for the entire dataset similar to Fig. 3.12. The modeled CRF values shown in Fig. 3.15 were calculated using an identical libRadtran configuration to those in Fig. 3.12 with the only exception being the varying scattering parameterizations described in the prior paragraph. All habit parameterizations used were those calculated in Yang *et al.* (2013) provided in the libRadtran. It is immediately evident that the habit parameterization change in the tropics to an aggregate shape has severely reduced the CRF, and in most regions caused a flip in sign from warming to cooling. The same is observed in the northern hemisphere summer over land, where the aggregate parameterization was also used. The oceans where the bullet rosette parameterization was changed to represent a roughened particle also exhibited a decrease in CRF, and in many places a sign change. This is most noticeable over the summertime mid-latitude oceans where much of these regions exhibited warming in Fig. 3.12, however in Fig. 3.15 now show cooling or white shaded regions indicating weak CRF around zero Wm^{-2}. Yi *et al.* (2013) showed the impact of surface roughening on ice crystals often lead to a strengthening of the shortwave albedo effect, and relatively little change on the infrared greenhouse effect causing a reduction in total net CRF. Lastly, the tropical regions in the doldrum latitudes, which exhibited low frequencies (Fig. 3.1) and optical depths (Fig. 3.7),

now exhibit large white shaded regions indicating near zero CRF, in contrast to previously exhibiting weak warming on the order of 1 – 5 Wm^{-2} in Fig. 3.12. This is most prevalent

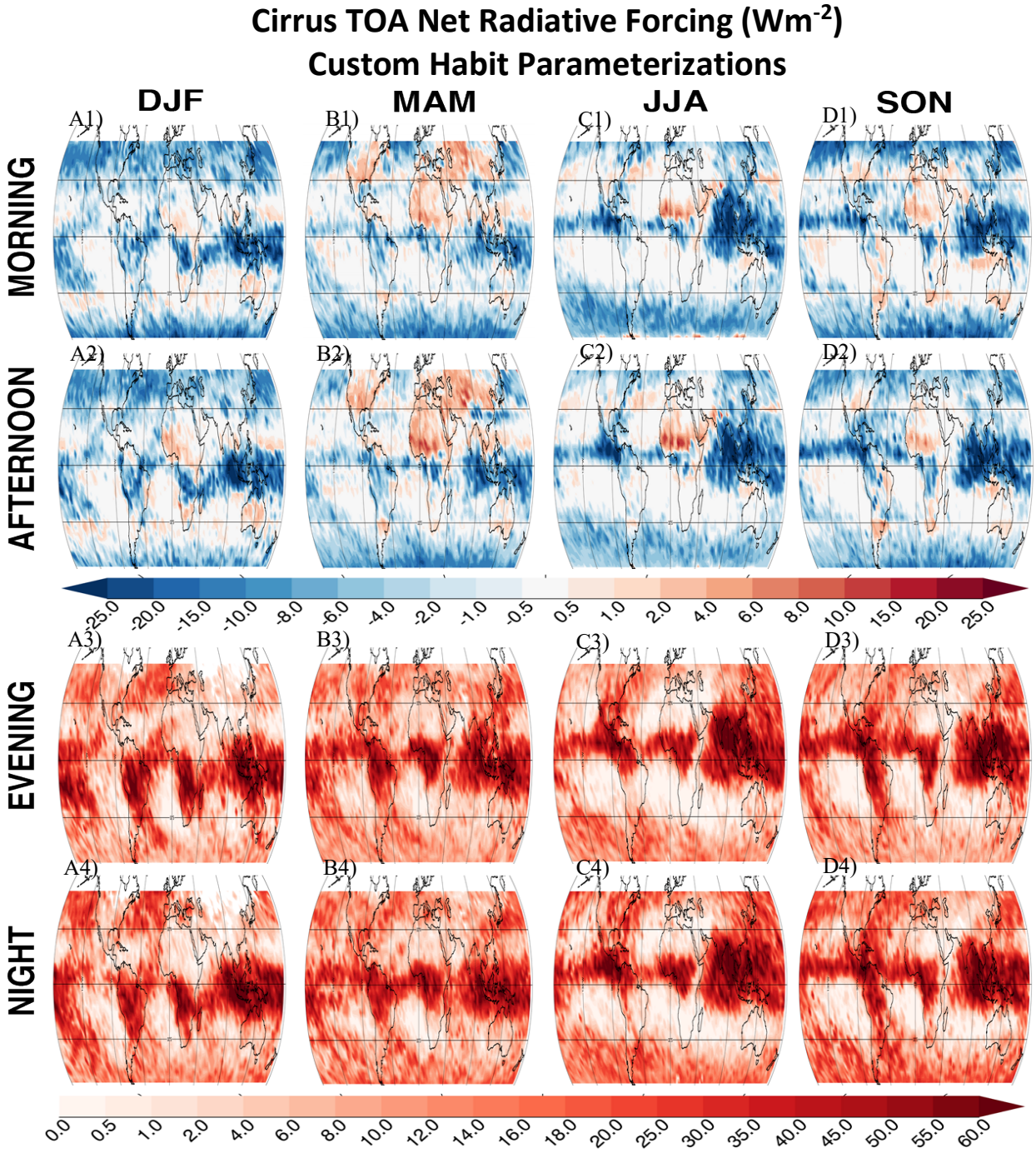

Figure 3.15. Global modeled TOA net radiative forcing using varied ice crystal habit parameterization per region and season. Row 1, 2, 3, and 4 corresponding to morning, afternoon, evening, and night, respectively. Column A, B, C, and D corresponding to DJF, MAM, JJA, and SON, respectively.

in the Eastern Pacific region. While most regions exhibited a significant reduction in net CRF with the aggregated parameterization, Northern Africa is an exception. The MAM and JJA seasons were less affected than DJF and SON, and this is due to the greater surface temperatures and thin optical depths observed in the spring and summer. The positive CRF observed in the Sahara in DJF and SON are correlated to the location of the warmest surface temps in excess of 30° C. The Saharan region as a whole being less affected by the habit parameterization change is likely due to the high surface albedo (Fig. 3.11) and surface temperatures occurring throughout the entire year, which is the primary difference between the Sahara and the rest of the tropics.

In contrast to the differences observed in the daytime total net CRF, there was little to no change observed in nighttime forcing across all regions. Cirrus crystal habit parameterizations primarily effect shortwave scattering properties, and have a minimal effect on broadband infrared radiances (Wendisch *et al.* 2007). Figure 3.16 depicts the same statistics as Fig. 3.14a with the new parameterizations. The nighttime mean forcing for each region remained mostly constant, and has increased by approximately 1.00 Wm^{-2} in the tropics compared to Fig. 3.14a. The daytime mean forcing for each region, however, now has a mean cooling effect with negative CRF, and are all relatively similar in magnitude 0 to -5 Wm^{-2}, however the standard deviations remained similar to those shown in Fig. 3.14b. Figure 3.17 shows histograms of the daytime relative CRF uncertainty calculated by Eq. 3.8 for the northern hemisphere (black curve), southern hemisphere (red curve), and the tropics (blue curve) in each season. Nighttime uncertainty histograms are not displayed as all had peaks < 1%, and median uncertainties ranging from 1 – 4%. Table 3.4 lists the median CRF uncertainty for each curve displayed in Fig. 3.17. Note the mean

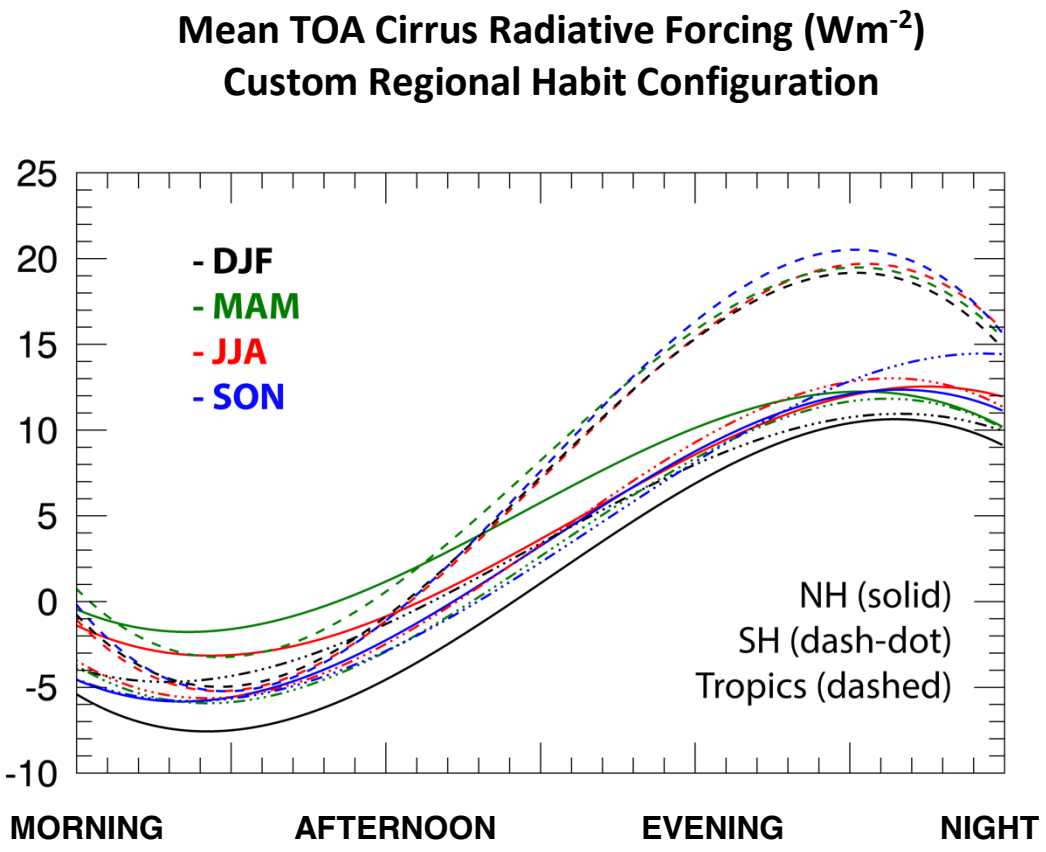

Figure 3.16. Diurnal mean total net CRF at TOA for Northern Hemisphere (solid curve), Southern Hemisphere (dash-dot curve), and the tropics (dashed curve) for each region using the custom habit parameterization configuration.

and standard deviation are not reported as irregular anomalously high uncertainties caused by low CRF values in the denominator of Eq. 3.8 skewed mean and standard deviations to be unrepresentative, and the medians most represent the histograms shown. The tropics had relatively consistent peak uncertainties with all seasons having the same change in habit parameterization from bullet to aggregate, and median uncertainties ranging from 110 – 120%. The lowest uncertainties were observed in the mid-latitude winter seasons with the NH and SH having 35.83% and 33.2% uncertainty, respectively. This is due to the only parameterization change for these regions and seasons being the roughening of the bullet rosette over the ocean. The highest uncertainties were observed in both the NH and SH

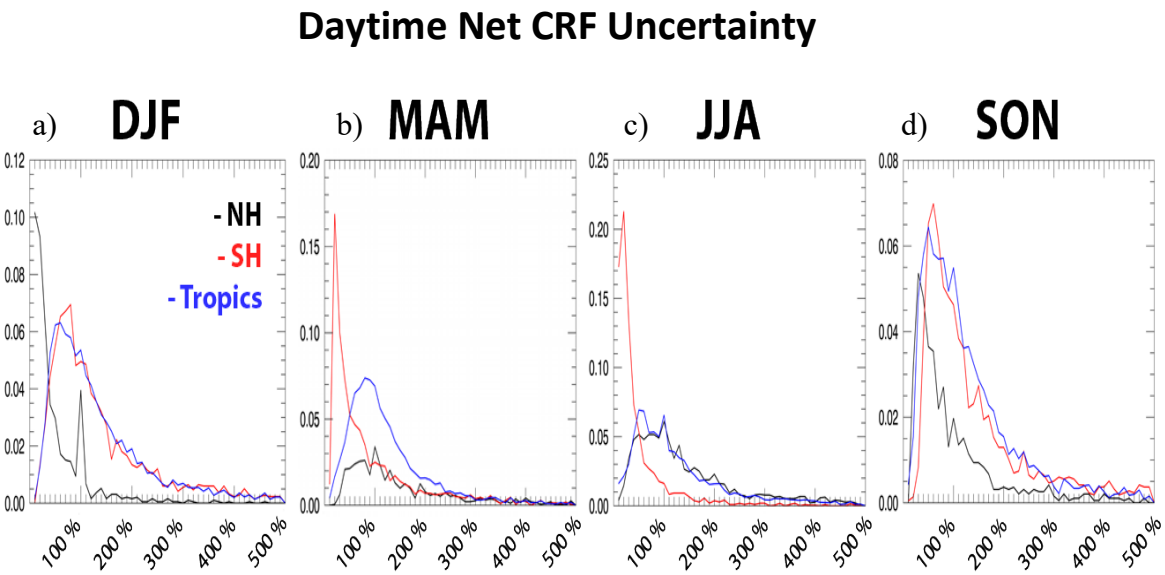

Figure 3.17. Daytime relative uncertainty histograms of net CRF calculated from Eq. 3.8. DJF, MAM, JJA, and SON are depicted in a, b, c, and d, respectively. The northern hemisphere, southern hemisphere, and tropical regions are depicted by the black, red, and blue curves, respectively.

Table 3.4 Median Daytime CRF Uncertainty

	DJF	MAM	JJA	SON
NH	35.83 %	138.0 %	131.1 %	77.54 %
SH	123.0 %	67.59 %	33.20 %	123.4 %
Tropics	120.5 %	109.9 %	113.4 %	113.2 %

mid-latitudes with median uncertainties exceeding 120% in the SH, and over 130% in the NH, in both their respective spring and summer seasons. This is observed as both the spring and summer seasons in the mid-latitudes experienced sign change from a mean warming to a mean cooling.

These uncertainty patterns conclude that roughened ice particles and aggregate shapes effectively scattered more shortwave radiation causing a greater albedo effect during the daytime. The increased scattering uncertainty observed in the aggregate habit parameterization was consistently greater than 100%. However, uncertainty caused by roughening the bullet rosette surface was more dependent on season. The NH and SH mid-latitude spring seasons had the highest uncertainties of their respective regions, and

relatively lower in their respective autumn seasons though both had the same change in habit parameterizations. Meaning the effect of increased crystal surface roughness was greater in warmer regions that initially had a large area of positive CRF causing a sign change. In contrast, the autumnal seasons of the mid-latitudes that initially exhibited large areas of negative had lower uncertainty on the order of 70%.

As mentioned at the beginning of this section, CRF uncertainty is a difficult parameter to quantify and is a function of the uncertainties from all model components. Here, I represented uncertainty as that introduced by assuming varying crystal habit scattering parameterizations for a cirrus layer because it is one of the primary assumptions and sources of uncertainty when modeling cirrus radiative effects. This introduced an uncertainty on the order of 100% for daytime RF estimates, but it was shown crystal habit had much less of an effect on nighttime forcing in the absence of solar shortwave scattering with uncertainties 1 – 4%. However, nighttime RF uncertainties are also affected by measurement uncertainties, and are likely higher than this value.

Similar to the depolarization ratio uncertainty, the relative extinction uncertainty for all range bins containing ice clouds was computed by taking the ratio of the reported absolute extinction uncertainty, reported in all CATS level 2 data, to the calculated extinction coefficient in the associated bin. Figure 3.18 shows a histogram of relative extinction uncertainty for the CATS cirrus dataset. The red curve representing daytime observations and black curve for nighttime. The peak of the daytime uncertainty is approximately 50% and the peak of the nighttime uncertainty is about 20% less at approximately 30%. The difference between the median uncertainties is approximately 10% with the median daytime uncertainty at 62.3% and the nighttime at 52.7%. Just as in

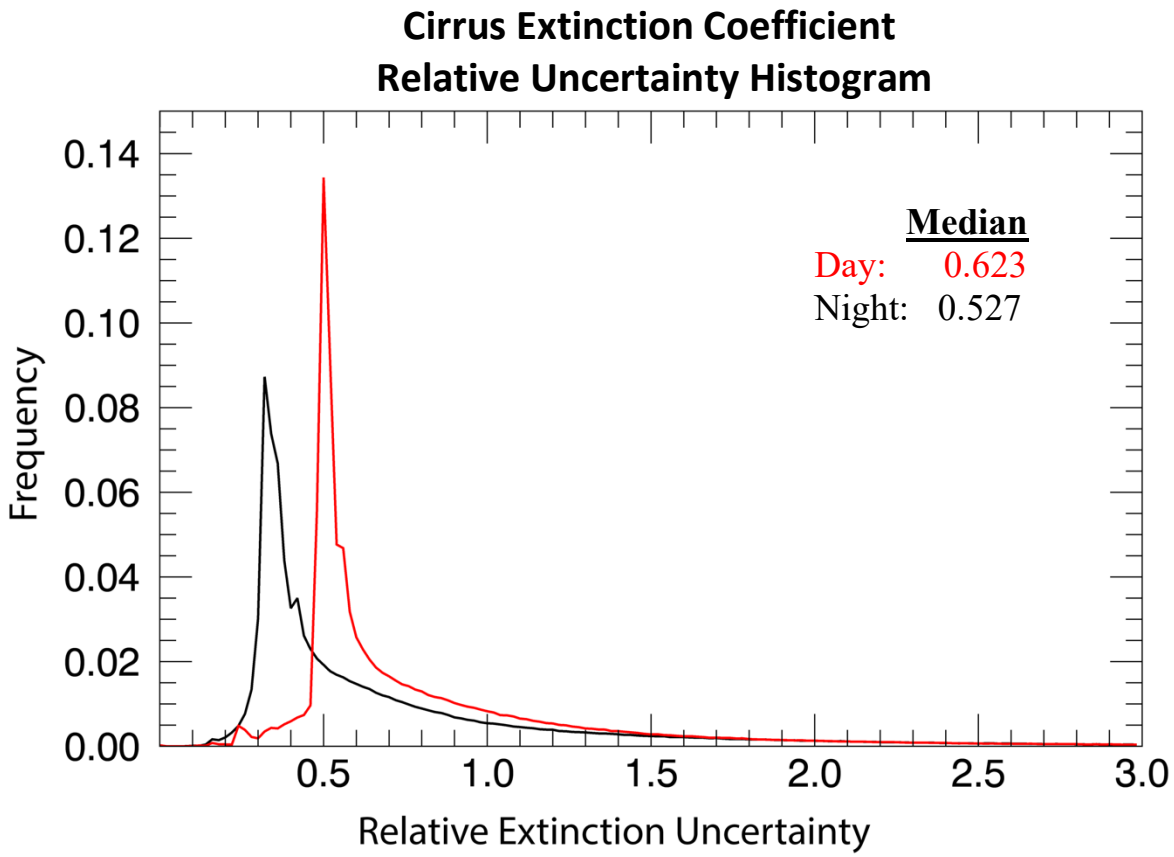

Figure 3.18. Extinction relative uncertainty for night and day time datasets shown by the black and red curve, respectively.

the case of the depolarization ratio, this is expected due to the reduced calibration uncertainties as a result of reduced SNR during the daytime from solar noise. The extinction uncertainty is considerably higher than that for depolarization due to the propagation of error of all variables used to calculate extinction. Eq. 3.9 shows a generalized form of the propagation of errors formula. The terms in Eq. 3.9 represent the particulate two-way transmission (T_p^2), particulate backscatter (β_P), and general calibration uncertainty (C). Of these, the calibration uncertainty has the biggest day/night change almost doubling from 16 – 18% during the nighttime to 7 – 10% in daytime data (Pauly *et al.* 2019). CATS uncertainties are calculated following the procedure in Young *et al.* 2013.

T_p^2 and β_P are first shown in Eq. 1.2 and 1.3, respectively, with the lidar ratio uncertainty also inherently represented in these terms.

$$\delta_{\sigma_P} = \sqrt{\left(\frac{\partial \sigma_P}{\partial T_P^2}\,\delta T_P^2\right)^2 + \left(\frac{\partial \sigma_P}{\partial \beta_P}\,\beta_P\right)^2 + \left(\frac{\partial \sigma_P}{\partial C}\,\delta C\right)^2} \qquad \text{Eq. 3.9}$$

Figure 3.19 shows histograms of the of relative ice water content uncertainty calculated in the same manner as the relative extinction uncertainty. The IWC uncertainty is considerably higher than the extinction uncertainty as IWC is a function of extinction with additional error propgated from inherent uncertainties in the power-law relationship used to calcuate IWC and D_{eff}. Heymsfield *et al.* (2014) reports the uncertainty for these

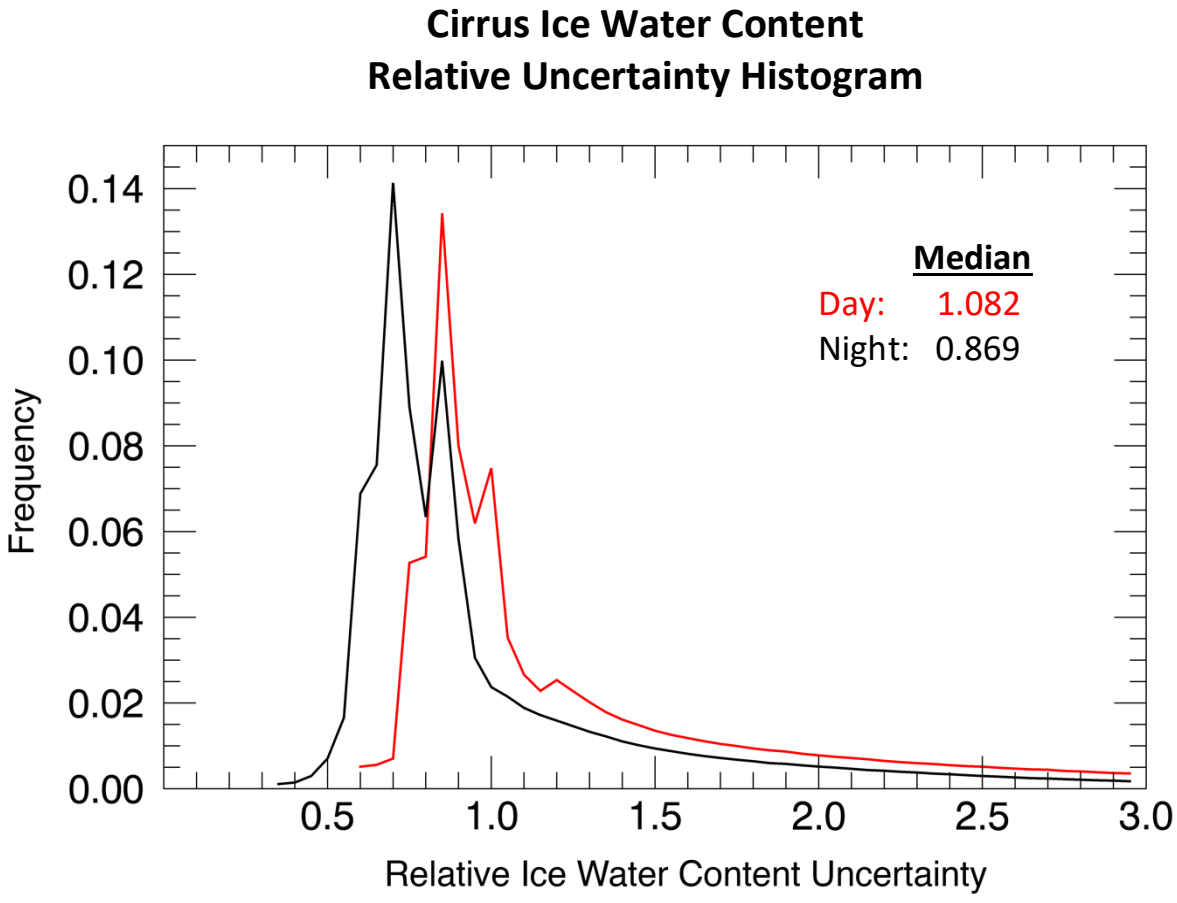

Figure 3.19. Ice water content relative uncertainty for night and day time datasets shown by the black and red curve, respectively.

uncertainty to be an estimated 31%. The peaks of the IWC uncertainties are multimodal, however, the median daytime uncertainty is expectadly higher than the nighttime uncertainty with median daytime uncertainty of 108.2% and median nighttime of 86.9%. The IWC uncertainty histograms exhibit more overlap than the extinction uncertainy histograms (Fig. 3.18) showing that uncertainty in the Heymsfield *et al.* (2014) parameteriation is a significant contributor to IWC uncertainty.

These measurement uncertainties in IWC and extinction also contribute to the nighttime RF uncertainty that is more dependent on longwave IR interactions. Nighttime RF uncertainty is likely additionally dependent on varying optical depth and temperature variables, and cannot be directly estimated here without further study. Though due to the CATS measurement uncertainties it is likely greater than the 1 – 4% reported in section 3.3 due to the effects of habit change.

3.4 Cirrus Global Impact Conclusions

This CATS dataset further elucidates our understanding of cirrus impact on the Earth climate system. By averaging across all times and regions the estimated global annual cirrus radiative effect is 5.78 ± 11.9 Wm^{-2} using the custom habit configuration, or 8.11 ± 10.6 Wm^{-2} using the single bullet rosette parameterization. Global circulation models estimate the Earth-Cloud system as a whole has a net cooling effect on the planet at the top of the atmosphere (Boucher *et al.* 2013). Not accounting for cirrus clouds less than 3.6 COD, Chen *et al.* (2000) estimated the global annual cloud radiative effect to be -34.7 Wm^{-2} using the NASA Goddard Institute for Space Studies (GISS) GCM. Lohmann *et al.* (2008) used the ECHAM5 atmospheric GCM to simulate the climate for five years, and estimated the mean annual global CRF at -25.7 Wm^{-2}.

Another study from Yi *et al.* (2013) estimated the annual global CRF to be -29.6 Wm^{-2} using a ten year run of the National Center for Atmospheric Research (NCAR) Community Atmosphere Model (CAM, version 5.1). Assuming the difference between these estimates and the Chen *et al.* (2000) GISS estimate yields the forcing from cirrus clouds then the ECHAM5 model estimated an annual cirrus RF of 9.0 Wm^{-2}, and the CAM5.1 model 5.1 Wm^{-2} (Table 3.5). However, these global mean estimates using CATS data do not account for latitudes greater than 51° in polar regions. Though this effect is assumed to be relatively small compared to the investigated regions due to low cirrus frequencies observed at higher latitudes of approximately 10% (Sassen *et al.* 2008). Though not accounting for high latitude cirrus potentially causes a low bias in these estimates due to polar night cirrus and high latitude SZAs likely contributing a warming effect.

The annual cirrus RF using the custom habit configuration agreed more with

Table 3.5: Annual Global Cloud Radiative Forcing (Wm^{-2})

Source	All Cloud Forcing	All Cloud (Except Cirrus < 3.6 OD)	Cirrus Forcing
GISS	-	-34.7	-
ECHAM5	-25.7	-	9.0
CAM5.1	-29.6	-	5.1
CATS Modeled Custom Habit	-	-	5.78 ±15.5
CATS Modeled Bullet Rosette	-	-	8.11 ±13.8

the CAM5.1 model, and the RF estimate using only bullet rosettes agreed more with the ECHAM5 model. Interestingly, this also agreed well with the manner these models parameterized ice habit. The CAM5.1 model used a single parameterization developed

by weighting the scattering properties of nine different habits creating a general mean mixed habit. The ECHAM5 model on the other hand was more simple assuming a plate habit for all cirrus at temperatures greater than -35°C, and a spheroidal habit for all cirrus ice below this temperature threshold. By incorporating a more representative cirrus ice habit scattering parameterization the mean global CRF was altered by approximately 40%, or 3.0 Wm^2. This reemphasizes cirrus influence in the climate system, and the importance to better understand their radiative effects.

In this chapter I utilized the unique orbit of the CATS lidar aboard the ISS to analyze diurnal cirrus physical properties and their radiative effects across all seasons. Mean profiles of cirrus IWC and D_{eff} were created on a 3° x 3° lat/long grid between the 51st parallels, which were then incorporated into the RT model, libRadtran, to estimate their radiative forcing at the TOA. Additionally, it was shown using the cirrus physical properties that a different habit parameterization should be used for different seasons and regions rather than using a single assumed habit, which is often practiced. This custom habit parameterization exhibited the potential for cirrus to have a cooling effect, and yielded uncertainty estimates on the order of 100%. Additionally, it was shown the that more realistic habit configuration agreed well with estimates from the GCM that also parameterized ice using a general habit mixture. However, Fig. 3.14 and Fig. 3.15 show that the majority of the warming effect from cirrus clouds is due to their nighttime forcing. Meaning cirrus overall radiative effect is modulated by the daytime forcing, which has been shown to potentially have a cooling effect, and is greatly affected by habit scattering parameterization.

Chapter 4: Mid-Latitude Cirrus Radiative Impacts and Sub-Type Variability Based on Constrained Airborne Lidar Observations (Ozog *et al.* 2019, In Review)

Chapter 3 focused on the global influence of cirrus clouds utilizing the unique CATS cirrus dataset capturing diurnal variability across all seasons. This study showed the benefits of a non-sun synchronous orbit, and helped elucidate the importance of cirrus diurnal variability; not only as it pertains to cirrus physical properties, but also their radiative influence. However, it was discussed that cirrus layers incorporated into the libRadtran RT simulations were mean profiles representative of each grid cell for the associated time of day and season. These mean profiles were derived from all non-attenuating cirrus layers for both day and night observations. While the prior study provided great insight into the diurnal influence of cirrus on the global scale, I theorize to better understand the radiative impact of cirrus clouds each individual observation must be modeled to develop more representative statistics. In this chapter a large dataset of CPL constrained cirrus observations from six field campaigns aboard the ER-2 are investigated to determine their radiative effects.

4.1 CPL Cirrus Retrievals

Six CPL field campaigns from 2012 – 2017, all of which flew on the NASA ER-2, were analyzed based on their prevalence of cirrus clouds, and varying atmospheric conditions in which they formed. As cirrus exhibit different properties depending on their dynamic mechanism of formation (Yorks, 2014), observations were additionally separated into synoptic and convective categories. The campaigns analyzed are listed in table 4.1 and include the Aerosol Characterization from Polarimeter and Lidar (ACEPOL), CALIPSO CATS Airborne Validation Experiment (CCAVE), Polarimeter Definition Experiment (PODEX), Wallops Airborne Vegetation Experiment (WAVE), NASA/NOAA Geostationary Operational Environmental Satellite (GOES) 16 Validation, and Studies of Emissions and Atmospheric Composition, Clouds, and Climate Coupling by Regional Surveys (SEAC4RS). Table 4.1 also lists the season, latitude range, ER-2 origin location, and primary type of cirrus observed for each campaign. Though cirrus may not have been the primary target of each campaign due to their high occurrence frequencies, and high operational altitude of the ER-2, CPL observed a large amount of cirrus during these

Table 4.1. CPL Flight Campaigns

Campaign	Season	Latitude Range	Base Location	Cirrus Type
ACEPOL	SON	30° – 40° N	Palmdale, CA	Synoptic
CCAVE	JJA	35° – 45° N	Palmdale, CA	Synoptic
PODEX	DJF	30° – 40° N	Palmdale, CA	Synoptic
WAVE	SON	35° – 45° N	Wallops Island, VA	Synoptic
GOES	MAM	30° – 40° N	Warner Robins, GA	Convective
SEAC4RS	JJA(S)	20° – 45° N	Houston, TX	Convective

campaigns, which chosen due to their coverage of s wide latitudinal range over varying times of year.

Tens of thousands of cirrus layers were observed by CPL throughout the six campaigns. However, similar to the CATS study in Chapter 3, layers analyzed in this study were further scrutinized to develop the best possible cirrus representation for modeling their radiative properties. Recently, CPL processing algorithms have been updated to mimic CATS processing; producing a L2_lay and L2_prof products with similar lidar ratio, layer discrimination, and cirrus microphysical property retrievals (York *et al.* 2015; Yorks *et al.* 2018). To be considered as a valid cirrus layer four criteria had to be met. Same as for the CATS study, cirrus layers had to have a reported cloud phase score of 8 or higher (scale 0-10), and not be fully attenuating. The SZA nadir to the ER-2 position and time of observation had to be less than 80 degrees. Min *et al.* (2010) showed the shortwave albedo effect rapidly approaches zero at zenith angles greater than 75 degrees. In addition to this, cirrus optical properties had to be constrained using a lidar ratio calculated from the transmission-loss method (Fernald *et al.* 1972; Spinhirne *et al.* 1980). The transmission-loss method retrieves a constrained layer mean lidar ratio by utilizing the difference in the modeled molecular profile above and below the cirrus due to the decreased particulate transmission through the layer. This method requires clear air regions above and below the cirrus layer void of aerosols, which nominally often occur from the vantage point of the ER-2. In total over 20,000 cirrus layers were analyzed. The synoptics observations being composed of 26 individual cirrus clouds, and over 6500 layers. The convective observations from 37 individual cirrus clouds, and over 13,500 layers.

4. 2 CPL Retrieved Cirrus Physical Properties

Table 4.1 lists the 4 campaigns where observed cirrus was associated with synoptic development, and the 2 campaigns where cirrus was primarily associated with convection. These designations where based on season and where the flights took place similar to the CPL cirrus discrimination discussed in Yorks (2014). To verify cirrus type their physical properties were examined. Figure 4.1 shows histograms of cirrus properties for all synoptic (blue curve) and convective (red curve) layers observed. Fig. 4.1a depicts the distribution of layer integrated VDR (Eq. 3.1). Similar to the CATS data, CPL only has depolarization capabilities in the 1064nm channel. This matches well with that shown in Yorks *et al.* (2011; 2014) who found lidar and depolarization ratios were greater in convective cirrus compared to synoptic cirrus, which was conclused using a different CPL cirrus dataset. Additionally, Fig. 4.1c shows convective cirrus had a much higher frequency of clouds above 12 km, while this only occurred 3% of the time in synoptic observations. Cirrus depolarization ratio has a direct correlation with cloud height (Platt *et al.* 2002; Sassen & Benson 2001). Discussed in section 3.2.1 VDR is an indicator of particle aspect ratios in cirrus clouds. Spheroid and bullet rosette shaped ice crystal habits have been found in mid-latitude synoptic cirrus clouds (Lawson *et al.* 2006), which have aspect ratios closer to unity than columns or large irregular aggregate crystals, more often found in cirrus associated with convection (Lawson *et al.* 2010). Examining Fig. 4.1d convective layers exhibit thinner physical thickness than synoptic as they tend to be more composed of tenuous layers blown off of their host anvil or remnants from a dissipated storm. In contrast, synoptic cirrus are more associated with large scale uplift spanning greater regions, and greater physical thickness. While a difference in physical depth is observed, the

distributions of optical depths are more similar (Fig. 4.1e) with a notable difference at the lowest optical depths in Fig. 4.1f depicting histograms for optical depths <0.2 at 0.01 bin size. Additionally, synoptic cirrus observed a small bimodal peak at approximately 0.9 COD likely associated with the thicker stratiform type cirrus that can be associated with

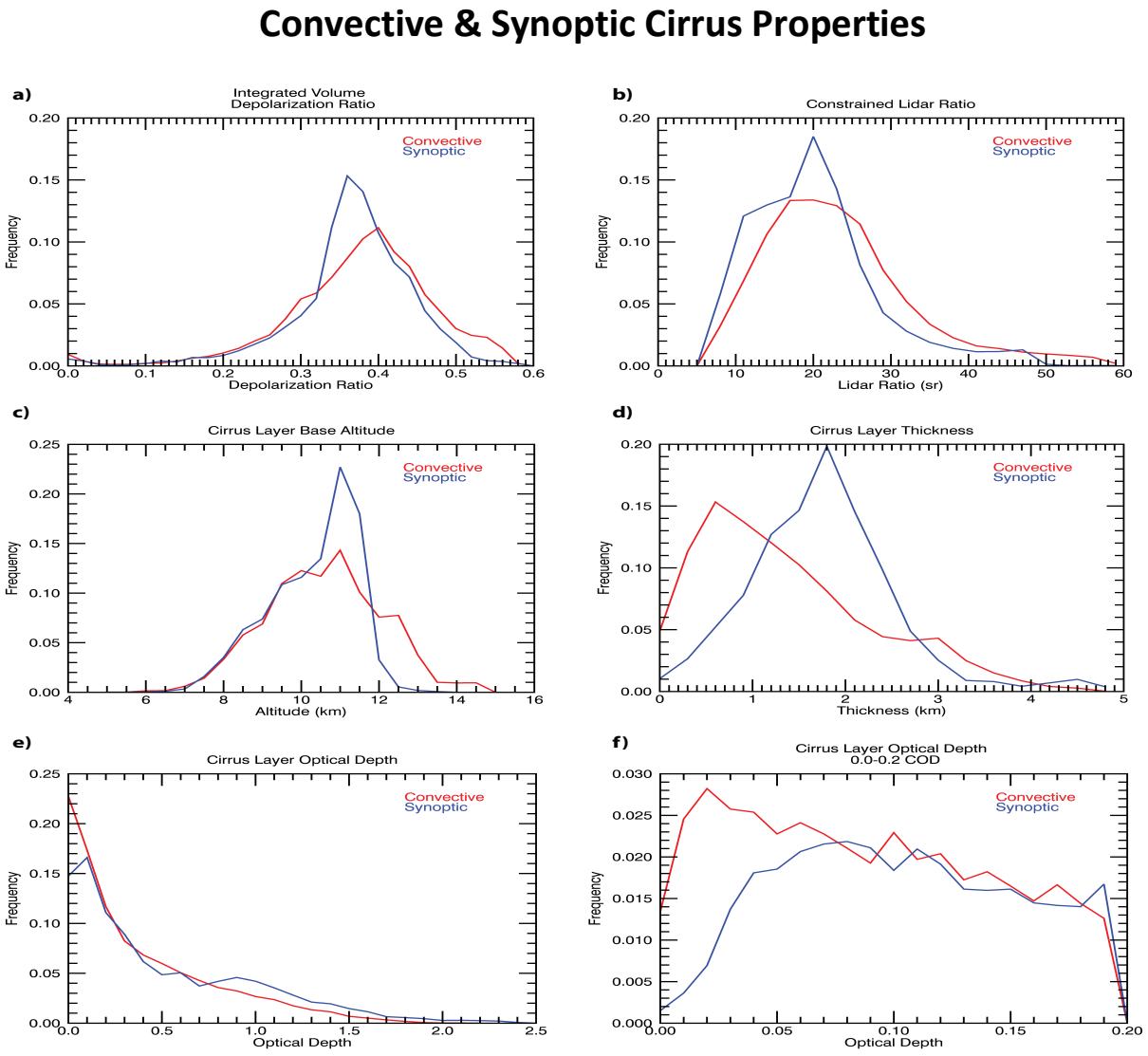

Figure. 4.1. Histograms of cirrus cloud physical and optical properties including (a) integrated VDR, (b) lidar ratio, (c) layer base altitude, (d) layer thickness, (e) layer optical depth binned at 0.1, and (f) layer optical depth for thinnest layers binned at 0.01 intervals for all synoptic and convectively formed layers.

synoptic development. Convective cirrus are more likely to have optical depths <0.05 while few synoptic cirrus were observed below this threshold.

4.3. Radiative Transfer Modeling

All CPL retrieved cirrus profile and layer products were incorporated into the libRadtrdan 1-D RT model to calculate their radiative effects. The configuration of all model runs were similar to those of the CATS study listed in table 3.3. However, instead of a MODIS averaged Lambertian albedo, the bidirectional reflectance distribution function (BRDF) for the associated surface type was used. These BRDFs are provided in the libRadtran model based on the 17 surface types designated in the International Geosphere Biosphere Programme (IGBP; Loveland & Belward, 1997). IGBP surface type is a standard product in the updated CPL processing indexed along the flight track from MERRA-2 reported surface type. Also instead of a single habit parameterization for initial model runs synoptic observations assumed a solid bullet rosette, and convective observations assumed a column aggregate parameterization (Lawson *et al.* 2006; Baker & Lawson 2006; Yorks, 2014). Opting for the smooth habit surface option provided by the Yang *et al.* (2013) parameterizations over roughening assumptions.

Like the CATS study, the atmospheric profiles used in model runs were calculated from the MERRA-2 temperature and pressure profiles reported in the CPL data. MERRA-2 meteorology data is provided at a 3 hour temporal resolution (00, 03, 06 UTC, etc.) for each day available on a global 0.625° longitude 0.50° latitude resolution. For this study instead of using a mean ozone and water vapor profile, ozone and water vapor profiles were indexed from MERRA-2 data along the ER-2 track for each flight and 3-hr interval closest to the time of observation. The last component required by the user to initiate libRadtran

RT simulations is the cirrus layer. CPL cirrus IWC and D_{eff} are calculated identically to the CATS processing described in Chapter 3.

4.3.1 Synoptic Cirrus Radiative Forcing

Cirrus observations from six CPL field campaigns are analyzed for their radiative effect in this study. In addition to the total radiative forcing, Eq. 3.6 can be broken down into its components to compute the SW forcing (CRF_{SW}; Eq. 4.1) and IR forcing (CRF_{IR}; Eq. 4.2) components also discussed in this chapter. These campaigns were chosen due to the varying regions and times of year to develop a robust dataset of cirrus representing the diverse conditions they form in. ACEPOL, PODEX, WAVE, and CCAVE encompass the cirrus observations associated with synoptic conditions. PODEX took place in the wintertime while both ACEPOL and WAVE took place in autumnal months. Though CCAVE flew in August, the ER-2 flights were over the desert southwest and Pacific coast where convection was largely absent. Inherently, discriminating mid-latitude cirrus by formation mechanism results in a seasonal dependence. The boreal winter (DJF) is characteristic of decreased convective activity, and increased synoptic influence with a stronger Hadley circulation and associated jet stream dynamics (Korty & Schneider 2008). As mentioned prior, the convective and synoptic observation were represented in the model with different scattering parameterizations. An irregular column aggregate habit for convective cirrus, and bullet rosette habit for synoptic cirrus. Section 4.4 will further

$$CRF_{SW} = [(SW_{\downarrow}) - (SW_{\uparrow})]_{Cloudy} - [(SW_{\downarrow}) - (SW_{\uparrow})]_{Clear} \qquad \text{Eq. 4.1}$$

$$CRF_{IR} = [(IR_{\downarrow}) - (IR_{\uparrow})]_{Cloudy} - [(IR_{\downarrow}) - (IR_{\uparrow})]_{Clear} \qquad \text{Eq. 4.2}$$

discuss uncertainties induced from these differences in crystal habit, similar to the CATS study.

Figure 4.2 displays box and whisker plot statistics for all campaigns TOA total net radiative forcing, and table 4.2 features their mean, median, and standard deviation statistics. The total CRF in black font, with the IR and SW forcing components in red and blue, respectively. As shown in Eq. 3.6 each total forcing value is the sum of the IR and SW forcing components. The synoptic cirrus, in the first four rows of table 4.2, all exhibited a general warming effect. PODEX had the warmest mean and median total radiative effect. Additionally, PODEX had the warmest observed single CRF and also was the only synoptic campaign without an observed minimum cooling CRF value. PODEX was the only campaign to take place in the wintertime, and had the coldest average cloud top temperatures (-64° C) of the synoptic campaigns. Note that the minimum ACEPOL (SON) total CRF value had a very low negative magnitude of just -0.14 Wm^{-2}. The PODEX

Table 4.2. Campaign Cirrus Radiative Forcing Component Statistics (Wm^{-2})

Campaign	Mean			Median			Std Dev		
	Total	IR	SW	Total	IR	SW	Total	IR	SW
ACEPOL	24.3	54.1	-29.9	22.0	58.6	-24.1	13.7	32.6	26.4
CCAVE	11.9	37.1	-25.2	10.0	32.6	-24.7	14.6	25.2	16.5
PODEX	33.7	52.7	-15.8	30.3	45.7	-9.91	18.8	35.5	18.5
WAVE	25.7	89.9	-64.3	27.4	88.9	-62.8	15.4	16.5	16.0
GOES	-2.95	45.2	-48.3	-4.60	44.8	-44.4	11.6	25.6	26.8
SEAC4RS	-4.86	38.2	-43.2	-3.97	30.7	-33.2	13.1	29.8	33.0
Synoptic	26.0	55.3	-27.7	23.3	51.2	-21.5	19.2	34.8	25.3
Convective	-4.42	39.8	-44.4	-4.12	34.4	-35.9	12.7	29.0	31.7
All	5.65	45.0	-38.8	2.29	39.4	-31.9	20.9	31.9	30.8

campaign also observed the greatest standard deviation of values at 33.65 ± 18.83 Wm^{-2}. CCAVE, which was the only summertime synoptic campaign, observed the lowest mean positive total forcing of 11.89 ± 14.64 Wm^{-2}, and was also the only the synoptic campaign where the one sigma range incorporated negative forcing. The CCAVE mean total forcing was 64%, 53%, and 51% lower than PODEX, WAVE, and ACEPOL, respectively. The WAVE, PODEX, and ACEPOL campaigns all had lower quartile total CRF values between 5 – 10 Wm^{-2}, and CCAVE had a lower quartile total CRF slightly lower at 3.32 Wm^{-2}. The contrast of CCAVE with the other synoptic campaigns is likely due it being the only summertime synoptic campaign, which had the warmest average cloud top temperatures (-49° C), causing greater outgoing IR flux at the TOA (Kato *et al.* 2011).

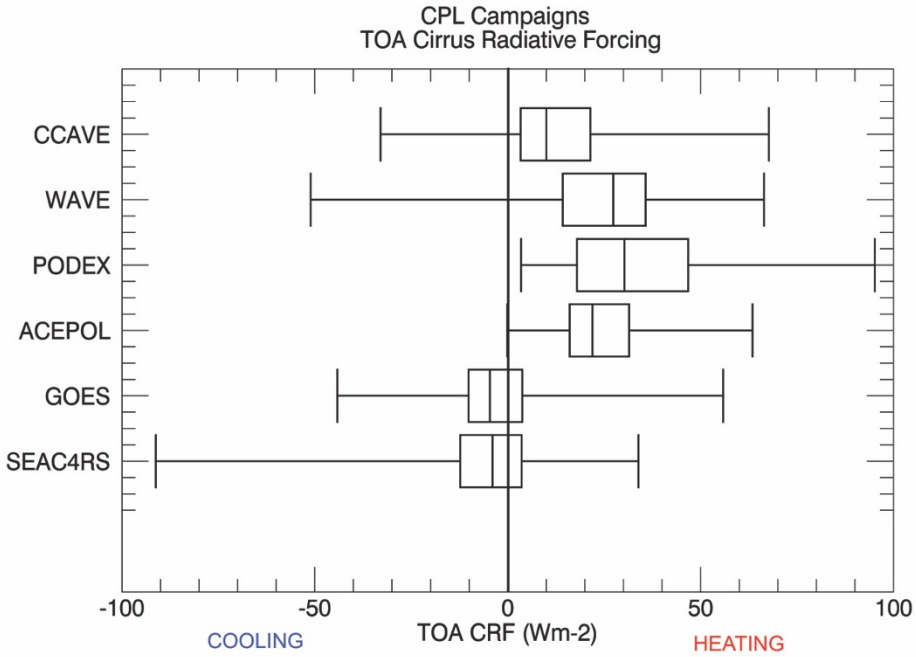

Figure 4.2. Box and whisker statistical plots for all CPL campaigns total TOA cloud radiative forcing

Figure 4.3 displays the histograms for each campaign total, IR, and SW radiative forcing components represented by the black, red, and blue curves, respectively. Discussed

in Chapter 1, cirrus are unique and important because they are relatively transmissive to incoming solar SW radiation while also efficiently absorb terrestrial IR radiation preventing it from escaping the Earth – Climate system at the TOA. Though cirrus are relatively transmissive to solar radiation their albedo effect still often results in a SW cooling effect observed in approximately 90% of synoptic observations. The other 10%

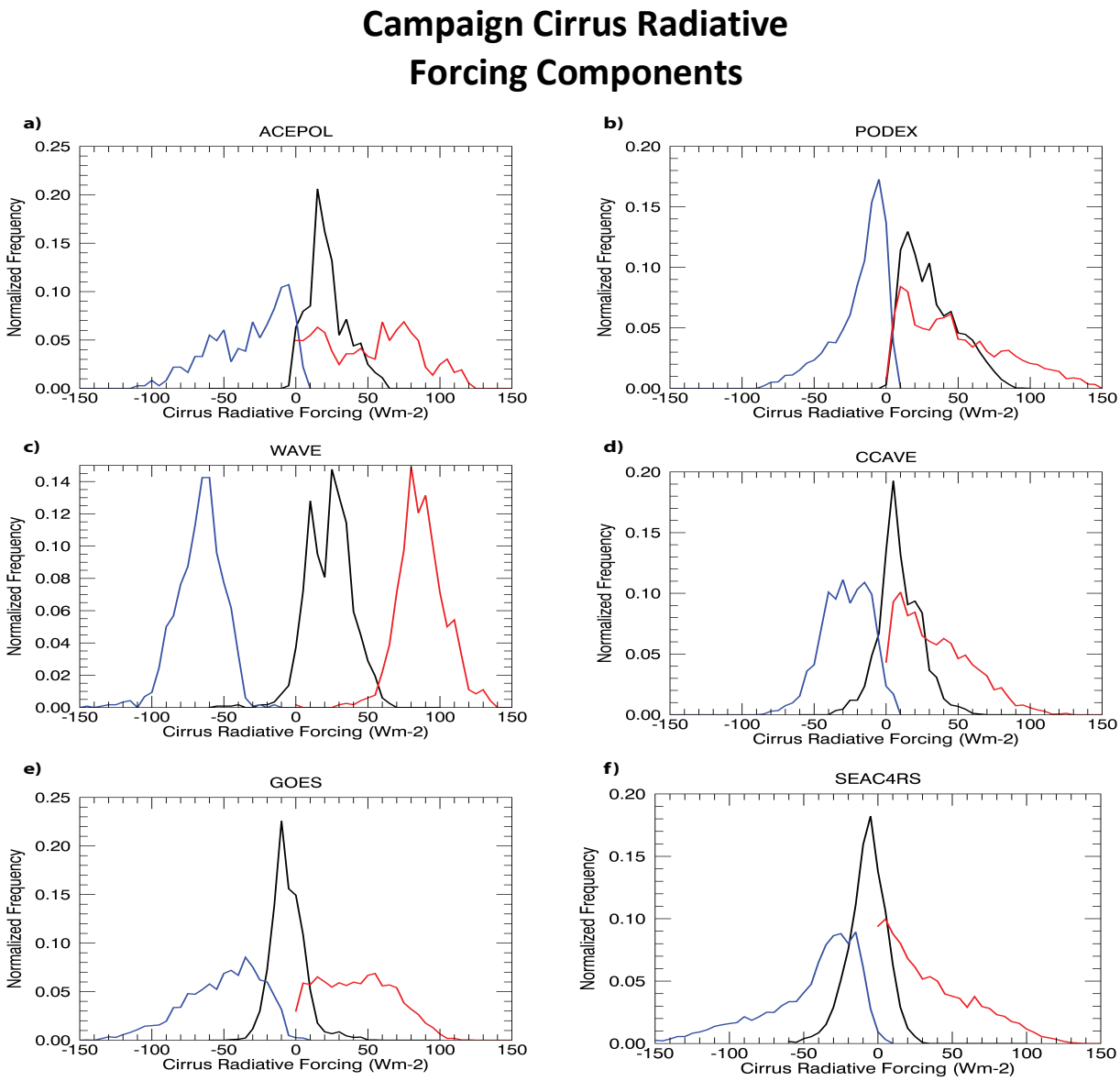

Figure 4.3. Histograms of Total (black), IR (red), and SW (blue) CRF for (a) ACEPOL, (b) PODEX, (c) WAVE, (d) CCAVE, (e) GOES, and (f) SEAC4RS campaigns at a bin size of 5 Wm^{-2}.

have a relatively weak SW warming effect no greater than 10 Wm^{-2}, occurring at the highest solar zenith angles. Conversely, the IR effect is positive for all synoptic observations. These trends are depicted in Fig. 4.3a – d with the SW forcing histograms (blue curve) peaked in the negative region, and the IR forcing histograms (red curve) peaked in the positive region. Fig. 4.3a – d represent all synoptic campaigns, with 4.3e & 4.3f the convective campaigns discussed in the following section. The peak of the total forcing histograms (black curve) for the synoptic campaigns all occur in the warming region agreeing well with the mean and median total CRF values in table 4.2. It is interesting to note that in Fig. 4.3c there is little overlap between the IR (red) and SW (blue) forcing histograms with the total (black) forcing histograms. The WAVE campaign was the only synoptic campaign that took place over the eastern United States as opposed to being based out of Palmdale, CA in the Southwest.

Many studies utilizing satellite data have investigated the influence of layer optical properties on cirrus radiative forcing, primarily cloud optical depth (Choi *et al.* 2005; Choi *et al.* 2006; Min *et al.* 2010). However, this study represents the first known attempt to study cirrus radiative effects from a large dataset exclusively using constrained lidar retrievals of cloud optical properties. Figure 4.4 shows the influence of COD on each radiative forcing component with probability density functions (PDF). The radiative forcing effect in Wm^{-2} is on the x-axis, and COD (unitless) is on the y-axis for each plot. PDF plots for synoptic cirrus are shown in Fig. 4.4(a) – (c) on the left column, with the SW, IR, and total CRF components in the top (Fig. 4a), middle (Fig. 4b), and bottom (Fig. 4c), respectively. Sassen & Cho (1992) showed that thin cirrus with a COD < 0.3 occur most frequently compared to larger optical depths (Stubenrauch *et al.* 2013). Thin cirrus

contribute to 42.5% of all synoptic observations, which is seen in Fig. 4.4(a) – (c) with the greatest clustering of points in the thin cirrus regime below 0.3 COD. Though observations exhibit a clustering at low optical depths clear trend lines can be seen between each radiative forcing component and optical depth. The synoptic SW forcing in Fig. 4.4a shows

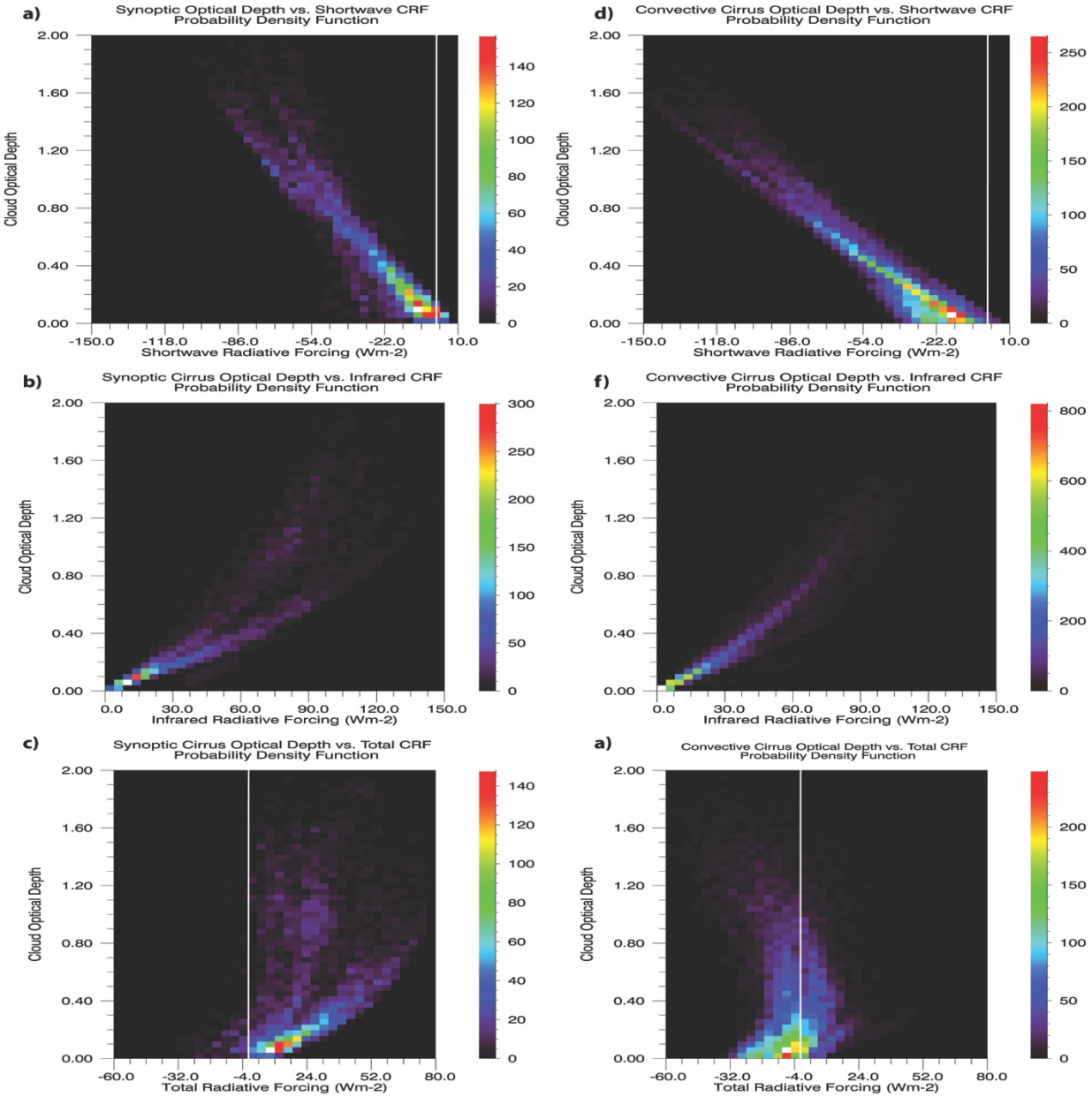

Figure 4.4. Probability density functions of cloud optical depth versus radiative forcing components. Plots a, b, and c show synoptic SW, IR, and total forcing, respectively. Plots d, e, and f show convective SW, IR, and total forcing, respectively. Zero forcing marked by white line.

a linear dependence of the albedo effect becoming increasingly negative at higher optical depths. The slope of the PDF in Fig. 4.4a shows SW CRF decreases by -47.1 Wm^{-2} per 1.0 optical depth in synoptic cirrus. The PDF in Fig. 4b shows the IR forcing dependence on optical depth is not linear, like the SW forcing, but rather more logarithmic. A rapid increase in IR forcing with increased optical depth is observed at optical depths less than 1.0, and then the curve levels off between COD 1.0 – 2.0 with an asymptote like quality. While cirrus layers with an optical depth less than 2.0 make up of 99% of this dataset, this trend in the IR forcing dependence on COD was also observed in Choi *et al.* (2005; 2006). A best fit line in Fig. 4b shows a maximum synoptic IR cloud forcing of 109.3 Wm^{-2} at an optical depth of 1.70. The synoptic cirrus total forcing PDF is shown in Fig. 4.4c. The total forcing shows a nonlinear dependence on COD, like the IR forcing. However, unlike the IR effect, which appears to monotonically increases with COD, the total forcing follows a parabolic trajectory where total CRF increases to a given optical depth. The best fit line for Fig. 4.4c has a maximum total CRF of 38.5 Wm^{-2} at an optical depth of 1.18. All synoptic cirrus CRF components show a significant correlation with optical depth. These trends show that, for a given cirrus layer, there is a critical optical depth where IR warming reaches its maximum potential, however, SW cooling continues to increase in magnitude with increasing optical depth. This results in the parabolic trajectory of total CRF increasing with COD until the SW albedo effect becomes stronger than the IR greenhouse effect at a critical optical depth. At optical depths greater than this the total CRF decreases in magnitude to a point where there is a sign change, and cirrus have a cooling effect at COD > 2.57.

Figure 4.5 depicts PDFs of the synoptic radiative forcing components and constrained lidar ratio used to calculate the cirrus optical and microphysical properties. Lidar ratio is an important variable in the forward inversion of the lidar equation. The PDFs in Fig. 4.5 further separate the SW, IR, and total forcing into thin (COD < 0.3) and opaque cirrus (COD > 3.0) regimes as defined by Sassen & Cho (1992). Note that opaque here does not mean fully attenuating to the CPL signal, but rather the nomenclature adopted from Sassen & Cho (1992) for this given cirrus optical depth range often used in cirrus studies. The top, middle, and bottom rows depict the SW, IR, and total radiative forcing, respectively, as in Fig. 4.4, while the left column (Fig. 4.5a – c) represents the thin cirrus and the right column (Fig. 4.5d – f) the opaque cirrus. The particulate lidar ratio (S_p; Eq. 1.4) is equivalent to the inverse single scattering albedo that has been multiplied by the 180° phase function (P_{11}). This can be interpreted as cirrus layers with a higher lidar ratio either having a larger cloud optical depth (greater numerator) or less backscatter (smaller denominator) compared to those with a lower lidar ratio. The synoptic cirrus PDFs in Fig. 4.5 exhibit relatively little spread, and considerably less in the thin COD regime. Lawson *et al.* (2006) showed that the majority of particles in mid-latitude synoptic clouds are relatively small (<100 μm), and greater concentrations of smaller particles have been shown to increase albedo (Morrison and Grabowski 2011), which effectively reduces the lidar ratio. As shown in Fig. 4.1b and Yorks (2014) lower lidar ratios are observed in synoptic cirrus. Meaning a greater cooling SW albedo effect at lower lidar ratios for a given optical. Fig. 4.4a shows thin cirrus lidar ratios centered at approximately 14 sr, and the

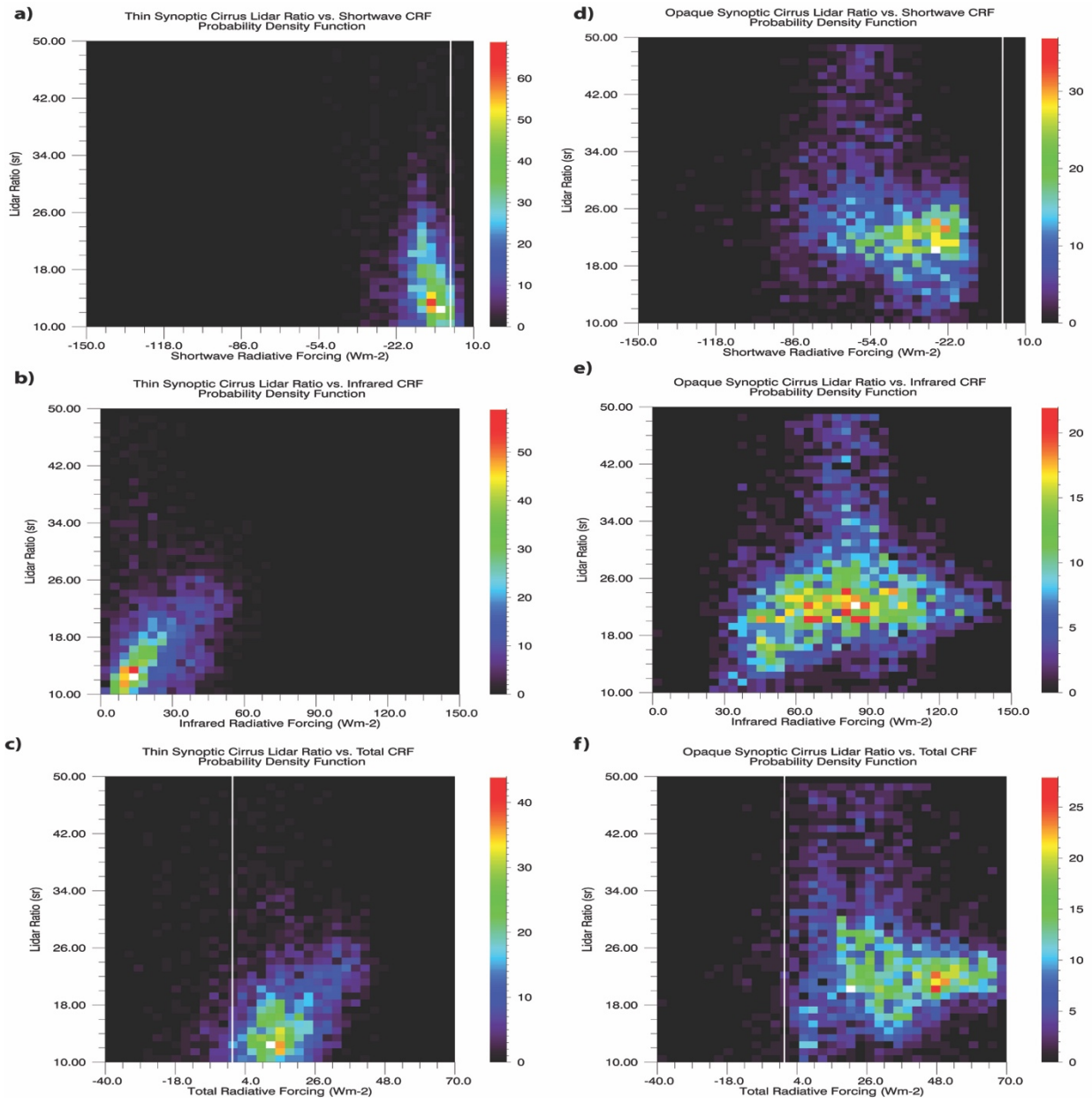

Figure 4.5. Probability density functions of synoptic cirrus constrained lidar ratio versus radiative forcing components. Plots a, b, and c show synoptic SW, IR, and total forcing, respectively, for thin cirrus. Plots d, e, and f show convective SW, IR, and total forcing, respectively, for opaque cirrus. Zero forcing marked by white line.

opaque center at approximately 22 sr. The magnitude of both the negative SW albedo effect, and the positive IR greenhouse effect are directly correlated with COD and lidar ratio. With a greater IR forcing showing synoptic cirrus have greater total net warming at greater optical depths and lidar ratios.

As in the CATS study, to better understand the radiative significance of cirrus on climate, modeled forcing must be weighted by cirrus temporal and spatial extent (Berry & Mace 2014). In this chapter will be referred to as the effective CRF. CPL airborne campaigns are conducted with explicit science objectives where their flight paths are created to target certain atmospheric phenomena. This results in a high bias in the ratio of cirrus layers observed to all CPL observations in the flights analyzed. To determine cirrus frequency a year of daytime data from the CATS lidar during 2016 was analyzed. The CATS lidar was chosen over the CALIPO satellite lidar as it provides better diurnal coverage of the mid-latitude and tropical regions due to the unique 51° inclination orbit of the ISS. The 2016 CATS frequencies were separated into seasonal components DJF, MAM, JJA, and SON. Additionally, seasonal frequencies were separated into the same thin (COD < 0.3) and opaque (0.3 < COD < 3.0) optical depths discussed above. The CATS laser becomes fully attenuated at approximately optical depth 3.0, similar to the CPL laser, so the CATS dataset excludes all fully attenuating ice clouds to best compare to the CPL dataset which consists only of constrained layers. Figure 4.6 shows the CATS 2016 global cirrus frequencies on a 3° x 3° latitude/longitude grid. The left column Fig. 4.6a – d shows thin cirrus frequency for DJF, MAM, JJA, and SON, respectively, and opaque cirrus on the right column Fig. 4.6e – h. Frequencies were determined by the ratio of cirrus observations in its respective COD range to the total number of CATS observations in the respective grid cell. The CPL dataset had observations in each season and spanned 20° – 45° N. Looking at this latitude band the cirrus occurrence frequencies for each season and COD range are listed in table 4.3. Thin cirrus occur more frequently compared to opaque layers with a maximum in the spring of 18.1%, and minimum in the autumn of 14.3%.

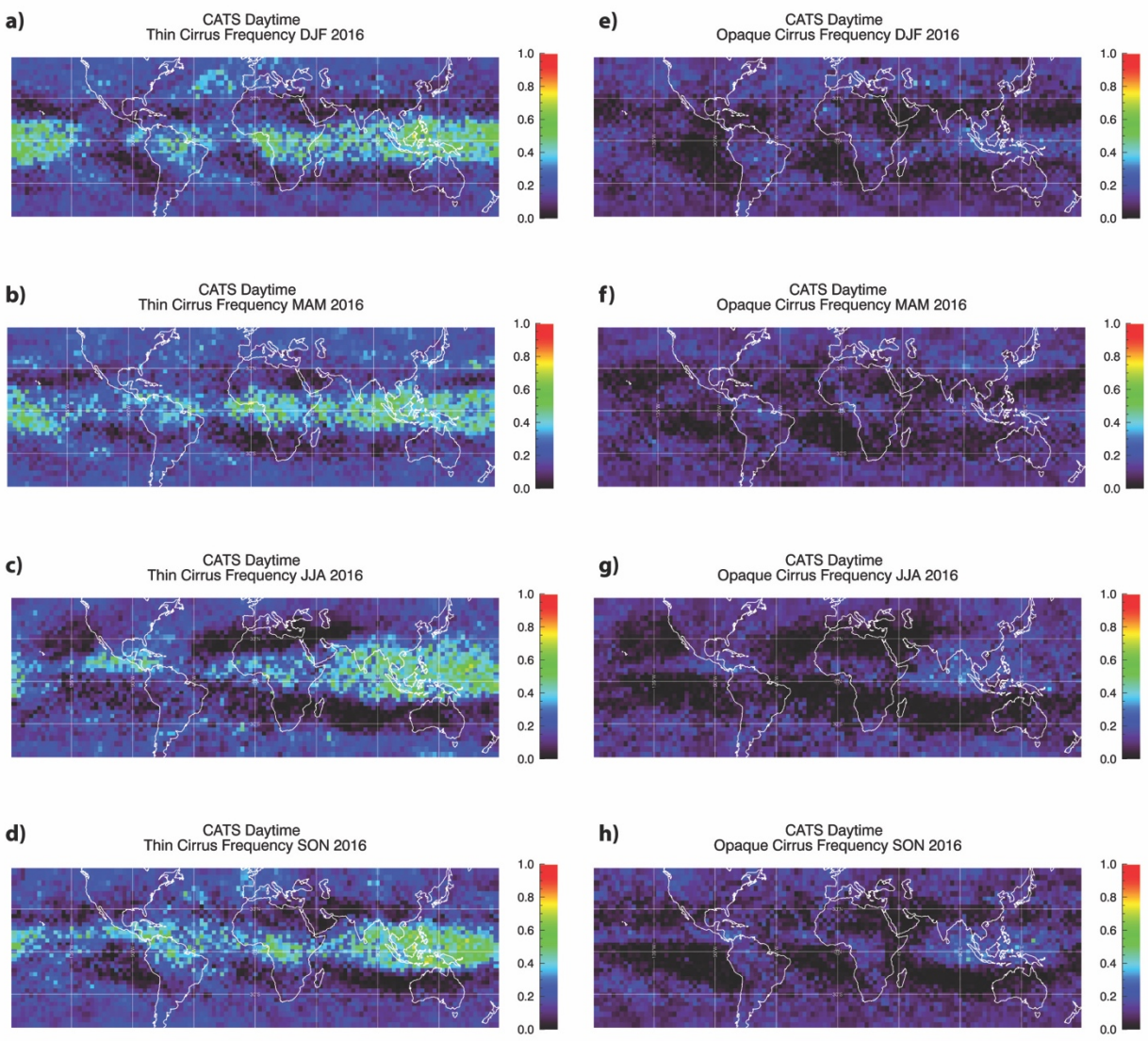

Figure 4.6. CATS gridded 2016 daytime cirrus frequency for layers with COD < 0.3 in DJF (a), MAM (b), JJA (c), and SON (d), and layers with COD between 0.3 – 3.0 during DJF (e), MAM (f), JJA (g), and SON (h).

Opaque cirrus exhibit less seasonal dependence with approximately 11% frequency in the winter and spring, and 8% frequency in the summer and fall. By weighting the total radiative forcing effects in table 4.2 by their spatial and temporal frequency a better understanding of cirrus impact on the climate system can be drawn.

Table 4.3. CATS 2016 Mid-Latitude Daytime Cirrus Frequency		
Season	Mid-Lat Thin Cirrus Frequency	Mid-Lat Opaque Cirrus Frequency
DJF	15.7 %	10.8 %
MAM	18.1 %	10.9 %
JJA	15.0 %	8.0 %
SON	14.3 %	8.5 %

Due to the prevalence of thin cirrus in the mid-latitudes they have a more weighted impact compared to opaque cirrus. Thin synoptic cirrus have an effective CRF of 3.55 ±1.92 Wm^{-2} compared to opaque synoptic cirrus effective CRF of 3.07 ±2.29 Wm^{-2}. Overall the mean synoptic cirrus effective total forcing is 3.31 ±2.13 Wm^{-2}.

4.3.2 Convective Cirrus Radiative Forcing

The SEAC4RS and GOES campaign observed primarily cirrus associated with the anvil outflow of convective thunderstorm systems. SEAC4RS took place in JJA, extending in September, where the ER-2 flew over convective cells in the Gulf of Mexico and the United States mainland. In the GOES campaign the ER-2 was based out of Georgia in late April and May where it largely flew over springtime linear convective systems. Figure 4.2 boxplots show that the convective cirrus exhibit a stronger cooling total CRF compared to the synoptic cirrus. The median and maximum total CRF for both convective campaigns are significantly lower than the respective median and maximum total CRF for the synoptic campaigns. SEAC4RS and GOES both observed a mean negative total CRF, and also relatively less spread represented by the lower standard deviations at -4.86 ± 13.08 and -2.95 ± 11.57 Wm^{-2}, respectively. The convective campaigns had a strong mean negative SW forcing of -44.4 Wm^{-2}, and weaker mean positive IR forcing of 39.8 Wm^{-2} leading the convective cirrus to exhibit a net cooling. Though Fig. 4.2 and Fig. 4.3 both show that the

convective cirrus have a warming effect at times, the mean of all warming observations is 8.16 ±7.04 Wm^{-2}, weaker than the mean of all cooling observations at -11.4 ±9.48 Wm^{-2}. With the majority of convective observations (64.3%) having a cooling effect. The greater incoming solar radiation at the lower SZAs in the warmer seasons SEAC4RS and GOES took place corresponds to a greater albedo effect (Hong *et al.* 2016). However, as discussed in Chapter 3, it is also likely that the column aggregate habit parameterization effectively scatters more SW radiation than bullet rosettes.

The convective cirrus PDFs in Fig. 4.4d – f, shown in the previous section, show the relation of CRF versus optical depth. All the PDFs here exhibit a clustering in the thin cirrus regime as approximately 52% of convective layers had a cloud optical depth < 0.3. Fig. 4.4d shows the convective cirrus SW forcing decreases at a rate -76.4 Wm^{-2} per 1.0 COD. This is a 65% greater rate than observed in Fig. 4.4a for the synoptic SW forcing dependence on optical depth. The convective IR forcing in Fig. 4.4e has the same logarithmic pattern observed in the synoptic IR effect, but is slightly weaker with the best fit line having a maximum of 103.8 Wm^{-2} at a COD of 1.89. The convective density plot for the total forcing versus optical depth is shown if Fig. 4.4f. Here a line of best fit showed a maximum forcing of -1.82 Wm^{-2} occurring at a relatively low optical depth value of 0.56. The maximum single total CRF observed in the convective observations was 55.8 Wm^{-2} where the cirrus layer had a 0.34 optical depth. With the IR CRF effect being relatively similar in magnitude between both cirrus types the SW forcing effect is the dominant force in determining the differences seen between the synoptic and convective total CRF.

Fig. 4.7a – c represent PDFs of lidar ratio versus CRF for thin and opaque convective cirrus, respectively. The convective cirrus exhibit more spread in the lidar ratio

distribution across all forcing values in both optical depth regimes compared to the synoptic cirrus. Referring back to Eq. 1.4 the lidar ratio is inversely proportional to backscatter. Since a larger range of larger particle sizes are observed in convective cirrus (100 – 400 μm; Lawson *et al.* 2006), they effectively backscatter less following the principle laid out for synoptic cirrus. This yields higher lidar ratios across a greater range of values in the convective cirrus. In contrast with synoptic cirrus in Fig. 4.5, the PDFs for the convective cirrus radiative components in Fig. 4.7 exhibit less correlation with lidar ratio. The lidar ratios range from 10 – 60 sr in both thin and opaque optical depth regimes. The PDFs for thin total convective CRF in Fig. 4.7c is centered on the x-axis at approximately -2.0 Wm^{-2}, and for opaque cirrus centered at a more negative total forcing of approximately -7.0 Wm^{-2} (Fig. 4.7f). The PDF in Fig. 4.7f also shows a higher density of lidar ratios at approximately 22 sr compared to the thin convective cirrus which have clustering primarily below lidar ratios of 20 sr (Fig. 4.7d). The convective cirrus lidar ratios have a weak inverse relationship with total CRF while synoptic cirrus, in contrast, exhibited a stronger direct correlation. This is likely due to that higher lidar ratios are associated with greater COD, and Fig. 4.4f shows that the cooling effect for convective cirrus begins at a significantly lower COD compared to synoptic cirrus (Fig. 4.4c).

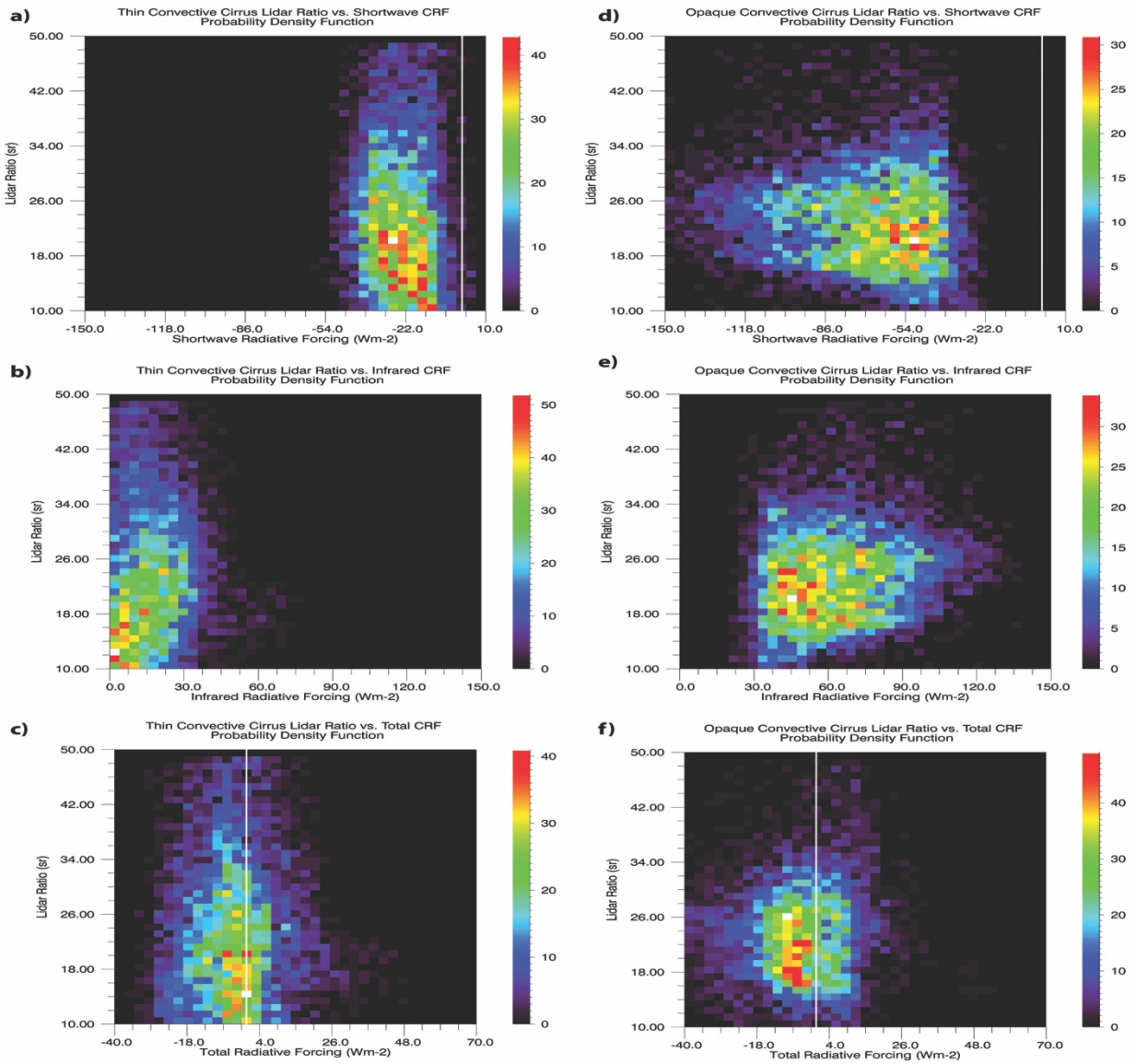

Figure 4.7. Probability density functions of convective cirrus constrained lidar ratio versus radiative forcing components. Plots a, b, and c show synoptic SW, IR, and total forcing, respectively, for thin cirrus. Plots d, e, and f show convective SW, IR, and total forcing, respectively, for opaque cirrus. Zero forcing marked by white line.

The effective CRF for the convective cirrus is estimated by weighting the CRF values in table 4.2 by the retrieved mid-latitude frequencies in table 4.3; same as for the synoptic cirrus. This reduced the absolute net cooling observed in convective cirrus from -4.42 Wm^{-2} to an effective CRF estimate of -.66 ±2.07 Wm^{-2} for thin cirrus, and -0.35

±1.07 Wm^{-2} for opaque cirrus. The overall mean effective radiative forcing for all convective cirrus observations is -0.51 ±1.67 Wm^{-2}.

When averaging across both the synoptic and convective datasets the mean total forcing by all cirrus is 5.65 ±20.9 Wm^{-2} with a median of 2.29 Wm^{-2} from Table 4.2. Accounting for seasonal frequencies, the annual mean daytime northern mid-latitude radiative forcing can be estimate similar to section 3.4. The annual mean daytime northern mid-latitude CRF is 0.95 ±2.63 Wm^{-2}. However, when scrutinizing cirrus observations more closely by formation mechanism it becomes more complex then this generality. Cirrus are observed to have greater potential for a significant cooling effect when associated with convection. The inherent seasonal differences between the synoptic and convective datasets agree well with the findings Hong *et al.* (2016), which analyzed a year of CALIPO and CloudSat data and found a negative summertime cirrus total CRF, and positive wintertime effect in the mid-latitudes. However, this is contrasted by the CATS study which observed a warming effect in JJA and a cooling effect DJF. It should be noted that the Hong *et al.* (2016) study included liquid water clouds and used a different roughened aggregate habit parameterization (Yang *et al.* 2000; 2005), and also a lower resolution two-stream model for its simulations which all induce inherent differences in results.

4.4 Uncertainty Analysis

Similar to the CATS study, uncertainties are represented here as the difference in the model radiative forcing from varying the crystal habit parameterization. All CPL cirrus observations were run in the libRadtran model with both the column aggregate and the solid bullet rosette parameterization to investigate the resultant uncertainty. Figure 4.8 shows histograms for the total radiative forcing; synoptic cirrus on the left in Fig. 4.8a and convective clouds on the right in Fig. 4.8b. Modeled results incorporating bullet rosettes are shown by the red curves, and aggregates by the blue curves. The red curve in Fig. 4.8a depicting bullet rosette synoptic cirrus represents the values for all prior discussion of synoptic cirrus in this chapter. Likewise, the blue curve in Fig. 4.8b for all connective cirrus discussed. These figures show the large potential uncertainty in modeled cirrus radiative forcing from an assumed crystal habit parameterization without in-situ observations.

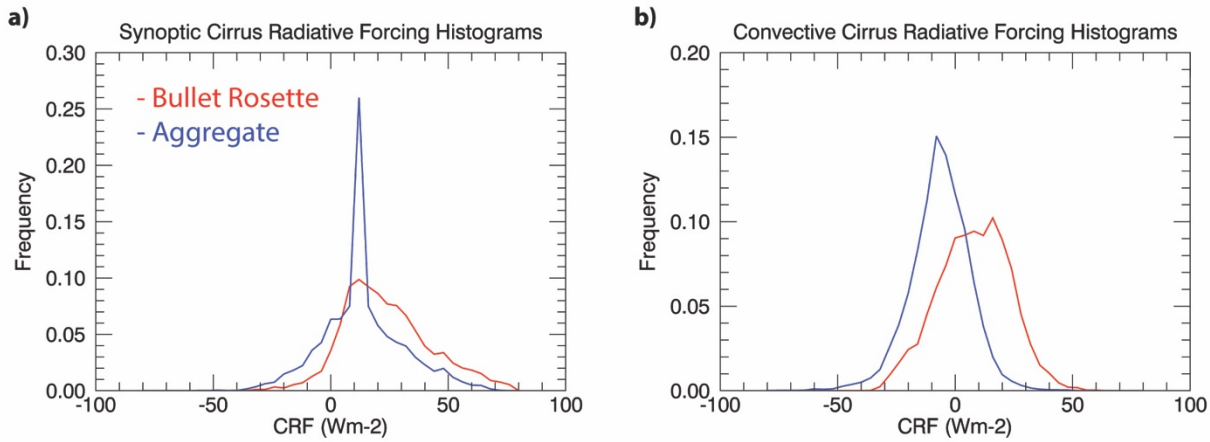

Figure 4.8. Histograms of synoptic (a) and convective (b) cirrus total cloud radiative forcing with bullet rosette habit parameterizations (red) and aggregate parameterizations (blue).

The peak for both the bullet rosette and aggregate habits in synoptic cirrus remained the same at approximately 10 Wm^{-2}. Though this value was 15% more common with the aggregate crystal shape indicated by the difference in peak height in 4.8a. However, the

aggregate parameterization yielded less observations above this peak than the bullet rosette parameterization, and also had cooling values three times more often than the bullet rosette parameterization. Approximately 15% of synoptic cirrus observed a net cooling with aggregates compared to 5% with bullet rosettes. This resulted in the mean radiative forcing for synoptic cirrus being 40% lower at 15.35 ±19.0 Wm^{-2} with the aggregate parameterization, and a median 45% lower at 12.77 Wm^{-2} compared to the respective values in table 4.2.

The observed differences are more significant for the convective cirrus layers. Fig. 4.8b shows the peak total CRF in the warming region with a bullet rosette parameterization compared to the peak for the aggregate crystal habit peaked in the cooling region. The mean convective cirrus total CRF shown in table 4.2 is -4.42 Wm^{-2} compared to model runs with the bullet rosette habit a factor of three greater at a mean 9.94 ±15.1 Wm^{-2} CRF. Convective cirrus with bullet rosettes observed a net warming 74% of the time; twice more often than when modeled with the aggregate parameterization. This is an important result as it shows the chosen cirrus ice habit parameterization in models can potentially lead to large uncertainties in the magnitude of calculated forcing or even potential sign changes.

Figure 4.9 depicts uncertainty histograms for the synoptic and convective observations in the blue and red curves, respectively, and the combined all observations by the black curve. Overall the whole dataset exhibited a median uncertainty of 90%, which is comparable to the global daytime forcing uncertainty estimated in Chapter 3. I reiterate here that the CPL dataset is comprised only of daytime observations due to the lack of nighttime observations obtained during campaigns. The synoptic cirrus have a much smaller uncertainty of 30.9% compared to the convective uncertainty of 147% due to the habit change. As differences in scattering properties primarily affect the SW forcing component it is likely that the reduced uncertainty observed in synoptic cirrus is due to reduced solar radiation. While there was overlap in the latitude ranges of each campaign the synoptic campaigns primarily took place in the boreal winter or fall with increased solar zenith angles. Additionally, the SEAC4RS campaign included flights farther south than all

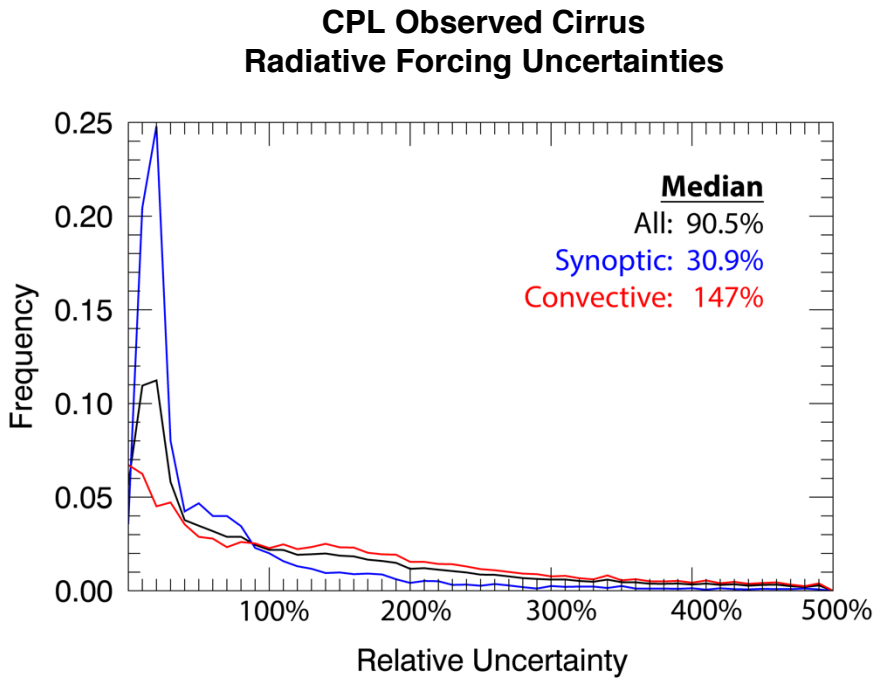

Figure 4.9 Uncertainty histograms from habit scattering differences for synoptic, convective, and combined all observations in the blue, red, and black curves, respectively.

other campaigns decreasing the SZA associated with convective observations. Since the aggregate habit has been shown to scatter more SW radiation, this albedo effect is more pronounced when solar insolation is greater. The convective cirrus were modeled with a mean SZA of 38°, and the synoptic observations had a mean SZA of 56°. This is in agreement with uncertainties observed in Chapter 3 being larger in the tropics, and respective mid-latitude summers, when SZA is lower.

In this chapter I analyzed an expansive dataset of over 20,000 cirrus observations from the airborne CPL instrument. These were used to model individual cirrus layers in contrast to mean profiles, like those in Chapter 3. Observations were separated into cirrus developed through convective forcing and synoptic forcing, and their modeled crystal habit parameterization were chosen to best represent their sub-type. Synoptic cirrus exhibited a greater warming effect than convective cirrus peaking at a COD of approximately 2.5, while convective cirrus was considerably lower around 0.5 COD. Showing that the aggregate like crystals, which are more likely to occur in convective cirrus, effectively scatter more incoming SW radiation resulting in a cooling effect at lower optical depths compared to synoptic. After normalizing absolute radiative forcing for frequency the magnitude of estimated mean annual daytime cirrus CRF for the mid-latitudes was 0.95 Wm^{-2}. Assuming frequencies and observations are representative of the Northern Hemisphere mid-latitudes this estimate was approximately equivalent to that estimate in the Chapter 3 using only bullet rosette habits. Though it was discussed that the CPL observations spanned a wider range of SZAs, which have been shown to be a key component in determining both CRF magnitude and sign. Furthermore, forcing

uncertainties for synoptic cirrus were on the order of 30% compared to 150% for convective cirrus.

Chapter 5: Future Work

The updated ACATS system with the new calibration configuration integrated into the receiver sub-system proved to provide consistent and reliable etalon calibration. This is a crucial first step in retrieving ACATS HSRL and Doppler wind retrievals. The new calibration technique consistently provided accurate etalon defect values leading to the reliable separation of the Rayleigh and particulate signal. However, HSRL optical properties and LOS Doppler wind retrievals exhibited large uncertainties within cirrus layers during ground based zenith pointing operations. Though the Rayleigh signal was consistently distinguished from the particulate signal in cirrus clouds during testing, retrieval of the ARB was not to the accuracy required for reliable retrievals of HSRL optical properties.

Future work with ACATS involves testing etalon calibration from the ER-2 during airborne science campaigns. From this platform ACATS has several advantages over ground based operations. A reduced range to target when observing cirrus clouds allows for less signal attenuation through the atmosphere, therefore resulting in a stronger Rayleigh signal to be retrieved through the ACATS etalon. In addition to range benefits, the lower atmospheric density and absence of a PBL aerosol layer observed below the ER-2 during flight also lends itself to little signal attenuation before reaching cirrus layers, thus allowing for a more robust signal to measure both the particulate and Rayleigh signal components at altitude.

Another benefit from the absence of PBL interference is accurate calibration of the signal to the atmospheric Rayleigh profile calculated from the temperature, pressure, and water vapor profiles. As shown in Yorks (2014) ACATS standard

operations concurrently act as a reliable standard backscatter lidar by integrating the signal across all 24 channels to mimic a single 532nm channel. Shown in Eq. 1.1 the ATB is retrieved by using a calibration fit to the atmospheric molecular signal. ACATS testing has not been optimized for ground based operations to account for low level aerosols in the near field signal, as well as system overlap. The cirrus observations discussed in Chapter 2 are beyond the range of where the system overlap function comes into unity. Yorks (2014) developed HSRL optical property algorithms that initially rely on accurate retrievals of ARB. However, the ATB is simply the sum of the APB and ARB signals, and Yorks (2014) showed that ACATS ATB retrievals of cirrus using the standard lidar method were comparable to coincident CPL retrieved ATB measurements. Eq. 5.1 shows an equation similar to Eq. 2.7 depicting the first step in HSRL optical property processing for the retrieval of the two-way particulate transmission. However, here the ARB (ω) in the numerator has been replaced by a formula for the difference in the standard backscatter method retrieved ATB (γ) and the HSRL retrieved APB (α). Ground testing of this technique proved unviable due to overlap and low level aerosols causing unreliable ATB calibration to the atmospheric Rayleigh profile. However, airborne operations with accurate etalon calibration have the potential to yield accurate ATB (γ) and APB (α) retrievals leading to HSRL derived optical properties. This technique would be analogous to the iodine filter HSRL method in that the molecular signal would be inferred from the total ATB signal rather than

$$T_P^2(r) = \left[\frac{\gamma(r,\pi) - \alpha\,(r,\pi)}{\beta_M(r,\pi)T_M^2(r)}\right] \qquad \text{Eq. 5.1}$$

directly retrieved. In the iodine filter method it is the particulate signal that is inferred from the difference in the total and Rayleigh signal.

The studies discussed in Chapters 3 and 4 illustrate the complexity of understanding cirrus radiative properties. In these studies I utilized large datasets of cirrus optical and physical properties along with atmospheric reanalysis MERRA-2 data to best represent the cirrus layers incorporated into the libRadtran model. Large uncertainties on the order of 100% were still calculated due to varying habit parameterization, which is arguably the most complex problem facing cirrus radiative studies. Mean estimates of radiative forcing from both the CATS and CPL studies were on the order of -5 to +5 Wm^{-2} in the daytime when weighted by cirrus spatial and temporal frequencies. While the largest single source of uncertainty is likely habit parameterization, there is still no comprehensive understanding on the multivariate dependence of cirrus radiative effects due to cloud/environment interactions. Studies often individualize the effects of a single variable on the forcing holding other components constant simplifying the problem to $y = f(x)$. In reality the radiative forcing problem looks more like the function depicted in Eq. 5.2. Here forcing is shown as dependent on all variables disucussed prior, several of which are also dependent on altitude (h). Additionally, habit is a function of altitude and not constant through a cirrus layer, however this is a limitation of current RTMs until parameterizations are developed to account for vertical inhomogeneity. M represents all potential explainatory variables not explicitely shown. Future studies of cirrus clouds should

$$f\left(\sigma_P(h), IWC(h), d_{eff}(h), SZA, T(h), T_{sfc}, habit(h),\ Albedo_{sfc}\ , M\right) \quad \text{Eq. 5.2}$$

focus on multivariate statistics to better understand the change in radiative properties given varying conditions. One way to approach this would be through multiple linear regression (MLR) analysis. This type of analysis treats CRF as a response variable to the independent explanatory variables in Eq. 5.2. The result of MLR analysis are coefficients used to create a polynomial model reconstruction of the original CRF data of the form in Eq. 5.3.

$$CRF_{Model} = Const + coeff_{\sigma} * \ \sigma_P + coeff_{IWC} * IWC + coeff_{d_{eff}} * d_{eff} + \ldots \quad \text{Eq. 5.3}$$

Figure 5.1 shows a test case where I performed a multple linear regression analysis on the DJF and JJA afternoon radiative forcing shown in Fig. 3.12 A2 & C2, respectively. In this regression model I used only variablies that consist of a single value for each grid cell, rather than performing it across all range bins. The explanatory variables used were the COD, IWP, surface temperature, cloud top temperature, SZA, surface albedo, and mean particle effective diameter. To a first order comparing the images in Fig. 5.1 to those ins Fig. 3.12 this regression model performed well at qualitatvely capturing the global CRF distraibution. It is clear that the latitudinal components such as the SZA and surface temperature are well captured indicated by the agreement between the sign change in the mid-latitudes. However, the effects of optical depth are not as well captured with the negative forcing values in the Eastern Indian / Western Pacific regions caused by large optical depths are absent in Fig. 5.1. This would be an excellent area for further study. It is possible that the latitudinal effects had a greater correlation than COD resulting in a lower weight placed on optical depth in the MLR data reconstruction. Note that MLR analysis is limited to the habit parameterization used to model CRF, which is the MLR dependent variable.

Conducting the MLR analysis again with the same explainatory variables trained with the multi-habit CRF dataset would yield different results. However, MLR is still an excelent tool for better understand how all environmental and cloud parameters play an important roll determining CRF.

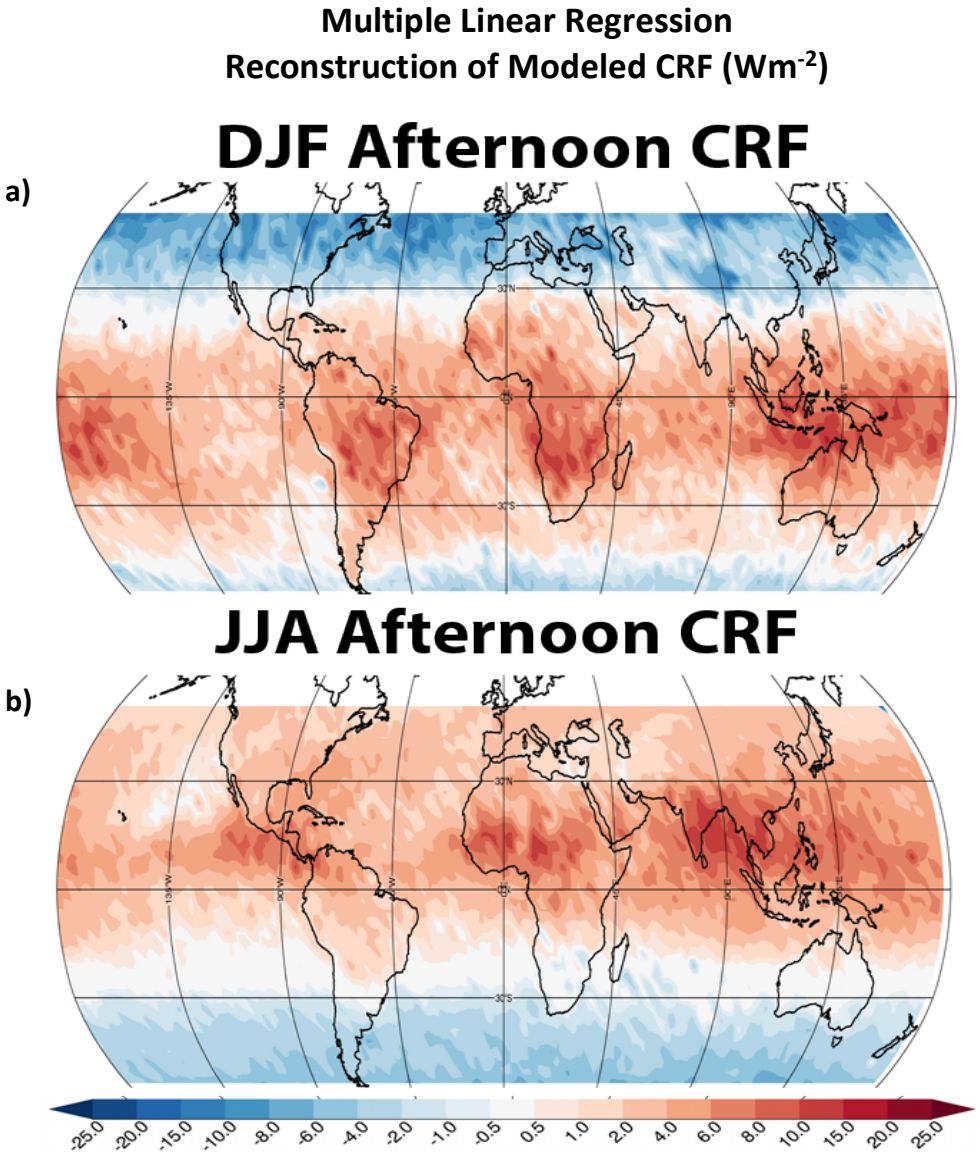

Figure 5.1. Multiple linear regression model used to reconstruct original cloud radiative forcing values calculated in libRadtran discussed in Chapter 3. **(a)** Depicts regression for DJF afternoon originally shown in Fig. 3.12 A2. **(b)** Regression for JJA afternoon originally shown in Fig 3.11 C2.

The DJF regression analysis had a 85.8% correlation with the original radiaitve forcing estimates, and the JJA regresion had a correlation of 79.5%. These high correlation coefficients show that this simple MLR model was fairly accurate is recreating and estimating the global cirrus radiative forcing. MLR analysis is a powerful tool that allows for valuable insite into how all variables simoutaneously effect cirrus radiative forcing. Further study and understanding of these principles could allow for first order approximations of modeled CRF without the use of a compiled RT model. Running RT simulations in the absence of supercomputing facilities is still time intensive, and work intensive to configure data properly for input. Each image in Fig. 3.12 and 3.14 took on the order of 10 hours to complete, however, the regression model in Fig. 5.1 took only seconds.

The primary topic of this study focused on cirrus radiative forcing at the top of the atmosphere. This important quantity is an excellent indicator of the impact on the climate used by the IPCC. However, another important radiative quantity listed in Fig. 1.1, but not disuccesed in these studies is the heating rate. To study cirrus heating rates, measured in units of Kelvin per day [K day^{-1}], the whole profile must be analyzed rather than just at the surface or TOA as often in the case of radiative forcing. Cirrus clouds induce variations in the atmospheric heating profile often causing cooling effects above the cloud and warming effects below the cloud (Liou 1986; Hong *et al.* 2015). Local heating rates around cirrus effect their internal structure as well as affecting surrounding conditions leading to the maintanence of current cirrus or future production. Future work should involve analyzing mean profiles of cirrus in the latitude-height plane for specific regions. Utilizing the CATS dataset regional spatial

resolutions could be modified to analyze diurnal heating rates at greater temporal resolution analyzed in Chapter 3. Figure 5.2 displays an example of this work, and the variability in the structure of atmospheric heaing rates between seasons. Fig. 5.2 shows afternoon heating rates over the Saharan and European region from 5° – 52° North using mean profiles averaged between 15° West and 40° degrees East. The ITCZ can be seen over 10° N in JJA (a), but is absent in DJF (b). The stronger sinking region in the Hadley cell caused by the presence of the ITCZ is observed over the Meditteranean

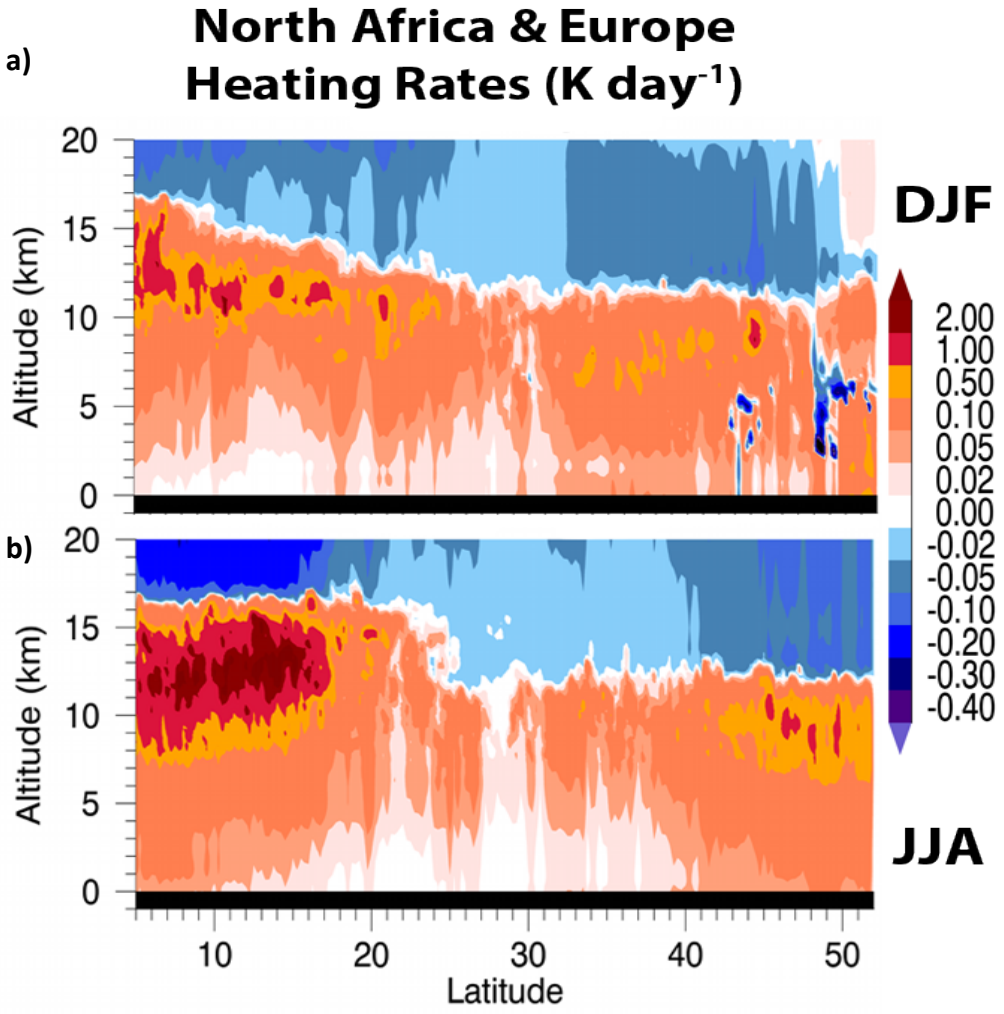

Figure 5.2. Latitude-height curtain image of afternoon heating rates over the Sahara and Europe with top image **(a)** representing DJF and the bottom **(b)** JJA.

around 28° N in JJA, and causes a reduction in cirrus frequency leading to low heating rates.

Lastly, this study illustrated the advantage to which CATS data is able to investigate diurnal variations in global phenomena. While I analyzed the diurnal signal of cirrus using two day and nighttime observations, future work could advance this approach by utilizing running averages or different spatial scales to achieve greater temporal resolution. CATS observations occur at all times of day, and taking advantage of this two and a half year dataset radiative forcing observations could be retrieved at hourly resolutions further constraining their climatic impact.

Chapter 6: Summary and Conclusions

In this dissertation I explored cirrus clouds utilizing lidar data from three instruments all operating from different platforms; each providing a different insight into cirrus cloud science. These included the ground-based zenith pointing ACATS lidar from a lab at NASA GSFC, the space-borne CATS lidar aboard the ISS, and the airborne CPL that operates from the high-altitude NASA ER-2.

In Chapter 2 I discussed a new method for etalon calibration for the ACATS lidar. ACATS utilizes the multi-channel technique, which employs a Fabry-Perot Interferometer (etalon) to spectrally resolve the backscattered signal across an array of detectors. This system architecture inherently allows ACATS to retrieve both HSRL optical properties and line-of-site Doppler wind velocities. Accurate characterization of etalon defect values are a crucial component required to retrieve ACATS HSRL and wind products. However, in previous airborne science operations etalon calibration was inconsistently reliable due to the weak Rayleigh signal at the operational altitude of 20 km. To resolve this issue a configuration consisting of a Delrin scattering medium and additional filters was integrated into the ACATS telescope housing. This proved to provide consistent etalon calibration from zenith pointing ground tests.

Initial testing of consecutive etalon scans showed this new method reduced the defect uncertainty by more than 50%, and reduced the standard deviation of defects by an order of magnitude compared to previous airborne retrievals. Additionally, the retrieved etalon defect values yielded consistent and reliable separation of the Rayleigh and particulate signals within observed cirrus layers. Though this was qualitatively

promising, the retrieved ARB profiles contained a low SNR with observed cirrus layers. This often resulted in low lidar ratios within cirrus layers, and anomalously high lidar ratios in cloud boundaries. This is primarily believed to be due to the 10 cm gap of the ACATS etalon filtering out a large percentage of the incoming Rayleigh signal. A reduced etalon gap would result in a greater transmission of the Rayleigh signal.

The 10 cm etalon is optimized for high resolution sampling of the Doppler shifted signal within particulate lasers. The new etalon calibration configuration additionally allows for retrievals of the laser reference spectrum required to calculate wind velocity. HSRL testing focus was shifted to the retrieval of vertical wind velocities within cirrus layers. Though the ACATS control software kept the laser and etalon well aligned during operations, it was shown laser stability was not of that required for science level wind data. Wind retrievals were improved by sampling the outgoing laser spectrum at higher temporal resolution, however this still exhibited a large standard deviation from the expected zero wind velocity.

The new etalon calibration method provided consistent defect values, though system limitations inhibited the retrieval of science quality HSRL and wind products from the ground-based zenith pointing platform. ACATS has yet to undergo operational testing from the ER-2 airborne platform where it was designed to operate. Future cirrus retrievals from the ER-2 will have the benefit of reduced range to target, and retrieval of the ARB from combing the standard backscatter and HSRL techniques.

In Chapter 3 and 4 I analyzed the radiative forcing that cirrus clouds exert at the top of the atmosphere using the libRadtran RT model. Chapter 3 I utilized the full 31 month CATS dataset consisting of thousands of orbits on the ISS where it observed

cirrus at all times of day. This data was used to develop gridded statistics of cirrus cloud properties between 51° North and South latitude for all seasons, which comprises approximately 78% of the global surface. Additionally, diurnal variations were analyzed across morning, afternoon, evening, and night affectively doubly the diurnal signal detected by the sun-synchronous CALIPSO lidar. Global cirrus frequencies remained approximately 40% across all seasons, though the spatial extent of frequencies shifted with the ITCZ in addition to strong diurnal variations. Layer integrated depolarization ratio and derived 180° phase function showed the varying scattering properties cirrus exhibit across different seasons and regions. In all seasons the mid-latitudes observed an increase in depolarization ratio during the daytime to around 0.35, decreasing in the nighttime hours to a range of 0.25 – 0.30. This trend corresponded to the diurnal trend observed in mean cloud top temperatures, and the inverse relationship of top temperature with depolarization ratio. The tropics had greater depolarization ratios around 0.40 due to colder cloud top temperatures, however, observed less diurnal variability. In addition to CATS layer statistics, mean profiles of cirrus ice water content and particle effective diameter were incorporated into the libRadtran model. RT simulations were ran twice for each grid point. First assuming a single global crystal habit, and then using a custom configuration of habits based on cirrus properties and previous in-situ studies. Single habit model runs estimated a mean global annual cirrus radiative forcing of 8.11 Wm^{-2} composed of 15.22 Wm^{-2} at nighttime and 1.00 Wm^{-2} during the day. The custom habit configuration estimate a global annual mean forcing of 5.78 Wm^{-2} with a net cooling during the daytime of -3.73 Wm^{-2}, and 15.29 Wm^{-2} at night.

In Chapter 4 I analyzed a large dataset of over 20,000 constrained CPL cirrus observations. These consisted of six flight campaigns that took place across all seasons, and ranged from 20° – 45° N latitude. The WAVE, PODEX, CCAVE, and ACEPOL campaigns consisted of synoptically developed cirrus while SEAC4RS and GOESR consisted of convectively developed cirrus. Modeled synoptic cirrus were parameterized using a bullet rosette habit, and convective cirrus with a column aggregate habit. Due to the greater scattering effects of aggregate crystals, convective cirrus were estimate to have a mean cooling effect, compared to the synoptic which primarily warmed. This resulted in the critical OD where the albedo effect becomes greater than greenhouse effect to be 0.34 COD in convective cirrus, and considerably higher in synoptic cirrus at 1.18 COD. With synoptic observations occurring primarily during colder seasons this contrasted the NH daytime forcing estimates discussed in Chapter 3. Additionally, synoptic cirrus were shown to have a direct correlation with the retrieved lidar ratio, where convective cirrus exhibited a weak indirect correlation. I have drawn several important conclusions regarding cirrus radiative impact on the climate from this work:

1) This dissertation places strong emphasis on the significance of cirrus in Earth's radiative budget, and the importance of accurate crystal habit representation when modeling their radiative effects. Changes in crystal habit scattering parametrization not only effects the magnitude of CRF, but also has the potential to change the sign. Additionally, this effect was shown to be more prevalent in the tropical regions, where cirrus are primarily associated with convective development. When averaging over all regions, seasons, and times of day the differences in crystal habit

lead to an improvement of the modeled annual mean CRF by 3 – 4 Wm^{-2}. The paradigm that cirrus have a TOA daytime warming effect is much more complex when further scrutinizing based on season, region, and subtype. The cirrus mean annual global radiative forcing is an important measure in GCMs, and was shown to be positive. However, this value is strongly regulated by cirrus conditions which favor negative CRF. Solar zenith angles greater than 65° used to represent morning and afternoon CATS observations in DJF yielded negative CRF in the mid-latitudes. While more frequent lower mid-day SZAs used to model CPL cirrus observations returned mean positive CRF. The diurnal CRF was presented in this study using a sin function, however it is likely that taking into account mid-day solar maximum would yield more positive daytime forcing estimates. This would result in a four or five degree polynomial function to best represent diurnal forcing, rather than a simple sinusoidal wave. This confirmed my hypothesis that to better constrain our understanding of cirrus RF it is beneficial to statistically analyze the effects for individual layers rather than use mean profiles. Additionally, it was shown that the mean warming effect of cirrus clouds can largely be attributed to nighttime observations in the absence of the solar albedo effect. Recent global efforts to combat climate change have suggested the geoengineering cirrus to increase the global albedo. While this is possible depending on the conditions under which ice nucleation would occur, cirrus would have to dissipated before SZAs surpass approximately 80° or they would contribute to global warming.

2) In the recent IPCC AR 4 and AR5 reports the emphasis on cirrus clouds is decidedly absent with focus placed on anthropogenic contrail cirrus. Though important, this

likely has a lesser impact due to relatively low global frequencies (Forster *et al.* 2007; Boucher *et al.* 2013). In contrast to the cirrus discussion, the IPCC aerosol discussion involves a comprehensive analysis of the radiative effects for individual aerosol types, which all have an estimated <1.0 Wm^{-2} forcing magnitude. I estimated the mean annual global cirrus CRF to contribute between 16.5 – 23.4% of the total cloud radiative effect, in close agreement with multiple GCM studies. This is significant as cirrus are poorly represented in GCMs, and have a radiative forcing similar in magnitude to CO_2 (Etminan *et al* 2016), if not potentially greater. It is has been shown that it is crucial to represent cirrus in GCMs with the same scrutiny to which aerosols are modeled by more realistically parameterizing and studying cirrus by their unique habit structures and subtypes.

3) Cirrus radiative effects are determined through non-linear interactions with optical properties, microphysical properties, and environmental conditions. While many studies place emphasis on the interactions with cloud properties such as COD and IWP, it was shown here that environmental conditions including SZA and temperature variables are also significant in addition to habit. In order to better elucidate cirrus forcing estimates it is pivotal for future studies to approach cirrus with multivariate analysis techniques. With Current GCMs altering cirrus frequency at all latitudes, this is essential to better constrain feedback mechanisms which have a high degree of uncertainty.

The importance of understanding cirrus clouds on Earth's radiation budget is undeniably a crucial area of research with still much to be understood. Advances in computing power, and open source community 1-D radiative transfer models have been

essential to recent cirrus studies. Ice crystal geometric scattering parameterizations built from supercomputer models are at the forefront of these efforts. However, cirrus radiation studies are still inhibited by the observational limitations and parameterization assumptions inherent to the model. I have only scratched the surface on understanding the importance of environmental conditions, temporal resolution, and accurate habit parameterizations when studying cirrus. Decreasing the assumptions made in modeling cirrus is crucial to improving our understanding of cirrus feedback mechanisms and their effect on our climate.

Appendices

APPENDIX A: Local Hour Angle Calculation

The local hour and zenith angle was calculated from code written for IDL by Yaswant Pradhan of the UK Met Office adopted from code by Wiel Wauben of the Royal Netherlands Meteorological Institute (KNMI), and is readily available on GitHub at https://github.com/bcdev/globcolour/blob/master/globcolour-matchup-tool/src/prototype/idl/GlobColour_MatchUp_IDLtool_UoP_v2-07-1/lib/SOLAR.pro Inputs required by the user to run the code include latitude, longitude, and UTC time which are all provided in standard CPL and CATS data products.

First, the Earth-Sun distance is calculated based on the Julian day.

$$\eta = \frac{2\pi(Day_{Julian})}{365}$$

$$X = 1.00011 + 3.4221E^{-2}\cos(\eta) + 7.19E^{-4}\cos(2\eta)$$

$$+1.28E^{-3}\sin(\eta) + 7.7E^{-5}\sin(\eta)$$

$$D_{sun} = \frac{1.0}{\sqrt{X}}$$

The solar declination is then calculated from the Julian day.

$$\delta_{\odot} = [6.198E^{-3} - 0.399912\cos(\eta) - 6.758E^{-3}\cos(2\eta) - 2.697E^{-3}\cos(3\eta)$$

$$+7.0257E^{-2}\sin(\eta) + 9.07E^{-4}\sin(2\eta) + 1.48E^{-3}\sin(3\eta)]$$

The equation of time was then calculated in units of hours, which accounts for variation in day length caused by Earth's axial tilt and orbit ellipticity.

$$\xi_{Time} = [7.2E^{-3}\cos(\eta) - 5.28E^{-2}\cos 2(\eta) - 1.2E^{-3}\cos(3\eta)$$

$$-0.1229\sin(\eta) - 0.1565\sin(2\eta) - 4.1E^{-3}\sin(3\eta)]$$

Using these values along with the user inputs the local hour time and SZA could then be retrieved.

$$T = 24 * (UTC + 1 - Day_{Julian})$$

$$Hour_{angle} = \left(\frac{360}{24}\right)\frac{T + longitude}{15 + \xi_{Time} - 12}$$

$$Altitude_{angle} = [\sin(\delta_{\odot}) * \sin(\text{latitude}) + \cos(\delta_{\odot}) + \cos(\text{latitude})$$

$$+ \cos(Hour_{angle})]$$

$$Solar_{Elevation} = \text{arcsine}(Altitude_{angle})$$

$$SZA = 2\pi - Solar_{Elevation}$$

$$Local_{Hour} = 12 + Hour_{Angle}\frac{180}{\pi}\left(\frac{24}{360}\right)$$

Bibliography

Abreu, V. J., Barnes, J. E., and Hays, P. B. (1992). Observations of winds with an incoherent lidar detector, Appl. Opt., 31, 4509–4514, https://doi.org/10.1364/AO.31.004509

Adam, O., Bischoff, T., Schneider, T. (2016) Seasonal and Interannual Variations of the Energy Flux Equator and ITCZ. Part II: Zonally Varying Shifts of the ITCZ. J. Climate, 29, 7281–7293, https://doi.org/10.1175/JCLI-D-15-0710.1

Bailey, M.P. and Hallett, J. (2009) A Comprehensive Habit Diagram for Atmospheric Ice Crystals: Confirmation from the Laboratory, AIRS II, and Other Field Studies. *J. Atmos. Sci.,* **66**, 2888–2899, https://doi.org/10.1175/2009JAS2883.1

Baker, B. A., and Lawson, R. P. (2006). In Situ Observations of the Microphysical Properties of Wave, Cirrus, and Anvil Clouds. Part I: Wave Clouds. Journal of the Atmospheric Sciences, 63(12), 3160–3185. https://doi.org/10.1175/jas3802.1

Baran, A. J., Francis, P. N., Havemann, S., and Yang, P. (2001). A study of the absorption and extinction properties of hexagonal ice columns and plates in random and preferred orientation, using exact T-matrix theory and aircraft observations of cirrus, J. Quant. Spectrosc. Ra., 70, 505–518, https://doi.org/10.1016/S0022-4073(01)00025-5

Baran, A. J. and Francis, P. N. (2004), On the radiative properties of cirrus cloud at solar and thermal wavelengths: A test of model consistency using high-resolution airborne radiance measurements. Q.J.R. Meteorol. Soc., 130: 763-778. doi:10.1256/qj.03.151

Baum, B., Yang, P., Heymsfield, A., Platnick, S., King, M., Hu, Y.-X., and Bedka, S. (2005). Bulk scattering models for the remote sensing of ice clouds. Part 2: Narrowband models, J. of Applied Meteorology, 44, 1896–1911, https://doi.org/10.1175/JAM2309.1

Baum, B., Yang, P., Hu., Y. X., and Feng. Q. (2010). The impact of ice particle roughness on the scattering phase matrix. Journal of Quantitative Spectroscopy and Radiave Transfer, 111(17-18), 2534-2549. https://doi.org/10.1016/j.jqsrt.2010.07.008

Benedetti-Michelangeli, G., Congeduti, F., and Fiocco, G. (1972). Measurement of aerosol motion and wind velocity in the lower troposphere by Doppler optical lidar, J. Atmos. Sci., 29, 906–910, https://doi.org/10.1175/1520-0469(1972)029<0906:MOAMAW>2.0.CO;2

Berry, E., and Mace, G. G. (2014). Cloud properties and radiative effects of the Asian summer monsoon derived from A-Train data. Journal of Geophysical Research, 119(15), 9492–9508. https://doi.org/10.1002/2014JD021458.

Blasing, T. J. (2016). Recent Greenhouse Gas Concentrations. United States. https://doi.org/10.3334/CDIAC/atg.032.

Boucher, O., Randall, D., Artaxo, P., Bretherton, C., Feingold, G., Forster, P., *et al*. (2013). Clouds and Aerosols. In: Climate Change 2013: The Physical Science Basis. Contribution of Working Group I to the Fifth Assessment Report of the Intergovernmental Panel on Climate Change. Retrieved from https://www.ipcc.ch/site/assets/uploads/2018/02/WG1AR5_Chapter07_FINAL-1.pdf

Bucholtz, A., Hlavka D. L., McGill, M., Schmidt, K. S., Pilewskie, P., Davis, S. M., Reid, E. A., and Walker, A. L. (2010) Directly measured heating rates of a tropical subvisible cirrus cloud, *J. Geophys. Res*., 115, D00J09, doi:10.1029/2009JD013128.

Buras, R., Dowling, T., and Emde, C. (2011). New secondary-scattering correction in DISORT with increased efficiency for forward scattering, J. Quant. Spectrosc. Radiat. Transfer, 112, 2028–2034, https://doi.org/10.1016/j.jqsrt.2011.03.019.

Campbell, J., S. Lolli, J. Lewis, Y. Gu, and E. Welton, (2016). Daytime Cirrus Cloud Top-of-the-Atmosphere Radiative Forcing Properties at a Midlatitude Site and Their Global Consequences. *J. Appl. Meteor. Climatol.,* 55, 1667–1679, doi:10.1175/JAMC-D-15-0217.1.

Chen, T., Rossow W. B., and Zhang, Y. (2000). Radiative Effects of Cloud-Type Variations. *J. Climate,* **13**, 264–286, https://doi.org/10.1175/1520-0442(2000)013<0264:REOCTV>2.0.CO;2

Choi, Y. S., Ho, C. H., and Sui, C. H. (2005). Different optical properties of high cloud in GMS and MODIS observations. Geophysical Research Letters, 32(23), 1–4. https://doi.org/10.1029/2005GL024616.

Choi, Y. S., and Ho, C. I. (2006). Radiative effect of cirrus with different optical properties over the tropics in MODIS and CERES observations. Geophysical Research Letters, 33(21). https://doi.org/10.1029/2006GL027403.

Chou, C., and Neelin, J. D., (2004). Mechanisms of global warming impacts on regional tropical precipitation. J. Clim., 17, 2688–2701.

Comstock, J. M., Ackerman, T. P., and Mace G. G. (2002). Groundbased lidar and radar remote sensing of tropical cirrus clouds at Nauru Island: Cloud statistic and radiative impacts. *J. Geophys. Res*., 107, 4714,

doi:10.1029/2002JD002203.

Cordero, R. R., Seckmeyer, G., Pissulla, D., Dasilva, L., and Labbe, F. (2007). Uncertainty evaluation of the spectral UV irradiance evaluated by using the UVSPEC radiative transfer model. Optics Communications, 276(1), 44–53. https://doi.org/10.1016/j.optcom.2007.04.008.

Das, S. S., Jain, A. R., Kumar, K. K., and Narayana Rao, D. (2008), Diurnal variability of the tropical tropopause: Significance of VHF radar measurements, *Radio Sci.*, 43, RS6003, doi:10.1029/2008RS003824.

Del Genio, A. D. (2002). GCM simulations of cirrus for climate studies. In *Cirrus*, D. K. Lynch *et al*., Eds., Oxford University Press, 310–326.

Eliasson, S., Buehler, S. A., Milz, M., Eriksson, P., and John, V. O. (2011). Assessing observed and modelled spatial distributions of ice water path using satellite data, Atmos. Chem. Phys., 11, 375-391, https://doi.org/10.5194/acp-11-375-2011.

Endemann, M., 2006: ADM-Aeolus: The first spaceborne wind lidar. *Proc. SPIE*, 6409, 64090G, https://doi.org/10.1117/12.697081.

Esselborn, M., Wirth, M., Fix, A., Tesche, M., and Ehret, G. (2008). Airborne high spectral resolution lidar for measuring aerosol extinction and backscatter coefficients. *Appl. Opt*, 47, 346– 358, https://doi.org/10.1364/AO.47.000346

Etminan, M., Myhre, G., Highwood, E. J., and Shine, K. P. (2016). Radiative forcing of carbon dioxide, methane, and nitrous oxide: A significant revision of the methane radiative forcing. Geophysical Research Letters, 43(24), 12,614-12,623. https://doi.org/10.1002/2016GL071930.

Fernald, F. G., Herman, B. M., and Reagan, J. A. (1972). Determination of Aerosol Height Distributions by Lidar. *J. Appl. Meteor.,* 11, 482–489, https://doi.org/10.1175/1520-0450(1972)011<0482:DOAHDB>2.0.CO;2.

Forster, P., Ramaswamy, V. Artaxo, P., Berntsen, T., Betts, R., Fahey, D. W., Haywood, J., Lean, J., Lowe, D. C., Myhre, G., Nganga, J., Prinn, R., Raga, G., Schulz M., and Van Dorland, R. (2007). Changes in Atmospheric Constituents and in Radiative Forcing. In: Climate Change 2007: The Physical Science Basis. Contribution of Working Group I to the Fourth Assessment Report of the Intergovernmental Panel on Climate Change [Solomon, S., D. Qin, M. Manning, Z. Chen, M. Marquis, K.B. Averyt, M.Tignor and H.L. Miller (eds.)]. Cambridge University Press, Cambridge, United Kingdom and New York, NY, USA.

Fu, Q. and Liou K. N., (1992). On the Correlated k-Distribution Method for Radiative Transfer in Nonhomogeneous Atmospheres. *J. Atmos. Sci.,* 49, 2139–2156, https://doi.org/10.1175/1520-0469(1992)049<2139:OTCDMF>2.0.CO;2 .

Gelaro, R., McCarty, W., Suárez, M. J., Todling, R., Molod, A., Takacs, L., Randles, C.A., Darmenov, A., Bosilovich, M.G., Reichle, R., Wargan, K., Coy, L., Cullather, R., Draper, C., Akella, S., Buchard, V., Conaty, A., da Silva, A. M., Gu, W., Kim, G.-K., Koster, R., Lucchesi, R., Merkova, D., Nielsen, J. E., Partyka, G., Pawson, S., Putman, W., Rienecker, M., Schubert, S.D., Sienkiewicz, M., and Zhao, B. (2017). The modern-era retrospective analysis for research and applications, version 2 (MERRA-2). Journal of Climate, 30(14), 5419–5454, https://doi.org/10.1175/JCLI-D-16-0758.1.

Guignard, A., Stubenrauch, C. J., Baran, A. J., and Armante, R. (2012). Bulk microphysical properties of semi-transparent cirrus from AIRS: a six year global climatology and statistical analysis in synergy with geometrical profiling data from CloudSat-CALIPSO, Atmos. Chem. Phys., 12, 503-525, https://doi.org/10.5194/acp-12-503-2012.

Gultepe, I., Heymsfield, A. J., and Lenschow, D. H. (1990). A Comparison of Vertical Velocity in Cirrus Obtained from Aircraft and Lidar Divergence Measurements during FIRE.*J. Atmos. Oceanic Technol.,* **7**, 58–67, https://doi.org/10.1175/1520-0426(1990)007<0058:ACOVVI>2.0.CO;2 .

Hair, J. W., Hostetler, C. A., Cook, A. L., Harper, D. B., Ferrare, R. A., Mack, T. L, Welch, W., Izquierdo, L. R., and Hovis, F. E. (2008). Airborne High Spectral Resolution Lidar for profiling aerosol optical properties," Appl. Opt. 47, 6734-6752, https://doi.org/10.1364/AO.47.006734.

Haladay, T., and Stephens, G. (2009), Characteristics of tropical thin cirrus clouds deduced from joint CloudSat and CALIPSO observations, *J. Geophys. Res.*, 114, D00A25, doi:10.1029/2008JD010675.

Held, I. M., and Soden, B. J., (2006). Robust responses of the hydrological cycle to global warming. J. Clim., 19, 5686–5699.

Heymsfield, A., Winker, D., Avery, M., Vaughan, M., Diskin, G., Deng, M., Mitev, V., and Matthey, R. (2014). Relationships between Ice Water Content and Volume Extinction Coefficient from In Situ Observations for Temperatures from 0° to −86°C: Implications for Spaceborne Lidar Retrievals. *J. Appl. Meteor. Climatol.,* **53**, 479–505, https://doi.org/10.1175/JAMC-D-13-087.1

Hong, Y., and Liu, G. (2015). The Characteristics of Ice Cloud Properties Derived from CloudSat and CALIPSO Measurements. *J.Climate,* 28, 3880-3901, https://doi.org/10.1175/JCLI-D-14-00666.1

Hong, Y., Liu, G. and Li, J.-L. F. (2016). Assessing the radiative effects of global ice clouds based on CloudSat and CALIPSO measurements. J. Climate, 29, 7651–7674, doi:10.1175/ JCLI-D-15-0799.1.

Jensen, E. J., Kinne, S., and Toon, O. B. (1994). Tropical cirrus cloud radiative forcing: Sensitivity studies. Geophysical Research Letters, 21(18), 2023–2026. https://doi.org/10.1029/94GL01358.

Kato, S., *et al*. (2011), Improvements of top-of-atmosphere and surface irradiance computations with CALIPSO-, CloudSat-, and MODIS-derived cloud and aerosol properties, *J. Geophys. Res.*, 116, D19209, doi:10.1029/2011JD016050.

Key, J. R., Yang, P., Baum, B. A., and Nasiri, S. L. (2002). Parameterization of shortwave ice cloud optical properties for various particle habits, J. Geophys. Res., 107, doi:10.1029/2001JD000 742.

Klett, J. D., (1981). Stable analytical inversion solution for processing lidar returns. *Appl. Opt*, 20, 211–220, https://doi.org/10.1364/AO.20.000211

Klett, J. D., (1985). Lidar inversion with variable backscatter/extinction ratios. *Appl. Opt*, 24, 1638–1643, https://doi.org/10.1364/AO.24.001638

Koch, W. (1996). Solar radiative transport in Arctic cirrus clouds; Solarer Strahlungstransport in arktischem Cirrus (Doctor Dissertation)

Korty, R. L., and Schneider, T. (2008). Extent of Hadley circulations in dry atmospheres. Geophysical Research Letters, 35(23). https://doi.org/10.1029/2008GL035847

Lawson, R. P., Baker, B. A., Schmitt, C. G., and Jensen, T. L. (2001). An overview of microphysical properties of Arctic clouds observed in May and July 1998 during FIRE ACE, J. Geophys. Res., 106, 14,989–15,014, doi:10.1029/2000JD900789.

Lawson, R. P., Baker, B. A., Pilson, B., and Mo, Q. (2006). In Situ observations of the microphysical properties of wave, cirrus and anvil clouds. Part II: Cirrus clouds, J. Atmos. Sci., 63, 3186–3203, doi:10.1175/JAS3803.1.

Lawson, R. P., Jensen, E., Mitchell, D. L., Baker, B., Mo, Q., and Pilson, B. (2010). Microphysical and radiative properties of tropical clouds investigated in TC4 and NAMMA, J. Geophys. Res., 115, D00J08, doi:10.1029/2009JD013017.

Lee, J., Yang, P., Dessler, A. E., Gao, B. C., and Platnick, S. (2009). Distribution and radiative forcing of tropical thin cirrus clouds. J. Atmos. Sci., 66, 3721–3731, doi:10.1175/2009JAS3183.1.

Liou, K. (1986). Influence of Cirrus Clouds on Weather and Climate Processes: A Global Perspective. *Mon. Wea. Rev.,* **114**, 1167–1199, https://doi.org/10.1175/1520-0493(1986)114<1167:IOCCOW>2.0.CO;2

Liou, K., Ou, S. C., Takano, Y., Valero, F. P. J., and Ackerman, T. P. (1990). Remote sounding of the tropical cirrus cloud temperature and optical depth using 6.5 and 10.5 pim radiometers during STEP, J. Appl. Meteorol. 29, 716-726, https://doi.org/10.1175/1520-0450(1990)029<0716:RSOTTC>2.0.CO;2

Liu, Z., McGill, M., Hu, Y., Hostetler, C. A., Vaughan, M., and Winker, D. (2004). Validating lidar depolarization calibration using solar radiation scattered by ice clouds. Geoscience Remote Sensing Letters, 1, doi: 10.1109/LGRS.2004.829613.

Lohmann, U., Spichtinger, P., Jess, S., Peter, T., and Smit, H. (2008). Cirrus cloud formation and ice supersaturated regions in global climate model. *Environ. Res. Lett.* 3(4), 5022-5033, http://dx.doi.org/10.1088/1748-9326/3/4/045022

Lolli, S., Campbell, J. R., Lewis, J. R., Gu, Y., Marquis, J. W., Chew, B. N., Liew, S., Salinas, S.V., and Welton, E. J. (2017). Daytime top-of-the-atmosphere cirrus cloud radiative forcing properties at Singapore. Journal of Applied Meteorology and Climatology, 56(5), 1249–1257. https://doi.org/10.1175/JAMC-D-16-0262.1

Loveland, T.R., and Belward, A.S. (1997). The IGBP-DIS global 1km land cover data set, DISCover: First results, International Journal of Remote Sensing, 18:15, 3289-3295, https://doi.org/10.1080/014311697217099

Luo, Z., and Rossow, W.B. (2004). Characterizing Tropical Cirrus Life Cycle, Evolution, and Interaction with Upper-Tropospheric Water Vapor Using Lagrangian Trajectory Analysis of Satellite Observations. *J. Climate,* **17**, 4541–4563, https://doi.org/10.1175/3222.1

Mace, G. G., Zhang, Q., Vaughan, M., Marchand, R., Stephens, G., Trepte, C., and Winker, D. (2009). A description of hydrometeor layer occurrence statistics derived from the first year of merged Cloudsat and CALIPSO data. Journal of Geophysical Research Atmospheres, 114(8). https://doi.org/10.1029/2007JD009755

Martins, E., Noel, V., and Chepfer, H. (2011). Properties of cirrus and subvisible cirrus from nighttime Cloud-Aerosol Lidar with Orthogonal Polarization (CALIOP), related to atmospheric dynamics and water vapor. Journal of Geophysical Research Atmospheres, 116(2). https://doi.org/10.1029/2010JD014519

Mayer, B., and Kylling, A. (2005). Technical note: The libRadtran software package for radiative transfer calculations – description and examples of use. Atmospheric Chemistry and Physics Discussions, 5(2), 1319–1381. https://doi.org/10.5194/acpd-5-1319-2005

McGill, M. J. (1996). Recovery and Validation of Wind and Aerosol Profiles from Incoherent Doppler Lidar Measurements (Doctoral Dissertation), University of Michigan (Ann Arbor, MI).

McGill, M. J., Skinner, W. R., and Irgang, T. D. (1997a). Analysis techniques for the recovery of winds and aerosol backscatter coefficients from a multiple channel incoherent Doppler lidar, *Applied Optics*, 36(6), 1253-1268, https://doi.org/10.1364/AO.36.001253

McGill, M. J., Marzouk, M., Scott, V. S., and Spinhirne, J. D. (1997b). Holographic circle-to-point converter with particular applications for lidar work, *Optical Engineering*, 36(8), 2171-2175, https://doi.org/10.1117/1.601437

McGill, M. J., and Spinhirne, J. D. (1998). A comparison of two direct-detection Doppler lidar techniques, *Optical Engineering*, 37(10), 2675-2686, https://doi.org/10.1117/1.601804

McGill, M., Hlavka, D., Hart, W., Scott, V. S., Spinhirne, J., and Schmid, B. (2002). Cloud Physics Lidar: instrument description and initial measurement results. Applied Optics, 41(18), 3725. https://doi.org/10.1364/ao.41.003725

McGill, M. J., Hlavka, D. L., Hart, W. D., Welton, E. J., and Campbell, J. R. (2003). Airborne lidar measurements of aerosol optical properties during SAFARI-2000. Journal of Geophysical Research: Atmospheres, 108, 8493, https://doi.org/10.1029/2002jd002370

McGill M. J., Yorks, J. E., Scott, V. S. Kupchock, A. W., and Selmer, A. P. (2015). The Cloud-Aerosol Transport System (CATS): a technology demonstration on the International Space Station. Lidar Remote Sensing for Environmental Monitoring XV, 96120A, https://doi.org/10.1117/12.2190841

McFarquhar, G. M., Heymsfield, A. J., Spinhirne. J., and Hart, B. (2000). Thin and subvisual tropopause tropical cirrus: Observations and radiative impacts, *J. Atmos. Sci*., **57(12)**, 1841– 1853, doi:10.1175/1520-0469(2000)057<1841:TASTTC>2.0.CO;2.

Meyer, K. G., and Platnick, S. (2010). Utilizing the MODIS 1.38 μm channel for cirrus cloud optical thickness retrievals: Algorithm and retrieval uncertainties, *J. Geophys. Res.*, **115**, D24209, doi:10.1029/2010JD014872.

Min, M., Wang, P., Campbell, J. R., Zong, X., and Li, Y. (2010). Midlatitude cirrus cloud radiative forcing over China. J. Geophys. Res., 115, D20210, doi:10.1029/2010JD014161.

Mitchell, D. L., Chai, S. K., Liu, Y., Heymsfield, A. J., Dong, Y. (1996). Modeling cirrus clouds. Part I: Treatment of bimodal size spectra and case study analysis. J. Atmos. Sci., 53 (1996), pp. 2952–2966, https://doi.org/10.1175/1520-0469(1996)053<2952:MCCPIT>2.0.CO;2

Morrison, H. and Grabowski, W. W., 2011: Cloud-system resolving model simulations of aerosol indirect effects on tropical deep convection and its thermodynamic environment, Atmos. Chem. Phys., 11, 10503-10523, doi:10.5194/acp-11-10503-2011

Murphy, D. M., Kelly, K. K., Tuck, A. F., Proffitt, M. H., and Kinne, S. (1990). Ice saturation at the tropopause observed from the ER-2 aircraft, Geophys. Res. Lett., 17, 353–356, https://doi.org/10.1029/GL017i004p00353

Myhre, G., D. Shindell, F.-M. Bréon, W. Collins, J. Fuglestvedt, J. Huang, *et al*. (2013). Anthropogenic and Natural Radiative Forcing. In: Climate Change 2013: The Physical Science Basis. Contribution of Working Group I to the Fifth Assessment Report of the Intergovernmental Panel on Climate Change Change. Retrieved from https://www.ipcc.ch/site/assets/uploads/2018/02/WG1AR5_Chapter08_FINAL.pdf

Nazaryan, H., McCormick, M. P., and Menzel, W. P. (2008). Global characterization of cirrus clouds using CALIPSO data, *J. Geophys. Res.*, 113, D16211, doi:10.1029/2007JD009481.

Noel, V., Winker, D. M., McGill, M., and Lawson, P. (2004). Classification of particle shapes from lidar depolarization ratio in convective ice clouds compared to in situ observations during CRYSTAL-FACE, J. Geophys. Res., 109, D24213, doi:10.1029/2004JD004883.

Noel, V., Chepfer, H., Chiriaco, M., and Yorks, J. (2018). The diurnal cycle of cloud profiles over land and ocean between 51° S and 51° N, seen by the CATS spaceborne lidar from the International Space Station, Atmos. Chem. Phys., 18, 9457–9473, https://doi.org/10.5194/acp-18-9457-2018

Ozog, S., Yorks, J., McGill, M., Nowottnick, E., Selmber, P., Dickerson, R. (2019). Mid-Latitude Cirrus Radiative Impacts and Sub-Type Variability Based on Constrained Airborne Lidar Observations. *Manuscript submitted for publication*

Pauly, R. M., Yorks, J. E., Hlavka, D. L., McGill, M. J., Amiridis, V., Palm, S. P.,

Rodier, S. D., Vaughan, M. A., Selmer, P. A., Kupchock, A. W., Baars, H., and Gialitaki, A. (2019). Cloud Aerosol Transport System (CATS) 1064 nm Calibration and Validation, Atmos. Meas. Tech. Discuss., https://doi.org/10.5194/amt-2019-172, *in review*

Platt, C. M. (1979). Remote Sounding of High Clouds: I. Calculation of Visible and Infrared Optical Properties from Lidar and Radiometer Measurements. *J. Appl. Meteor.,* **18**,1130–1143, https://doi.org/10.1175/1520-0450(1979)018<1130:RSOHCI>2.0.CO;2

Platt, C. M., and Dilley, A. C. (1981). Remote Sounding of High Clouds. IV: Observed Temperature Variations in Cirrus Optical Properties. *J. Atmos. Sci.,* **38**, 1069–1082,https://doi.org/10.1175/1520-0469(1981)038<1069:RSOHCI>2.0.CO;2

Platt, C. M. R., Austin, R. T., Young, S. A., and Heymsfield, A. J. (2002). LIRAD Observations of Tropical Cirrus Clouds in MCTEX. Part II: Optical Properties and Base Cooling in Dissipating Storm Anvil Clouds*. Journal of the Atmospheric Sciences, 59(22), 3163–3177. https://doi.org/10.1175/1520-0469(2002)059<3163:lootcc>2.0.co;2

Pruppacher, H. R., and Klett, J. D. (1997). Microphysics of Clouds and Precipitation. Kluwer Academic, 954 pp.

Ramanathan V., Cess R. D., Harrison E. F., Minnis P., Barkstrom B. R., Ahmad E., & Hartmann. D. (1989). Cloud-radiative forcing and climate: Results from the Earth Radiation Budget Experiment. American Association for the Advancement of Science, 243(4887), 57–63. Retrieved from http://links.jstor.org/sici?sici=0036-8075%2819890106%293%3A243%3A4887%3C57%3ACFACRF%3E2.0.CO%3B2-V

Sassen, K. (1991a). Corona-producing cirrus cloud properties derived from polarization lidar and photographic analyses, Appl. Opt., 30, 3421–3552, https://doi.org/10.1364/AO.30.003421

Sassen, K. (1991b) The polarization lidar technique for cloud research: A review and current assessment. *Bull. Amer. Meteor. Soc*, **72,** 1848–1866, https://doi.org/10.1175/1520-0477(1991)072<1848:TPLTFC>2.0.CO;2

Sassen, K. and Cho, B.S. (1992). Subvisual-Thin Cirrus Lidar Dataset for Satellite Verification and Climatological Research. *J. Appl. Meteor.,* 31, 1275–1285, https://doi.org/10.1175/1520-0450(1992)031<1275:STCLDF>2.0.CO;2

Sassen, K., Benson, R. P., and Spinhirne, J. D. (2000). Tropical anvil cirrus cloud properties from TOGA/COARE airborne polarization lidar. *Geophys. Res. Lett*, **27,** 673–676, https://doi.org/10.1029/1999GL010946

Sassen, K. (2001). Cirrus: A Modern Perspective. Cirrus, D. Lynch *et al*., Eds., Oxford University Press, in press. 11 – 40

Sassen, K., and Benson, S. (2001). A midlatitude cirrus cloud climatology from the Facility or Atmospheric Remote Sensing. Part II: Microphysical properties derived from lidar depolarization. J. Atmos. Sci., 58, 2103– 2112, https://doi.org/10.1175/1520-0469(2001)058<2103:AMCCCF>2.0.CO;2

Sassen, K., and Comstock, J. M. (2001). A midlatitude cirrus cloud climatology from the Facility for Atmospheric Remote Sensing. Part III: Radiative properties. J. Atmos. Sci., 58, 2113–2127, https://doi.org/10.1175/1520-0469(2001)058<2113:AMCCCF>2.0.CO;2

Sassen, K., Liou, K.-N., Takano, Y., and Khvorostyanov, V. I. (2003). Diurnal effects in the composition of cirrus clouds, *Geophys. Res. Lett.*, 30, 1539, doi:10.1029/2003GL017034, 10.

Sassen, K., Wang, Z., and Liu, D. (2008). Global distribution of cirrus clouds from CloudSat/Cloud-Aerosol Lidar and Infrared Pathfinder Satellite Observations (CALIPSO) measurements, *J. Geophys. Res.*,113, D00A12, doi:10.1029/2008JD009972.

Sassen, K., Wang, Z., and Liu, D. (2009). Cirrus clouds and deep convection in the tropics: Insights from CALIPSO and CloudSat, *J. Geophys. Res.*, 114, D00H06, doi:10.1029/2009JD011916

Schaaf, C., and Wang, Z. (2015). *MCD43C3 MODIS/Terra+Aqua BRDF/Albedo Albedo Daily L3 Global 0.05Deg CMG V006* [Data set]. NASA EOSDIS Land Processes DAAC. doi: 10.5067/MODIS/MCD43C3.006

Shindell, D., and Faluvegi, G. (2009). Climate response to regional radiative forcing during the twentieth century. Nature Geosci., 2, 294–300, https://doi.org/10.1038/ngeo473

Soden, B. J. (2000). The diurnal cycle of convection, clouds, and water vapor in the tropical upper troposphere, Geophys. Res. Lett., 27, 2173–2176, https://doi.org/10.1029/2000GL011436

Spinhirne, J. D., Reagan, J. A., and Herman, B. M. (1980). Vertical Distribution of Aerosol Extinction Cross Section and Inference of Aerosol Imaginary Index in the Troposphere by Lidar Technique. *J. Appl. Meteor.,* 19, 426–438, https://doi.org/10.1175/1520-0450(1980)019<0426:VDOAEC>2.0.CO;2

Stamnes, K., Tsay, S.-C., Wiscombe, W., and Jayaweera, K. (1988). Numerically stable algorithm for discrete–ordinate–method radiative transfer in multiple scattering

and emitting layered media, Appl. Opt., 27, 2502–2509. https://doi.org/10.1364/AO.27.002502

Stamnes, K., Tsay, S.-C., Wiscombe, W., and Laszlo, I. (2000). DISORT, a General-Purpose Fortran Program for Discrete-Ordinate-Method Radiative Transfer in Scattering and Emitting Layered Media: Documentation of Methodology, Tech. rep., Dept. of Physics and Engineering Physics, Stevens Institute of Technology, Hoboken, NJ 07030

Stephens, G.L., Vane, D.G., Boain, R.J., Mace, G.G., Sassen, K., Wang, Z., Illingworth, A.J., O'connor, E.J., Rossow, W.B., Durden, S.L., Miller, S.D., Austin, R.T., Benedetti, A., Mitrescu, C., and, (2002). THE CLOUDSAT MISSION AND THE A-TRAIN. *Bull. Amer. Meteor. Soc.,* 83, 1771–1790, https://doi.org/10.1175/BAMS-83-12-1771

Stephens, G. L. (2005). Cloud Feedbacks in the Climate System: A Critical Review. *J. Climate,* **18**, 237–273, https://doi.org/10.1175/JCLI-3243.1

Stubenrauch, C.J., Rossow, W.B., Kinne, S., Ackerman, S., Cesana, G., Chepfer, H., Di Girolamo, L., Getzewich, B., Guignard, A., Heidinger, A., Maddux, B.C., Menzel, W.P., Minnis, P., Pearl, C., Platnick, S., Poulsen, C., Riedi, J., Sun-Mack, S., Walther, A., Winker, D., Zeng, S., & Zhao, G. (2013). Assessment of Global Cloud Datasets from Satellites: Project and Database Initiated by the GEWEX Radiation Panel. *Bull. Amer. Meteor. Soc.,* 94, 1031–1049, https://doi.org/10.1175/BAMS-D-12-00117.1

Sun, W., Videen, G., Kato, S., Lin, B., Lukashin, C., and Hu, Y. (2011), A study of subvisual clouds and their radiation effect with a synergy of CERES, MODIS, CALIPSO, and AIRS data, J. Geophys. Res., 116, D22207, doi:10.1029/2011JD016422.

Suneeth, K. V., Das, S. S. and Das, S. K. Clim Dyn (2017) 49: 3277. https://doi.org/10.1007/s00382-016-3512-x

Tian, B., Soden, B. J., and Wu, X. (2004). Diurnal cycle of convection, clouds, and water vapor in the tropical upper troposphere: Satellites versus a general circulation model, J. Geophys. Res., 109, D10101, https://doi.org/10.1029/2003JD004117

Twomey, S. (1977). The Influence of Pollution on the Shortwave Albedo of Clouds. *J. Atmos. Sci.,* 34, 1149–1152, https://doi.org/10.1175/1520-0469(1977)034<1149:TIOPOT>2.0.CO;2

Tucker, S.C., Weimer, C. S., Baidar, S., and Hardesty, R.M. (2018). The Optical Autocovariance Wind Lidar. Part I: OAWL Instrument Development and

Demonstration. *J. Atmos. Oceanic Technol.*, **35**, 2079–2097, https://doi.org/10.1175/JTECH-D-18-0024.1

Vaughan, J. M. (1989). The Fabry-Perot Interferometer, Adam Hilger, Philadelphia.

Wang, P. H., Minnis, P., McCormick, M. P., Kent, G. S., and Skeens, K. M. (1996). A 6 year climatology of cloud occurrence frequency from stratospheric aerosol and gas experiment II observations (1985–1990), J. Geophys. Res., 101(D23), 29407–29429, https://doi.org/10.1029/96JD01780

Wang, Z., and Sassen, K. (2002). Cirrus cloud microphysical property retrieval using lidar and radar measurements. Part I: Algorithm description and comparison with in situ data. J. Appl. Meteor., 41, 218–229, https://doi.org/10.1175/1520-0450(2002)041<0218:CCMPRU>2.0.CO;2

Welton, E. J., Campbell, J. R, Spinhirne, J. D., and Scott, V. S. (2001). Global monitoring of clouds and aerosols using a network of micro-pulse lidar systems, Proc. SPIE, 4153, 151-158, https://doi.org/10.1117/12.417040

Wendisch, M., Pilewskie, P., Pommier, J., Howard, S., Yang, P., Heymsfield, A. J., Schmitt C. J., Baumgardner D., and Mayer, B. (2005). Impact of cirrus crystal shape on solar spectral irradiance: A case study for subtropical cirrus. Journal of Geophysical Research: Atmospheres, 110(3), 1–17. https://doi.org/10.1029/2004JD005294

Winker, D. M., Vaughan, M. A., Omar, A. H., Hu, Y., Powell, K. A., Liu, Z., Hunt, W. H., and Young, S. A. (2009). Overview of the CALIPSO Mission and CALIOP Data Processing Algorithms. J. Atmos. Oceanic Technol., 26, 1105-1119, doi:10.1175/2009JTECHA1281.1.

Winker, D.M., Pelon, J., Coakley, J.A, Ackerman, S.A., Charlson, R.J., Colarco, P.R., Flamant, P., Fu, Q., Hoff, R.M., Kittaka, C., Kubar, T.L., Le Treut, H., McCormick, M.P., Mégie, G., Poole, L., Powell, K., Trepte, C., Vaughan, M.A., and Wielicki, B.A. (2010). The CALIPSO Mission. *Bull. Amer. Meteor. Soc.,* **91**, 1211–1230,https://doi.org/10.1175/2010BAMS3009.1

Woods, S., Lawson, R. P., Jensen, E., Bui, T. P., Thornberry, T., Rollins, A., *et al*. (2018). Microphysical properties of tropical tropopause layer cirrus. *Journal of Geophysical Research: Atmospheres*, 123, 6053– 6069. https://doi.org/10.1029/2017JD028068

Wylie, D. P., Menzel, W. P., Woolf, H. M., and Strabala, K. I. (1994). Four Years of Global Cirrus Cloud Statistics Using HIRS. *J. Climate,* **7**, 1972–1986,https://doi.org/10.1175/1520-0442(1994)007<1972:FYOGCC>2.0.CO;2

Wylie, D. P., and W. P. Menzel (1999), Eight years of high cloud statistics using HIRS, J. Clim., 12, 170–184, doi:10.1175/1520-0442-12.1.170.

Yang, P., Liou, K. N., Wyser, K., and Mitchell, D. (2000). Parameterization of the scattering and absorption properties of individual ice crystals. Journal of Geophysical Research Atmospheres, 105(D4), 4699–4718. https://doi.org/10.1029/1999JD900755

Yang, P., Wei, H., Huang, H.-L., Baum, B. A., Hu, Y. X., Kattawar, G. W., Mishchenko M., and Fu, Q. (2005). Scattering and absorption property database for nonspherical ice particles in the near- through far-infrared spectral region. Applied Optics, 44(26), 5512. https://doi.org/10.1364/ao.44.005512

Yang, P., Bi, L., Baum, B. A., Liou, K., Kattawar, G. W., Mishchenko, M. I., and Cole, B. (2013). Spectrally Consistent Scattering, Absorption, and Polarization Properties of Atmospheric Ice Crystals at Wavelengths from 0.2 to 100 μm. *J. Atmos. Sci.,* **70**, 330–347, https://doi.org/10.1175/JAS-D-12-039.1

Yi, B., Yang, P., Baum, B. A., L'Ecuyer, T., Oreopoulos, L., Mlawer, E. J., Heymsfield, A. J., and Liou, K. (2013). Influence of Ice Particle Surface Roughening on the Global Cloud Radiative Effect. *J. Atmos. Sci.,* **70**, 2794–2807, https://doi.org/10.1175/JAS-D-13-020.1

Yorks, J. E., Hlavka, D. L., Hart, W. D., and McGill, M. J. (2011). Statistics of Cloud Optical Properties from Airborne Lidar Measurements. J. Atmos. Oceanic Technol., 28, 869–883. doi: http://dx.doi.org/10.1175/2011JTECHA1507.1

Yorks, J. E., McGill, M. J., Scott, V. S., Wake, S. W., Kupchock, A., Hlavka, D. L., Hart, W. D., and Selmer, P. A. (2014). The Airborne Cloud–Aerosol Transport System: Overview and Description of the Instrument and Retrieval Algorithms. *J. Atmos. Oceanic Technol.,* **31**, 2482–2497, https://doi.org/10.1175/JTECH-D-14-00044.1

Yorks, J. E. (2014). An Investigation of Cirrus Cloud Properties Using Airborne Lidar (Doctoral Dissertation), University of Maryland (College Park, MD). Retrieved from https://drum.lib.umd.edu/handle/1903/15324

Yorks, J. E., Palm, S. P., McGill, M. J., Hlavka, D. L., Hart, W. D., Selmer, P. A., and Nowottnick E. (2015). The Cloud Aerosol Transport System (CATS) Algorithm Theoretical Basis Document release 1.2. Retrieved from https://cats.gsfc.nasa.gov/media/docs/CATS_Data_Products_Catalog.pdf

Yorks, J. E., Palm, S. P., McGill, M. J., Hlavka, D. L., Hart, W. D., Selmer, P. A., and Nowottnick E. (2018). Cloud Aerosol Transport System (CATS) Data Release

Notes version 3.0. Retrieved from https://cats.gsfc.nasa.gov/media/docs/CATS_Release_Notes7.pdf

Young, A.T. (1981). Rayleigh scattering. *Phys. Today*, **35**, 42–48.

Young, S. A., Vaughan, M. A., Kuehn, R. E., & Winker, D. M. (2013). The retrieval of profiles of particulate extinction from Cloud-Aerosol Lidar and Infrared Pathfinder Satellite Observations (CALIPSO) data: Uncertainty and error sensitivity analyses. Journal of Atmospheric and Oceanic Technology, 30(3), 395–428. https://doi.org/10.1175/JTECH-D-12-00046.1

Zhang, Y., Macke, A., and Albers, F. (1999). Effect of crystal size spectrum and crystal shape on stratiform cirrus radiative forcing, Atmos. Res. 52, 59-75, https://doi.org/10.1016/S0169-8095(99)00026-5

Zhao, Y., Mace, G. G., and Comstock, J. M. (2011). The occurrence of particle size distribution bimodality in midlatitude cirrus as inferred from ground-based remote sensing data, *J. Atmos. Sci.*, **68**, 1162–1177, doi:10.1175/2010JAS3354.1.